# On periodically driven quantum systems

Proefschrift

ter verkrijging van
de graad van Doctor aan de Universiteit Leiden,
op gezag van Rector Magnificus prof. mr. C.J.J.M. Stolker,
volgens besluit van het College voor Promoties
te verdedigen op dinsdag 20 september 2016
klokke 15.00 uur

door

Brian Michael Tarasinski

geboren te Berlijn (Duitsland) in 1988

| | |
|---|---|
| Promotor: | Prof. dr C. W. J. Beenakker |
| Co-promotor: | Dr J. K. Asbóth (Hungarian Academy of Sciences) |
| Promotiecomissie: | Prof. dr P. W. Brouwer (FU Berlin, Duitsland) |
| | Dr M. T. Wimmer (TU Delft) |
| | Prof. dr E. R. Eliel |
| | Prof. dr V. Vitelli |

Casimir PhD Series Delft-Leiden 2016-24
ISBN 978-90-8593-268-0
An electronic version of this thesis can be found
at https://openaccess.leidenuniv.nl

Dit werk maakt deel uit van het onderzoekprogramma van de Stichting voor Fundamenteel Onderzoek der Materie (FOM), die deel uit maakt van de Nederlandse Organisatie voor Wetenschappelijk Onderzoek (NWO).

This work is part of the research programme of the Foundation for Fundamental Research on Matter (FOM), which is part of the Netherlands Organisation for Scientific Research (NWO).

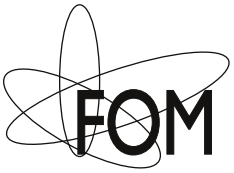



Cover: Geometric interpretation of the two winding numbers of a nontrivial time evolution operator of a driven Su-Schrieffer-Heeger model (cf. Chapter 3).

# Contents

# 1 Introduction

## 1.1 Preface

In the last few decades, a major part of the field of condensed matter physics is the exploration, classification, prediction and experimental realization of *topological insulators and superconductors* (which, perhaps counter-intuitively, can be treated very similarly; this is because superconductors are *thermal* insulators). Such materials are indistinguishable from "normal" (or *trivial*) insulators or superconductors in local bulk properties like density of states or electrical and thermal conductivity, but are still different from normal states in a manner that disallows a transition from topological to trivial without going through a *topological phase transition*, during which the material loses its insulating property.[75,143]

A principle called *bulk-boundary correspondence* implies that a boundary between two different topological phases hosts robust edge states, often with very peculiar properties, like absence of backscattering or dephasing, or non-Abelian exchange statistics. These properties have been recognized to have potential applications in quantum computing, both as memory and for the implementation of quantum gates.[131]

Since then, a lot of experimental effort was put in the realization and manipulation of materials with topological phases, but the materials shown to have such properties are rather sparse.

In search for new experimental handles to engineer the topological properties of a material, the possibility of periodic external driving was proposed,[116] which was shown to induce a topological band structure in an initially trivial semiconductor. When periodical driving is introduced to a quantum system, the so-called *Floquet theory* is usually employed, so that this new type of topological insulators are called *Floquet topological insulators*.

A model that captures the essential difference between insulators and Floquet insulators is the so-called *quantum walk*, a quantum-mechanical

analogue to the random walk. Just like the classical random walk, the quantum walk evolves in discrete time steps, so that the effect of the external driving is represented by the subsequent application of time-step evolution operators. It turns out that the family of quantum walks are rich enough to implement relatively simple models with non-trivial phase diagram for all different possible symmetry classes.[101] Quantum walks thus can serve as a platform to study the different topological phases of Floquet topological insulators.

Besides their topological properties, quantum walks have also gained a lot of popularity in the design of quantum algorithms.[91,175] As many classical algorithms can be understood as a (more or less) random walk on a decision graph, the "quantization" of that random walk may lead to a quantum algorithm for the same problem, often achieving close to optimal quantum speed-up.

In the next three chapters of this thesis, we study the properties of Floquet topological insulators by the help of quantum walks. In the chapter thereafter, we present a related but slightly different study: We consider the time-dependent transition of a (non-Floquet) topological Josephson junction and its relaxation to the new ground state. The final chapter is devoted to the experimental study of the spin-orbit interaction in nanowires of indium antimonide, which are the central building block in one of the most promising experimental approaches to manufacture a one-dimensional topological superconductor.[128]

In the rest of this introduction, we outline a few basic ideas that are used heavily in this thesis, especially the next three chapters, introducing most of the key concepts highlighted above, including the Floquet theory, basic properties of quantum walks, the idea of band topology and the resulting bulk-boundary correspondence, and a connection between a quantum walk-based algorithm and band topology. We conclude with a more detailed summary of the subsequent chapters of this thesis.

## 1.2 Floquet formalism

*Periodically driven systems* Most chapters in this thesis are concerned with non-interacting single quantum particles whose time evolution is governed by explicitly time-dependent Hamiltonians. Especially, we consider a time evolution where the system is subject to a *periodic driving*, so that the Hamiltonian is explicitly dependent on time and

obeys

$$H(t) = H(t+T) \tag{1.1}$$

for some fixed period $T$.

The energy of such systems is not conserved and it is not possible to reduce the Schrödinger equation to the stationary Schrödinger equation. However, the situation is essentially equivalent to the situation of a particle in a periodic potential, implying broken translational invariance in *space*, which can be tackled by the well-known Bloch theorem. Here, similar ideas can be applied, replacing space with *time*. The resulting theory is referred to as the *Floquet theory* of periodically driven systems.

*The Floquet operator* The basic element of Floquet theory is the unitary *Floquet operator* $F$, which is the time evolution operator of the system over one period. It can thus be found as the solution of the Schrödinger equation for the time-evolution operator

$$i\tfrac{d}{dt}U(t,t_0) = H(t)U(t,t_0), \tag{1.2}$$

$$U(t_0,t_0) = 1, \tag{1.3}$$

evaluated after one period:

$$F_{t_0} = U(t_0+T,t_0). \tag{1.4}$$

One can write the solution formally as

$$F_{t_0} = \mathbb{T}\exp\left(-i\int_{t_0}^{t_0+T} H(t)dt\right), \tag{1.5}$$

where $\mathbb{T}$ refers to time ordering.

It is important to note that the Floquet operator depends on the choice of $t_0$. However, different choices are related by a unitary transformation:

$$F_{t_1} = U(t_1,t_0)F_{t_0}U(t_0,t_1). \tag{1.6}$$

We will refer to the choice of $t_0$ as the choice of a *time frame* for the Floquet operator. It is analogous to the choice of a unit cell for a lattice in the Bloch theory.

*Quasienergy and effective Hamiltonian* In analogy with the Bloch theorem, it can then be shown that any solution of the time-dependent Schrödinger equation can be written as a superposition of solutions that are eigenfunctions of the Floquet operator. Such solutions can be written as

$$\psi_\varepsilon(t) = e^{-i\varepsilon t} u_\varepsilon(t), \tag{1.7}$$

where $e^{-i\varepsilon T}$ is an eigenvalue of $F$, and $u_\varepsilon(t)$ is a function with period $T$.

If one considers the function $\psi_\varepsilon(t)$ only at integer multiples of $T$, its time dependence resembles that of a wave function with energy $\varepsilon$. It is thus said to have *quasi-energy* $\varepsilon$. For time scales much larger than $T$, the evolution of a wave function is the same as that of a system governed by a stationary Schrödinger equation with the *effective Hamiltonian*

$$H_{\text{eff}} = \frac{i}{T} \log(F_{t_0}). \tag{1.8}$$

Because of the transformation Eq. (1.6), the spectrum of $H_{\text{eff}}$ does not depend on the choice of $t_0$, but the eigenfunctions $u_\varepsilon(t)$ do.

Finally, we note that all quasienergies $\varepsilon$ can be chosen to lie in the interval $\left[-\frac{\pi}{T}, \frac{\pi}{T}\right]$ (corresponding to the selection of the principle branch of the logarithm) and should be considered periodic on that interval. This is again in analogy with spatially periodic systems, and in fact this interval is sometimes referred to as the quasienergy Brillouin zone.

## 1.3 Random walks and quantum walks

*Random walks* A classical random walk is a random process of a walker on a one-dimensional lattice with lattice sites labeled by $x \in \mathbb{Z}$. The walk consists of an integer number of steps, during each of which the walker either walks to the right with probability $p$, or to the left with probability $1-p$. We refer to the position of the walker after $t$ steps as $X_t$.

For the probability distribution after $t$ steps, $\rho(x,t) = \Pr(X_t = x)$, one thus obtains the recursion relation

$$\rho(x,t+1) = p\,\rho(x-1,t) + (1-p)\rho(x+1,t). \tag{1.9}$$

For the walker starting at site $x = 0$, the solution is well-known to be the binomial distribution

$$\rho(x,t) = \begin{cases} \binom{t}{(x+t)/2} p^{(x+t)/2}(1-p)^{(x-t)/2} & \text{if } x+t \text{ even,} \\ 0 & \text{otherwise.} \end{cases} \tag{1.10}$$

*Quantum random walks* One of the basic assumptions of quantum theory is that the result of a measurement is a random process. We can thus implement a classical random walk by using quantum mechanics: We consider a quantum mechanical particle (the walker) on a one-dimensional lattice, whose state space is spanned by $\{|x\rangle, x \in \mathbb{Z}\}$, together with a coin, whose state space is spanned by the two states $\{|+\rangle, |-\rangle\}$ (corresponding to "heads" and "tails"). Any state of the total system is thus given by a two component wave function $\psi(x) = (u(x), v(x))$ by the expansion

$$|\psi\rangle = \sum_x u(x)|x\rangle|+\rangle + v(x)|x\rangle|-\rangle. \tag{1.11}$$

Instead of referring to the two systems as walker and coin, we appeal to a physicist's intuition by regarding $\psi$ as the wave function of a spin-1/2 particle on a lattice. Correspondingly, the two coin states will also often be referred to as "spin-up" and "spin-down" (instead of "heads" and "tails").

Assume now that the system starts out in the state $|\psi_0\rangle = |x = 0\rangle|+\rangle$. We then apply the following operations: We first "flip" the coin by applying a rotation of the spin:

$$R_\theta \begin{pmatrix} u(x) \\ v(x) \end{pmatrix} = \begin{pmatrix} \cos\theta & -\sin\theta \\ \sin\theta & \cos\theta \end{pmatrix} \begin{pmatrix} u(x) \\ v(x) \end{pmatrix} = e^{-i\theta\sigma_y} \begin{pmatrix} u(x) \\ v(x) \end{pmatrix}, \tag{1.12}$$

where here and in the rest of the introduction, we use $\vec{\sigma} = (\sigma_x, \sigma_y, \sigma_z)$ to denote the vector of Pauli matrices in the $\{|+\rangle, |-\rangle\}$ basis of the coin.

After the rotation, we apply a *spin-dependent translation operator* $S$, defined by:

$$S \begin{pmatrix} u(x) \\ v(x) \end{pmatrix} = \begin{pmatrix} u(x-1) \\ v(x+1) \end{pmatrix}, \tag{1.13}$$

which moves the spin-up component of the wave function to the right and the spin-down component to the left. If we now perform a measurement of the position of the walker, the walker will have performed a random walk step, having moved to the right with probability $p = \cos^2\theta$, and to the left with probability $1 - p = \sin^2\theta$. A balanced random walk is obtained when choosing $\theta = \pi/4$. In order to perform another step, the coin must be reinitialized to $|+\rangle$.

commuting operators $S = S_+S_-$, where each of the two only shifts one spin species while leaving the other in place, we can also choose $F_4 = S_+RS_-$. The two latter choices for $F$ are of special relevance as they imply additional symmetries on the eigenfunctions, which is play a role in Chapters 2, 3 and 4.

*The Galton board* There is an illustrative device to demonstrate the idea of a classical random walk, called the Galton board (also known as a quincunx, or bean machine), which consist of a board with interleaved rows of pins, arranged in a diagonal lattice (the term quincunx actually refers to the arrangement of five dots as on the five-side of a regular game die: ⚄, which is the arrangement repeated to form the lattice of pins on the Galton board, see Fig. 1.1). If a stream of irregular shaped objects (beans) is flowing through this arrangement, the objects will pass one pin of each row either on the left or the right, with a very high sensitivity to the precise conditions, so essentially with equal probability, $p = 1/2$. If the object are collected in bins after $t$ rows, one obtains a histogram of samples from the probability distribution $\rho(x,t)$. The vertical axis thus represents time in this experiment.

*The optical Galton board* An analogous implementation of the quantum walk is obtained by replacing the beans with a monochromatic beam of light, and the pins with semi-transparent mirrors, so-called beam splitters. The amplitudes of two incoming wave fronts $(u,v)$ at 45-degree angles from both sides is related to the outgoing wave fronts at 45-degree angles $(u',v')$ by the scattering matrix

$$\begin{pmatrix} u' \\ v' \end{pmatrix} = \begin{pmatrix} \cos\theta & -\sin\theta \\ \sin\theta & \cos\theta \end{pmatrix} \begin{pmatrix} u \\ v \end{pmatrix}, \tag{1.15}$$

where we took the liberty to define the phase of the incoming and outgoing modes so that this matrix is real. The angle $\theta$ is given by the reflectivity of the beam splitter. If we arrange an array of identical beam splitters in the same manner, an incident beam on one of the first rows in the array will propagate through the lattice, performing a simple quantum walk. The state of the coin is encoded in horizontal component of the wave vector. The beam splitters perform the action of the coin operator $R$, while the free propagation in the space between the beam splitters leads to the shift operator $S$. Detecting the intensity of

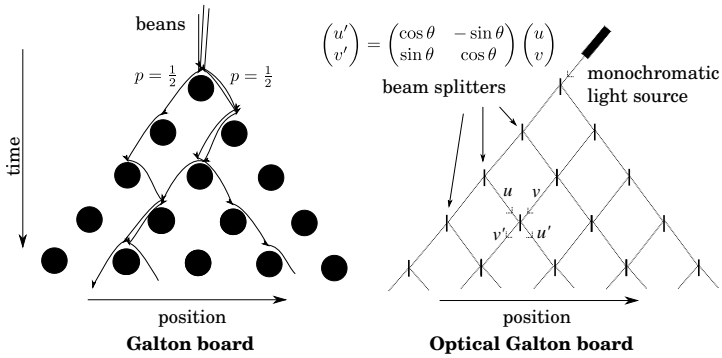


**Figure 1.1:** *Left:* The Galton board consists of pins through which beans are falling, performing a classical random walk. The number of rows of pins corresponds to the number of time steps taken in the walk. *Right:* In the optical Galton board, the beans are replaced by a monochromatic beam and the pins by beam splitters. Beams propagating to the right are considered spin-up and left-propagating beams spin-down. The mixing of the two species happens at the beam splitters, which corresponds to a rotation $R_\theta$, while diagonal propagation in the space between the beam splitters corresponds to a spin-dependent shift. In a "balanced" quantum walk with half-transparent mirrors, one has $\theta = \pm\pi/4$ or $\theta = \pm 3\pi/4$.

the partial beams after $n$ rows of beam splitters will thus result in the probability distributions $(|u(x)|^2, |v(x)|^2)$ of the corresponding quantum walk. By interference measurements, one could even recover the phases, and thus obtain the function $\psi(x,t)$.

One might argue that this construction shows that in fact the quantum walk does not even deserve the name "quantum", as it can be implemented using classical waves. However, it must be understood that both of the experiments presented here for the classical and quantum walk only serve as an illustration of the corresponding processes and are by no means an *efficient* implementation of either, given that the size of the physical system is proportional to the square of the number of steps. In contrast, an efficient simulation of the classical quantum walk, on a classical computer, say, only requires $\log_2(n)$ physical objects (bits) to hold the position of the walker, and similarly, an efficient implementation of the quantum walk only requires $\log_2(n)$ qubits.

*Differences between random walk and quantum walk* Even though the construction in the previous paragraphs suggests similarities between

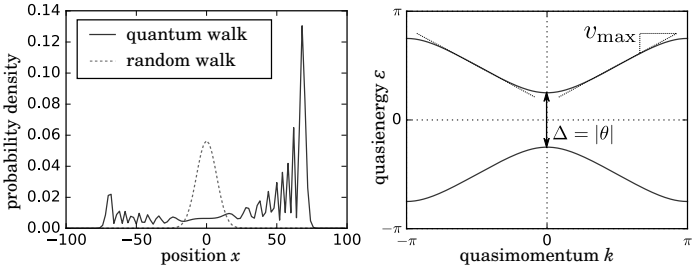


**Figure 1.2:** *Left:* Comparison of a classical random walker starting at the origin and a simple quantum walker with $\theta = \pi/4$ and initial state $|\psi_0\rangle = |x = 0\rangle\,|+\rangle$, after $t = 100$ steps. We show the probability density $\rho(x)$ for the classical walker, and the probability distribution for a position measurement $\rho(x) = |u(x)|^2 + |v(x)|^2$ for the quantum walk. For both walks, we only show the probability at even lattice sites, for odd lattice sites the probability is zero. *Right:* The quasienergy band structure of the same quantum walk. The maximum propagation speed is $v_{\max} = \pm\sqrt{2}$, and the gap in the spectrum is given by $\Delta = |\theta|$.

classical random walks and quantum walks, it turns out that the two behave quite differently. To illustrate the difference, we consider the spread of the probability amplitude of a particle that starts out on a single site with spin up, $|\psi_0\rangle = |x = 0\rangle\,|+\rangle$. We choose the rotation angle $\theta = \pi/4$. Fig. 1.2 shows the square of the probability amplitude after $n = 100$ steps, compared to the probability distribution of a classical random walker starting at $x = 0$, which is $\rho(x, t = 100)$.

While for the random walk we obtain the familiar bell-shaped distribution of width $\sqrt{t}$, the quantum walk results in a relatively flat distribution, featuring oscillations, and terminated by two peaks at around $\pm t/\sqrt{2}$.

The long time behavior of the quantum walk Eq. (1.14) can be understood by considering its Floquet operator and corresponding quasienergy spectrum. Because this system is translational invariant, we can perform a Fourier transformation in space:

$$\psi(x,t) = \int_0^{2\pi} \frac{dk}{2\pi} e^{ikx} \psi(k,t). \tag{1.16}$$

In this basis, the shift operator $S$ preserves $k$ and can be written as

$$S(k) = \exp(i\sigma_z k). \tag{1.17}$$

We thus can calculate and diagonalize the Floquet operator in spin

space.[101] The result can be expressed as

$$F(k) = SR_\theta = \exp(-i\varepsilon_k \hat{n}_k \cdot \vec{\sigma}), \tag{1.18}$$

and the corresponding effective Hamiltonian is thus given by

$$H_{\text{eff}} = \varepsilon_k \hat{n}_k \cdot \vec{\sigma}. \tag{1.19}$$

In this expression, the quasienergies $\varepsilon_k$ is given by (see Fig. 1.2)

$$\varepsilon_k = \pm \arccos(\cos k \cos\theta). \tag{1.20}$$

This spectrum can be used to discuss the long-time behavior of a wave packet[97]: A stationary-phase approximation of a wave function that contains contribution from all $k$ (as a very localized initial conditions does, by Heisenberg's uncertainty relation), will have most of its contribution at $\pm v_{\max}$, which for $\theta = \pi/4$ is given by $v_{\max} = \sqrt{2}/2$. Besides the ballistic spread, the other striking difference between the two distributions in Fig. 1.2 is the asymmetry of the quantum walk. It is a consequence of the asymmetry of the initial condition $|+\rangle$, together with the fact that the quantum walk is *not* "random", i.e. Markovian, and does retain information about its past indefinitely, due to its unitary evolution. The fact that the $|+\rangle$ state is asymmetric becomes clear in Fig. 1.1, where the initial spin is given by the direction of the initial beam.

## 1.4 Generalizations and related concepts

Above, we described the simplest version of the quantum walk, consisting of a shift and a rotation. Since, a plethora of generalizations have been considered.

A generalization in one dimension is to split the shift operator $S$ in two operators $S = S_+ S_-$ which only shift one spin component, leaving the other in place:

$$S_+ \begin{pmatrix} u(x) \\ v(x) \end{pmatrix} = \begin{pmatrix} u(x-1) \\ v(x) \end{pmatrix}, \quad S_- \begin{pmatrix} u(x) \\ v(x) \end{pmatrix} = \begin{pmatrix} u(x) \\ v(x+1) \end{pmatrix}. \tag{1.21}$$

Additionally, a longer sequence of different rotations can be applied. This leads to the family of *split-step quantum walks*[14,101] with Floquet operators given by

$$F = S_n R_{\theta_n} \cdots S_2 R_{\theta_2} S_1 R_{\theta_1}, \tag{1.22}$$

where $S_n \in \{S_+, S_-\}$ and each $\theta_n \in [0, 2\pi]$. These one-dimensional walks are the main subject of study in Chapters 2, and time-dependent Hamiltonians with similar properties are studied in Chapter 3.

Generalizations to higher dimensions have also been studied.[54,101] A common approach is to introduce shift operators that perform the spin-dependent shift along a selected axis and applies these alternatingly.

Another generalization (in one or more dimensions) is the introduction of a coin space of higher dimension. The shift operator then typically shifts two perpendicular subspace in opposite directions. This approach is used in Chapter 2 to obtain a quantum walk with additional symmetries.

In fact, there are generalizations of the idea of a quantum walk to arbitrary graphs.[60] A similar approach,[168] which is used in the design of quantum algorithms, establishes a one-to-one correspondence between random walks (Markov processes) on any graph and a "quantized" walk on the same graph. Unlike described here, this approach is based on reflections as the basic building block, not rotations. Still, under this paradigm, the random walk on a line and the simple quantum walk described above are indeed mapped to each other.*

Yet another modification of the quantum walk, which was considered especially in the context of the optical Galton board implementation, is the addition of non-linear operator to the time-evolution.[130] A modification of this nature is investigated in Chapter 4.

## 1.5 Band topology

In this thesis, we are mostly concerned with the topological properties of the band structure of quantum walks. Before we consider the peculiarities occurring in quantum walks and driven system, we quickly review the idea of topological band structures. We restrict our attention to non-interacting systems and focus mainly on one-dimensional systems.

The general idea is that a band is a periodic and continuous map from the toric Brillouin zone to the set of eigenfunctions (mathematically, elements of $\mathbb{C}P^n$).† For one-dimensional two-band models like the simple

*Because any rotation can be written as a product of two reflections, quantum walks with rotations and quantum walks with reflections are very similar in any case.

†This means that eigenfunctions are only defined up to a phase. This is important, because in general, one cannot make a continuous choice of phase for all $k$.

quantum walk, it is the map from the unit circle of quasimomenta to spinors, which can be imagined on the surface of the Bloch sphere. The spin structure of a band can thus be envisioned as a closed path on the surface of a sphere.

Under certain conditions, mappings can be different from each other topologically, meaning that it is impossible to continuously deform one mapping into the other. For closed curves on the Bloch sphere, however, no such distinction exists: All paths on the unit sphere can be smoothly deformed into a point, and thus also into each other.

*Winding of a chiral Hamiltonian* This situation can change, however, when additional constraints are present. For instance, consider a tight-binding Hamiltonian on a bipartite lattice with no on-site energies. This means that the lattice can be divided into two sublattices $A$ and $B$, and the Hamiltonian only has finite elements between the two. We can then write the Hamiltonian as

$$H = \begin{pmatrix} 0 & \tilde{H}^\dagger \\ \tilde{H} & 0 \end{pmatrix}, \tag{1.23}$$

where the subblocks of the Hamiltonian correspond to the $A$ and $B$ sublattice. The subblock $\tilde{H}$ still is a matrix in position basis (ignoring for now possible further sub-structure such as spin). The structure of this Hamiltonian can be described as

$$\sigma_z H \sigma_z = -H, \tag{1.24}$$

where $\sigma_z$ is acting on the $A/B$ blocks. A symmetry of this sort is referred to as *chiral* symmetry.*

We now consider the translationally invariant case, were bands can form. We write the same Hamiltonian in momentum basis:

$$H(k) = h_x(k)\sigma_x + h_y(k)\sigma_y = \begin{pmatrix} 0 & h^*(k) \\ h(k) & 0 \end{pmatrix}. \tag{1.25}$$

Then, the spinors are restricted to the equator on the Bloch sphere, as long as $h(k) \neq 0$. The path associated with each band will traverse this

*This term is borrowed from elementary particle physics, where its occurrence in a Hamiltonian actually is related to the *handedness* of the corresponding particles. Here, the term is used because of the similar mathematical structure. For an overview over the history of the different uses of this term, we refer to the introductory chapter of Ref. 49

circle an integer number of times, and no deformation subject to the chiral symmetry restriction can change this; furthermore there even is a sense of orientation to this winding. For the underlying Hamiltonian, its two bands will preserve this distinction as long as the bands are separate, i.e. the gap does not close, $h(k) \neq 0$.

To capture this idea in mathematical terms, note that an eigenvector $\xi_k = (u(k), v(k))$ of the Hamiltonian (1.25) will always satisfy $|v(k)/u(k)|^2 = 1$, (the stereographic projection of the equator of the Bloch sphere is the unit circle). Thus, we can write the integral

$$\nu = \int \frac{dk}{2\pi i} \partial_k \log(v(k)/u(k)), \tag{1.26}$$

which, according to the Cauchy integral theorem, will give the number of times $v/u$ winds around the origin, or equivalently (by stereographic projection), how often $\xi_k$ winds around the north-south axis of the Bloch sphere. In this two-band example, the other band is given by $\bar{\xi}_k = (u_k, -v_k)$, and has the same winding number. Because $v/u = h/|h|$, the winding can also be found directly from the Hamiltonian:

$$\nu = \frac{1}{2\pi i} \oint \frac{dh}{h} = \int \frac{dk}{2\pi i} \partial_k \log(h(k)), \tag{1.27}$$

*Symmetry classes* In one dimension, topological distinction of bands can thus only occur under the assumption of symmetries. These symmetries are assumed to act locally: We require that they only act on the spin subspace.* Usual unitary symmetries which commute with the Hamiltonian are generally not of interest, they only lead to decoupled blocks of the Hamiltonian which can be considered individually. But there are other symmetries, which anticommute with the Hamiltonian, or are antiunitary. That leaves three possibilities: *Time-reversal symmetry* $T$ (antiunitary, anticommuting), *particle-hole symmetry* $P$ (antiunitary, commuting), and *chiral symmetry* $\Gamma$ (unitary, anticommuting).[9,150] The antiunitary symmetries can either square to 1 or $-1$, and the presence of two of such symmetries dictates the presence of the third;† this results

*In some systems, like graphene, a chiral symmetry emerges due to a sublattice symmetry. Then, the chiral symmetry operator involves two neighboring sublattice sites, and thus is only "almost" local.

†Also, not more than one of each of the symmetries can be present. E.g. if there are two time-reversal symmetries $T_1$ and $T_2$, then $T_1 T_2$ is a unitary symmetry of the Hamiltonian, which we excluded.

in the existence of ten different symmetry classes, of which five turn out to allow topological distinctions in one dimension. Chapter 2 considers all of these, while in the rest of the introduction, we only consider classes AIII and BDI (see below) as examples.

Finally, we remark that the names of the symmetry operators hint to certain physical mechanism that ensure them. However, in this thesis, most models are rather artificial, so that the names of the symmetries should be considered historical, and their mathematical properties should be taken as their definition independent of their origin.

Consider the Hamiltonian Eq. (1.25). It can have all three symmetries: It will always have a chiral symmetry represented by the operator $\Gamma = \sigma_z$:

$$\sigma_z H(k) = -H(k)\sigma_z. \tag{1.28}$$

If this is the only present symmetry, the Hamiltonian is said to belong to symmetry class AIII. If furthermore, $h(k) = h^*(-k)$, the system also has a particle-hole symmetry $P = K$, which is complex conjugation in position basis:

$$H^*(-k) = H(k). \tag{1.29}$$

Note that complex conjugation in position basis involves $k \to -k$ in momentum basis. This particle-hole symmetry operator $P$ is of the kind $P^2 = 1$. Furthermore, because $\Gamma$ and $P$ are present, then also $T = \Gamma P = \sigma_z K$ is a time-reversal symmetry of the system, and in this case is of type $T^2 = 1$. This class is referred to as BDI and as we will see shortly, the simple quantum walk belongs to this class.

However, so far, we have discussed the symmetries and band topology of time-independent Hamiltonians. The same classification can be applied to the quasienergy bands of a Floquet system, but the role of the symmetries has to be carefully re-evaluated: Firstly, it is not immediately clear how the presence of a discrete symmetry in the effective Hamiltonian is caused by certain symmetries in the underlying time-dependent Hamiltonian. Secondly, even if such a symmetry exists, because the eigenfunctions depend on the choice of the time frame, the symmetries and corresponding topological numbers may also depend on the time frame. This allows for a somewhat richer classification scheme of the topology of driven systems and is the main subject of investigation in Chapters 2 and 3.

*Symmetry and topology of the simple quantum walk* To illustrate these points, we discuss the topological properties of the simple quantum walk. The Floquet operator is given by

$$F = Se^{-i\theta\sigma_y} \tag{1.30}$$

As we can check immediately, the effective Hamiltonian has a particle-hole symmetry $P = K$, as can be seen from

$$F^* = F, \tag{1.31}$$

because $S$ is real in position basis (it only has matrix elements 0 and 1). It follows that

$$H_{\text{eff}}^* = -H_{\text{eff}}. \tag{1.32}$$

It turns out that the same system also has a chiral symmetry.[14,14,101] However, in the effective Hamiltonian presented above, it is "hidden". Namely, when changing the time frame to

$$F = R_{\theta/2} S R_{\theta/2}, \tag{1.33}$$

we can see by a quick calculation that

$$\sigma_x F \sigma_x = F^{-1} \quad \Rightarrow \quad \sigma_x H_{\text{eff}} \sigma_x = -H_{\text{eff}}, \tag{1.34}$$

so that chiral symmetry is given by $\Gamma = \sigma_x$. Particle-hole symmetry is still given by $K$; consequently, a time-reversal symmetry is also present. The symmetry class this effective Hamiltonian thus is BDI, and by a simple change of basis, we could write it in the form of Eq. (1.25).

The winding number of this effective Hamiltonian can be found by direct calculation, and turns out to be $\nu = \text{sgn}\theta$.*

If we try to find the "hidden symmetry" in the original time frame, we can use the fact that time frames are connected by unitary transformations. We can reconstruct the action of $\Gamma = \sigma_x$ and find the "chiral symmetry operator" in the original basis: $\Gamma = R_{-\theta/2}\sigma_x R_{\theta/2}$. This operator is not a useful symmetry operator: It explicitly contains the parameter $\theta$, and thus it is not sensible to compare the winding numbers of

*The sign is actually not well-defined, as it depends on the basis transformation used to bring $H_{\text{eff}}$ to a standard form. For discussion of this matter we refer to the appendix of Chapter 2.

Hamiltonians with different values of $\theta$, furthermore, adding any inhomogeneities or disorder to $\theta$ seems to break it. In the symmetrized time frame Eq.(1.33), however, these problems to not apply. We thus say that the simple quantum walk belongs to symmetry class BDI because *there exists one time frame* in which the effective Hamiltonian has the required symmetries.

Finally, we note that in the second symmetrized time frame mentioned above, namely $F = S_+ R S_-$, the same chiral symmetry $\Gamma = \sigma_x$ holds; the winding number in this time frame however is always $\nu = 0$, independent of $\theta$. We thus see that the choice of time frame is relevant.

## 1.6 Bulk-boundary correspondence

The most interesting consequence of band topology occurs when two large (so that bands can form) systems are interfaced at a common boundary. The general principle of the *bulk-boundary correspondence* predicts that at such an interface, bound states of a certain type must always exists even when both systems have no extended states at that energy and the topological number is different for both systems.

In general, the features of such bound states depend on the dimensionality of the problem and on the symmetries involved. In one dimension, such bound states are located precisely at zero energy (which is a special energy, because it is singled out by chiral or particle-hole symmetry). These states, often called *Majorana zero modes*, have been the subject to much interest recently for their robustness: not only is their presence guaranteed independent of the details of the boundary, and also not destroyed by the presence of disorder, but additionally their energy is pinned to a fixed value. This *topological protection* makes these states interesting for use as storage of quantum information (qubits).

*The bulk-boundary correspondence in one-dimensional chiral systems*
Because the later chapters make much use of the bulk boundary correspondence, we shall sketch here, as an example, how the bulk-boundary correspondence emerges for two-band Hamiltonians with chiral symmetry. We consider a setup where the lattice is divided into two *bulk domains* $A$ and $B$, in which the Hamiltonian is constant in space, with different parameters, so that it can be described by two translationally invariant Hamiltonians $H_{A,B}(k)$. In between, in the *boundary region*,

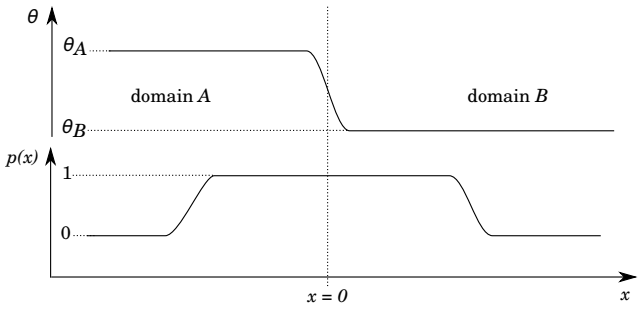


**Figure 1.3:** At a domain boundary, the Hamiltonian, parametrized by the parameter $\theta$, varies between two different values $\theta_A$ and $\theta_B$, and is translationally invariant in the two bulk domains. If the two Hamiltonians are topologically different, protected zero modes are expected in the region where the function $p(x)$ is finite, which is the essence of the bulk-boundary correspondence.

the Hamiltonian interpolates between the two domains in an arbitrary way (see Fig. 1.3), with the restriction, however, that the Hamiltonian of the total system still obeys the chiral symmetry, so that we can write it as:

$$H = \begin{pmatrix} 0 & h^\dagger \\ h & 0 \end{pmatrix}, \tag{1.35}$$

where $h$ is a matrix acting on position space only, and its matrix elements $h_{xx'}$ are local: We require that $h_{xx'}$ decays exponentially as $|x - x'| \to \infty$, and that $h$ is approaches translational invariance deep in the domains.

*The flat-band Hamiltonian* The object of consideration now is a deformed version of $H$, the *flat-band Hamiltonian* $Q$, given by

$$Q = \operatorname{sign} H, \tag{1.36}$$

which is obtained by deforming all positive eigenvalues of $H$ to $+1$ and all negative eigenvectors to $-1$, and leaving zero eigenvalues at zero. For the bulk Hamiltonians, this corresponds to rectifying the loop $h(k)$ to lie on the unit circle, $h(k) \to q(k) = h(k)/|h(k)|$, which does not change its winding number. We thus can write the operator for the setup including the boundary as

$$Q = \begin{pmatrix} 0 & q^\dagger \\ q & 0 \end{pmatrix}, \tag{1.37}$$

where the operator $q$ acts on space only. A crucial important property of $Q$, which we shall not prove here, is that, like $H$, its matrix elements decay in real space exponentially, i.e. $q_{xx'} = O(e^{-\xi|x-x'|})$ as $|x-x'| \to \infty$ for some decay length $\xi$.*

Consider now an eigenfunction $\psi = (u, v)$ of $Q$ with eigenvalue $\pm 1$:

$$qu = \pm v, \quad q^\dagger v = \pm u. \tag{1.38}$$

Then,

$$q^\dagger q u = u, \quad q q^\dagger v = v \tag{1.39}$$

And thus, $u$ is an eigenvector of $q^\dagger q$ while $v$ is an eigenvector of $qq^\dagger$, both with eigenvalue 1.

Eigenfunctions of $Q$ with eigenvalue 0, on the other hand, can be chosen to have either $v = 0$ or $u = 0$, and thus are eigenfunctions of the chiral operator $\sigma_z$ at the same time. We thus distinguish zero modes by their *chirality* $n$, $\sigma_z \psi = n\psi$, where $n = \pm 1$.

*Counting the zero modes* We can thus write down the *total chirality*, i.e. the sum of the chiralities of all the zero modes of $Q$, as

$$n = \dim\ker q^\dagger q - \dim\ker qq^\dagger \tag{1.40}$$

(dim ker denotes the dimension of the kernel, in other words, the number of linearly independent zero eigenfunctions) and because we just saw that the eigenvalues of $qq^\dagger$ and $q^\dagger q$ only take values $0, 1$, this can be expressed as traces:

$$n = \mathrm{tr}(1 - q^\dagger q) - \mathrm{tr}(1 - qq^\dagger) = \mathrm{tr}(qq^\dagger - q^\dagger q). \tag{1.41}$$

Only zero modes of $Q$ contribute to exactly one of the two traces, depending on the chirality. We immediately see that in any finite system (i.e. with periodic boundary conditions), the total chirality $n = 0$, by cyclic invariance of the trace. For the infinite line, the mathematical situation is more complicated and the result can be finite. [142]

*In fact, an algebraic decay $|x-x'|^\alpha$ with $\alpha < -1$ is sufficient [95]; but fast decay often holds and makes for somewhat easier intuition of the proof.

*Zero modes in a region* We can modify the formula to count only those zero modes that have support in the boundary region. For that, we introduce the operator

$$P = \sum_x p_x \, |x\rangle \langle x| \,, \tag{1.42}$$

where (see Fig. 1.3)

$$p_x = \begin{cases} 1 & \text{close the boundary region} \\ \to 0 & \text{as } |x| \gg \xi, \text{ far in the domains.} \end{cases} \tag{1.43}$$

This allows us to define the chirality of that region as

$$n = \mathrm{tr}(qq^\dagger - q^\dagger q)P. \tag{1.44}$$

The effect of the operator $P$ is that eigenfunctions of $Q$ only contribute according to their weight in the region where $p_x$ is finite, so that zero modes in the region where $p_x = 0$ are not counted.

In position space we can then write

$$n = \sum_{xx'} \left( q^*_{x'x} q_{x'x} - q^*_{xx'} q_{xx'} \right) p_{x'} = \sum_{xy} q^*_{x+y,x} q_{x+y,x} \left( p_{x+y} - p_x \right), \tag{1.45}$$

and because $q_{x+y,x}$ decays, there is no contribution for large $y$. This means that there is no contribution for $x$ close to the boundary, because $p_x - p_{x+y} = 1 - 1 = 0$ for small $y$, We only get contributions where $p$ varies, which is in the bulk. This allows us to obtain an expression which only involves the bulk Hamiltonians and is independent of the exact properties of the boundary.

In the bulks, $q$ is translationally invariant, and we can write $q_{xx'} = q_{A,x-x'}$ where $p$ varies from zero to one, and $q_{xx'} = q_{B,x-x'}$ where $p$ varies back to zero. Then we can write*

$$n = \sum_{xy} q^*_{x+y,x} q_{x+y,x} \left( p_{x+y} - p_x \right) = \sum_y y q^*_{A,y} q_{A,y} - \sum_y y q^*_{B,y} q_{B,y}. \tag{1.46}$$

*We used the following telescoping formulas:

$$\sum_{x \ll 0} p_x - p_{x+1} = p_{-\infty} - p_0 = -1, \quad \text{thus} \quad \sum_{x \ll 0} p_x - p_{x+y} = -y.$$

for all not too large $y$; and a similar expression for $x > 0$. The fact that we then can also extend the sum over $y$ to infinity requires the decay of $q$.

Using the Fourier transform $q_{A/B,y} = \int q_{A/B,k} e^{iky} (dk/2\pi)$, we can finally write this as $n = \nu_B - \nu_A$, where

$$\nu_{A/B} = -\sum_y y q_{A/B,y} q^*_{A/B,y} = -i \int \frac{dk}{2\pi} q^*_{A/B,k} \partial_k q_{A/B,k}, \tag{1.47}$$

which is the winding number of $q(k)$, and thus $h(k)$ defined in Eq. (1.27) Thus we conclude that if the winding number of $q(k)$, and thus of $h(k)$, changes by $\delta\nu$ across a domain boundary, the total chirality of the states in the boundary is indeed given by $\delta\nu$, and especially, the number of zero modes in the boundary is at least $|\delta\nu|$.

*Bulk-boundary correspondence in Floquet systems* The bulk-boundary correspondence also applies to effective Hamiltonians, but is not sufficient. The crucial difference is the definition of $Q$: While for stationary Hamiltonians, the sign function is defined unambiguously, effective Hamiltonians are defined only up to multiples of $2\pi$, which makes the distinction arbitrary. This also leads to the possibility of bound states at quasienergy $\varepsilon = \pi = -\pi$ which are protected by symmetry (*e.g.* in class BDI as discussed above, they can carry chirality). In fact, Floquet systems have been found where the classification of the effective Hamiltonian predicts no bound states, while numerical or optical simulations show protected edge modes.[99,149]

How to classify the topology of driven systems beyond the bands of an effective Hamiltonian has been the subject of a lot of recent research and is addressed in Chapters 2 and 3 in this thesis.

## 1.7 Quantum algorithms

The idea of quantum walks have been generalized to arbitrary bipartite graphs (or in fact any graph, using its bipartite double cover)[168], which allows the design of quantum algorithms that solves computational problems represented by such graphs.

Even though such algorithms are not the main topic of this thesis, they are a large field of application of quantum walks, and furthermore can often be understood in terms of the properties of quantum walks that we discussed above. In this section, we thus take a small detour and consider one of these algorithms, first presented in Ref. 162, and highlight their connection to topology.

*Quantum search on the hypercube* The algorithm we discuss solves the same problem as the famous Grover search algorithm.[72] In the problem, we want to find the solution to the problem $f(x^*) = 0$, where $x^* \in \{0,1\}^n$ i.e. $x$ is a bit string of length $n$. The function $f$ is not restricted, but we assume the solution $x^*$ to be unique.

The computation is performed by a quantum walk on the hypercube graph, formed by possible solutions $x$. The walker's position thus can be any bit string $x$ of length $n$, and during one step, the walker is allowed to move to any bit string $x'$ when $x$ and $x'$ only differ by a bit flip at one position, (see Fig. 1.4 for an illustration with $n = 3$).

*The oracle* The evaluation of the function $f(x)$ is performed by an *oracle* $O$. This oracle is an additional unitary evolution of the walker which "marks" the solution of $f(x) = 0$ by changing the phase of the walkers wave function on these points by $\pi$.* We thus have

$$O = 1 - 2\,|x^*\rangle\,\langle x^*| \tag{1.48}$$

For definiteness, we can even assume that the solution is $x^* = 00\ldots0$, because except for the application of the oracle, all parts of the algorithm are invariant under bit flips of the labels of the vertices, as will become apparent immediately.

*The quantum walk on the hypercube* The generalization of the one-dimensional quantum walk to this graph is rather straight-forward: Because at each time there are $n$ possible directions for the walker to go, we require an $n$-dimensional internal coin space (not a two-component spinor, as for the one-dimensional walker).

The coin rotation $R$ must be a unitary on that space, and should be invariant under bit flips. We could use a rotation around the symmetric state $|s\rangle$, defined by

$$|s\rangle = \frac{1}{\sqrt{n}} \sum_{i=1}^{n} |i\rangle\,, \tag{1.49}$$

which can be written as

$$R_\theta = e^{-i\theta}\,|s\rangle\,\langle s| + e^{i\theta}(1 - |s\rangle\,\langle s|), \tag{1.50}$$

*It must be understood that for the implementation of such an oracle, it is not necessary to know the target state $x^*$ explicitly; In fact, if $f$ can be computed efficiently with classical gates, the oracle can be implemented efficiently using quantum gates.

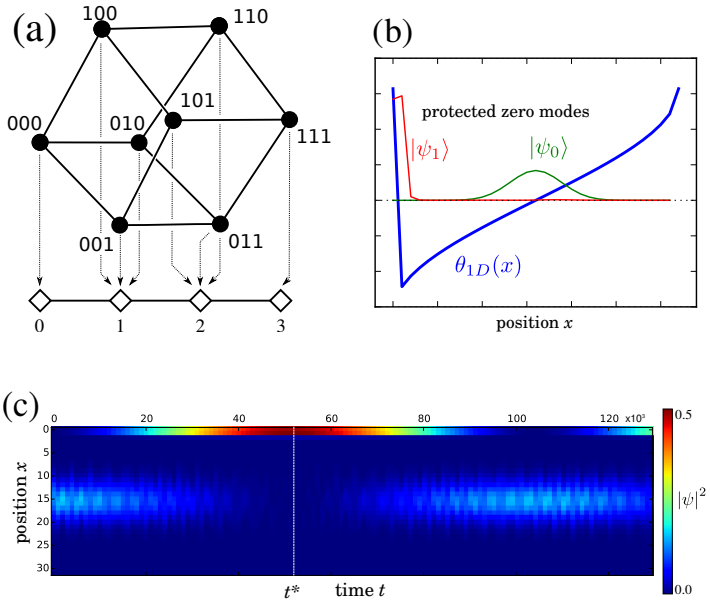


**Figure 1.4:** *(a)* The three-dimensional hypercube is mapped to a one-dimensional quantum walk by joining states which have the same distance to the oracle state $|0\rangle$. *(b)* The one-dimensional quantum walk has an effective $\theta_{1D} = \arcsin(1 - x/n)$. The oracle changes $\theta_{1D}(x = 0) = -\pi$ to $\pi$. This results is two bound states: $|\psi_0\rangle$, located around $x = n/2$, which corresponds to the totally delocalized state on the original hypercube, and $|\psi_1\rangle$, localized around the oracle state. The states are shown for $n = 32$, *(c)* The algorithm works by a beating between the initial state and the oracle state. We show this oscillation for $n = 32$. When measuring the position of the walker at time $t = t^*$, the probability of measuring the oracle state is almost 0.5.

and in order to achieve a maximal spreading speed, we can choose $\theta = \pi/2$. In fact, in the original description, the coin is chosen as a reflection around $|s\rangle$ instead, which differs from $R_{\pi/2}$ by a factor $i$.

The shift step then is a coin-dependent shift in the direction in which the coin is pointing, in other words, if the coin state is $|i\rangle$, the $i$th bit of $x$ is flipped.

The algorithm then proceeds by initializing the walker in a equal superposition of all possible states and then performing a quantum walk, applying

$$F = OSR \tag{1.51}$$

repeatedly. After $t = \frac{\pi}{2}\sqrt{2^n}$ repetitions, the position of the walker is

measured, and will result in the state marked by the oracle with high probability (almost 0.5).

*Projection to one dimension* The mechanism underlying this surprising result can be understood by projecting the walk on the hypercube to a one-dimensional walk on $n+1$ sites and two-dimensional coin (see Fig. 1.4a), where the position denotes the distance to the oracle state (if $x^* = 00\ldots0$, this is the number of 1's in the bit string, see Fig. 1.4) and the coin state is projected to either pointing towards or away from the oracle state. Omitting the action of the oracle, the result is a simple quantum walk, albeit with site-dependent rotation angle:

$$\theta_{1D} = \arcsin(1 - 2x_{1D}/n), \tag{1.52}$$

where $x_{1D}$ labels the sites of the reduced walk, see Fig. 1.4b.

*Topological bound states in 1D walk* Because the simple quantum walk changes its bulk winding number at $\theta = 0$, it ca be seen that this 1D walk features a topological phase transition at $x_{1D} = n/2$, and a corresponding chiral bound state is expected. In fact, this "bound state" is simply the result of projecting the equal superposition of all starting positions onto the 1D walk; this is just the initial condition of the described algorithm, and it in fact can be seen to be a zero-energy eigenstate of the system without the oracle.

We now consider the changes to the 1D walk when introducing the oracle operator. The oracle only acts on the target state, which is mapped to the state $x_{1D} = 0$ and in fact in the one-dimensional projected quantum walk, it turns out to be a change of the rotation angle $\theta_{1D}$ by $\pi$. This leads to the formation of a second topological phase transition, and a corresponding bound state.

The working of the algorithm is now clear: Because of the finite distance between the two bound states, they have an exponentially small, but finite overlap, leading to a splitting in quasi-energy $\Delta\varepsilon \propto 2^{-n/2}$, so that the application of the effective Hamiltonian leads to a very slow quantum beating between the two bound states at zero energy. The algorithm terminates after half a beating period, when the walker is in the bound state exponentially localized around the oracle state, see Fig. 1.4c.

## 1.8 This thesis

We finally give a short overview over the topics and main results of each of the following chapters.

### Chapter 2

Besides considering winding numbers of the bulk, it is also possible to characterize the topological quantum numbers of band insulators by calculating the scattering matrix of a half-infinite insulator at the energies of interest.[65] This matrix is directly related to the bound states emerging at an interface of two such systems, and can thus be used to classify the topological properties of the Hamiltonian, in accordance with the bulk-boundary correspondence. In fact, depending on the symmetries of the system, the topological quantum number at a certain energy can be expressed in terms of the determinant, trace, or Pfaffian of the scattering matrix.

In this chapter, we extend this approach to the Floquet scattering matrix of quantum walks, immediately identifying expressions for the additional quantum numbers required for Floquet systems. We use this result to map out the topological phase diagram of several quantum walk protocols with different symmetries.

### Chapter 3

The Su-Schrieffer-Heeger model (SSH model) is a one-dimensional tight binding model with alternating hopping strengths $u$ and $v$, originally devised to model the electronic structure of polymers with conjugated $\pi$-bonds. With fixed $u, v$, this system forms a one-dimensional topological insulator with chiral symmetry.

When driving the hopping strengths periodically in a symmetric way, the system becomes a topological Floquet insulator, with chiral symmetry still present. The Floquet operator of this system is very similar to that of quantum walks, and can in fact be mapped to quantum walks if the time-dependence of $u(t), v(t)$ is chosen piecewise constant.

In this chapter, we study the topological properties and bulk-boundary correspondence of the driven SSH model and find that in order to establish a bulk-boundary correspondence for both zero and $\pi$-quasienergy bound states, we need to calculate the winding number of the Floquet

operator in two different time frames, or, equivalently, consider the time evolution operator $U(T/2,0)$ which connects the two time frames.

## Chapter 4

In this chapter, we consider the simple quantum walk as presented in the introduction. However, we introduce an important modification, which is a non-linear self-interaction of the walker. To be precise, the local spin density $M(x) = \psi^\dagger(x)\sigma_z\psi(x)$ of the walker is taken to lead to a correction to the rotation angle $\theta(x) = \theta_0 + \delta\theta(M(x))$ in the next time step.

This self-interaction makes the time evolution in the bulk nonlinear, and a description in terms of a single particle Floquet operator is not longer possible. However, the interaction is chosen so that topologically protected bound states, which are present at domain boundaries in the linear model, are insensitive to this non-linearity, meaning that they still are a steady state solution of the non-linear time evolution.

We show that furthermore in this model, numeric simulation suggests that some of these modes are in fact attractive fixed points of the dynamics, meaning that independent of the initial conditions, the system approaches the same stable state at finite times. We corroborate this behavior by considering the non-linear Dirac equation obtained as a continuum approximation of the quantum walk for long wavelengths.

## Chapter 5

In this chapter we consider a driven system which is not driven periodically, but instead we consider a quench, where a parameter is varied from $-\infty$ to $\infty$, crossing a phase transition in between.

The system under consideration is a generalization of the single electron emitter,[30,31,52,64,121,136] where a quantum dot is coupled to a one-dimensional lead. The dot is assumed to have a bound state well below the Fermi energy $E_F$, which is thus occupied. A plunger gate is then used to control the energy of the bound state, moving it well above the Fermi energy. While the energy of the bound states crosses $E_F$, the particle will tunnel from the quantum dot and enter the lead as a localized excitation above the Fermi surface. Surprisingly, it has been recognized that this simple scheme to emit a single electron on top of a Fermi surface is very noiseless, in fact, at zero temperature and

in the limit of constant derivative of the energy of the bound state, the final state of the lead is precisely the ground state of the lead, with one particle added above the Fermi surface. Thus, even though the system is explicitly time dependent and the lead is assumed gapless, no additional particle-hole pairs are created.

In this chapter, we consider a generalization of this scheme to superconducting systems. Here, we change the phase across a topological Josephson junction as a function of time, thus driving the system through a fermion parity switch. Similarly, this leads to the emission of a particle, which now, due to the presence of superconductivity, will be a Bogoliubov quasiparticle, i.e. a coherent superposition of electron and hole.

We solve the scattering problem analytically for a minimal model and find again that no additional particle-hole pairs are created in the lead. Additionally, we give expressions for the charge of the emitted quasiparticle, which in general depends on both the coupling to the lead as well as the speed of the sweep. We find that for very slow (adiabatic) sweeps, the emitted particle is always either an electron or a hole, and that in order to obtain equal superposition, a very special coupling, a *Majorana filter*, is required.

## Chapter 6

In this chapter, unlike the previous chapters, we consider a classical transport problem of a solid state system. The theoretical issue considered, inspired by experiments that are also described in detail in this chapter, is that of magnetotransport in a hexagonal indium antimonide nanowire, which features strong spin-orbit coupling. Experimentally, the spin-orbit interaction strength can be determined by measuring the so-called weak localization and weak antilocalization, which are quantum corrections to the conductivity that depend on a small magnetic field in a characteristic manner.

However, the relation between magnetic field dependence and resulting spin-orbit strength estimates depend on the geometry of the problem. Because applying results for two-dimensional wires appeared as an oversimplification for the presented experiments, we used Monte Carlo simulation and the quasi-classical technique to model the three-dimensional geometry of the hexagonal nanowires.

The results of the simulation are used to interpret the experimental

data and furthermore explain an observed independence of weak localization on magnetic field direction as a coincidence for the parameters of the examined samples.

In regimes not accessible by current experiments, the simulations predict an interesting dependence of the weak localization corrections on the ratio $W/l_e$ with a fractional exponent, where $W$ is the radius of the wire and $l_e$ is the electronic mean free path.

# 2 Scattering theory of topological phases in discrete-time quantum walks

## 2.1 Introduction

The last decade has seen a systematic exploration of topological phases in band insulators and the protected low energy states that emerge at their boundaries.[75,143] From Majorana bound states at the ends of topological superconducting wires to the unique metallic surface state of three-dimensional topological insulators, a variety of boundary states can arise in this way. Their potential applications range from spintronics to topological quantum computation. As there are few real-life materials that are topological insulators,[12] there is an intense search for model systems that simulate topological insulators in the laboratory.[5,104,167]

Discrete-time quantum walks (DTQW)[175] are quantum generalizations of the random walk, with a quantum speedup that could be employed for fast quantum search[28] or even for general quantum computation.[119] They have been realized in many experimental setups, including atoms in optical lattices,[68,88] trapped ions,[157,184] and light in optical setups.[33,83,137,152,160,161] DTQWs are known to simulate topological insulators,[101] this was recently experimentally confirmed by the observation of edge states in an inhomogeneous quantum walk with photons.[99]

Beyond realizing entries in the periodic table of topological insulators,[150] DTQWs possess a richer structure of topological phases which is subject of ongoing research. The role of energy is taken over by quasienergy $\varepsilon$, that is $2\pi$-periodic in natural units, where $\hbar = 1$ and the unit of time is one timestep of the walk. This is a feature that quantum walks share with periodically driven lattice Hamiltonians,[36,116] for

which unique topological invariants have been found.[98] For both types of systems, topologically protected states may appear both at quasienergy $\varepsilon = 0$ and $\varepsilon = \pi$,[84] and states may be topologically protected even when all bands are topologically trivial.[97,149]

In this work we characterize topological phases of one dimensional DTQWs using a scattering matrix approach. This constitutes a generalization of methods developed for time-independent systems.[6,43,66] For DTQWs with gaps in the quasienergy spectrum at both $\varepsilon = 0$ and $\varepsilon = \pi$, we obtain the topological invariants as simple functions of the scattering matrix at these quasienergies. For unbalanced quantum walks, where there is an unequal number of left- and rightward shifts in a period, we find an integer number of perfectly transmitting unidirectional modes, that is equal to the quasienergy winding.[98] Our approach is particularly suitable to calculate the topological invariants of disordered quantum walks, as we demonstrate in an example.

This chapter is structured as follows. After defining our notation for one-dimensional discrete-time quantum walks in the next section, we adapt the concept of a scattering matrix for DTQWs in Sec. 2.3. In Sec. 2.4 we discuss the influence of particle-hole, time-reversal and chiral symmetry on the scattering matrix. The central result of this chapter, the topological invariants of DTQWs, are shown in Sections 2.5 and 2.6. We illustrate our approach in Sec. 2.7 with concrete examples. Finally, Sec. 2.8 discusses how the topological invariants can be directly measured in a quantum walk experiment.

## 2.2 Discrete-time quantum walks

We consider a particle (walker) with $N$ internal states (coin states) on a one-dimensional lattice, whose wave function can be written as

$$|\Psi\rangle = \sum_{x\in\mathbb{Z}} \sum_{n=1}^{N} \Psi(x,n)|x,n\rangle\,. \tag{2.1}$$

Here $x$ denotes the discrete position and $n$ the internal state of the walker.

The walker is subjected to a periodic sequence of two different types of operations: shifts and rotations. Measuring time $\tau$ in units of the

period, the dynamics are given by

$$|\Psi(\tau+1)\rangle = \mathscr{F}\,|\Psi(\tau)\rangle\,, \tag{2.2}$$

$$\mathscr{F} = R_{M+1} S_M R_M \ldots S_1 R_1. \tag{2.3}$$

The time-evolution operator over one period, a.k.a. Floquet operator $\mathscr{F}$, consists of shift operators $S_j$ and rotation operators $R_j$.

Each shift operation $S_j$, shifts a chosen internal state $n_j$ by one lattice site, either to the right (+) or to the left (−). In formulas $S_j = S^{\pm}_{n_j}$, with

$$S^{\pm}_n = \sum_{x\in\mathbb{Z}} \Big[\, |x\pm 1, n\rangle\langle x, n| + \sum_{n'\neq n} |x, n'\rangle\langle x, n'| \,\Big]. \tag{2.4}$$

For each internal state $n$, we fix a direction $s_n \in \{+1, -1, 0\}$ throughout the protocol. We require that the operators $S_j$ are compatible with each other, i.e. no state is shifted to the left by some $S_j$ and to the right by others. Accordingly, there are three sets of internal states: those shifted to the right, $n \in M_+$, those shifted to the left, $n \in M_-$, and those not shifted at all, $n \in M_0$. For each internal state $n$, we use $d_n$ to denote the number of shift operators $S$ in a period that shift the state,

$$d_n = \sum_{j=1}^{M} \delta_{n_j, n}. \tag{2.5}$$

Rotations mix the internal degrees of freedom, but are local in real space,

$$R_j = \sum_{x\in\mathbb{Z}} |x\rangle\langle x| \otimes R_j(x). \tag{2.6}$$

Each $R_j(x)$ is a $U(N)$ operation. For translation invariant quantum walks, $R_j(x)$ is independent of $x$.

The time evolution (2.3) is a stroboscopic simulation of an effective, time-independent Hamiltonian

$$H_{\text{eff}} \equiv i \log \mathscr{F}. \tag{2.7}$$

For definiteness, the branch cut of the logarithm is chosen such that all quasienergies, the eigenvalues of $H_{\text{eff}}$, are restricted to $\varepsilon \in [-\pi, \pi]$. In the presence of translational symmetry, quantum walks thus have a band structure, just like time-independent systems.

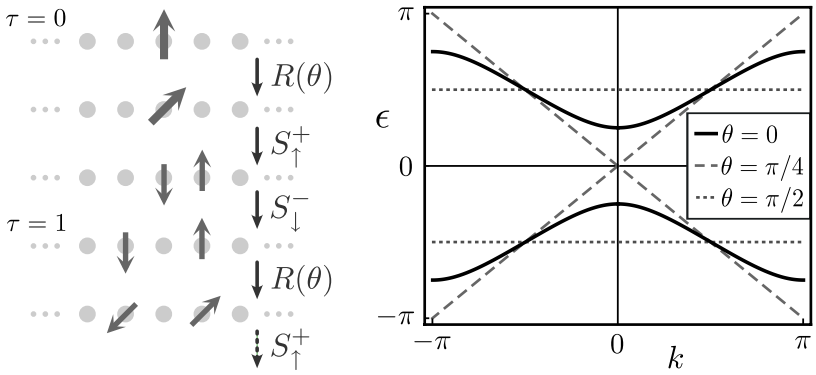


**Figure 2.1:** Left: Propagation of a particle in the simple quantum walk, initialized in spin-up state on a single site. Right: band structure of the simple quantum walk for different values of the rotation angle $\theta$. Generically the spectrum is gapped around quasienergies $\epsilon = 0, \pi$ except for the special cases $\theta = 0, \pi$.

As an example, Fig. 2.1 illustrates the protocol and the quasienergy band structure of the simple quantum walk,

$$\mathscr{F} = S_{\downarrow}^{-} S_{\uparrow}^{+} R(\theta). \tag{2.8}$$

The walker here has only two internal states, which we label by $\uparrow$ for $n = 1$ and $\downarrow$ for $n = 2$, and refer to as spin. First the spinor is rotated by an angle $\theta$ on the Bloch sphere,

$$R(\theta) = \sum_{x} |x\rangle\langle x| \otimes e^{-i\theta\sigma_y}. \tag{2.9}$$

Subsequently $S_{\uparrow}^{+}$ shifts the spin-up component of the state to the right and $S_{\downarrow}^{-}$ the spin-down component to the left.

Note that the Floquet operator is not unique for a given quantum walk protocol. For example we could just as well choose

$$\mathscr{F} = S_{\uparrow}^{+} R(\theta) S_{\downarrow}^{-}, \tag{2.10}$$

for the Floquet operator of the simple quantum walk, since it produces the same protocol of operations $(\ldots S_{\uparrow}^{+} R(\theta) S_{\downarrow}^{-} S_{\uparrow}^{+} R(\theta) S_{\downarrow}^{-} \ldots)$. Describing a quantum walk by a specific Floquet operator amounts to fixing a starting time, or time frame,[14] for the period of the walk. Changing the starting time of the period is much like choosing a different unit cell

in a crystal. It corresponds to a unitary transformation on the Floquet operator $\mathscr{F}$, and, as a result, cannot change the quasienergy spectrum. Nevertheless, the choice of the correct time frame can be crucial when investigating symmetries and topological properties as we shall discuss in the course of this chapter.

## 2.3 Scattering in quantum walks

To study DTQWs in a scattering setting, we maintain the whole quantum walk protocol only in a central region ($0 \le x < L$), which we want to analyze. In the remaining regions we omit the rotations,

$$R_j(x<0) = R_j(x \ge L) = \mathbb{1}_N \quad \text{for all } j. \tag{2.11}$$

In this way, a left ($x < 0$) and a right lead ($x \ge L$) are formed. The scattering setting is illustrated in Fig. 2.2 for the example of the simple quantum walk. Deep in the leads, a particle with internal state $n$ is simply shifted by $d_n$ sites in direction $s_n$ in each period,

$$\begin{aligned} \mathscr{F}\,|x,n\rangle = S_M \ldots S_1\,|x,n\rangle = |x+s_n d_n, n\rangle\,, \\ \text{for} \quad x < -d_n \quad \text{or} \quad x > L + d_n. \end{aligned} \tag{2.12}$$

An infinite lead of this type has propagating solutions at all quasienergies.

A natural basis for propagating states in the two leads ($l$,$r$) is given by the states

$$\begin{aligned} |l_{n,d,\varepsilon}\rangle &= \sum_{j=-\infty}^{0} e^{is_n\varepsilon j}\,|jd_n - d, n\rangle\,, \\ |r_{n,d,\varepsilon}\rangle &= \sum_{j=1}^{\infty} e^{is_n\varepsilon j}\,|L + jd_n - d, n\rangle\,, \end{aligned} \tag{2.13}$$

for $n \in M_+ \cup M_-$. These are quantum walk equivalents of plane waves, restricted to the left/right lead and normalized to carry the same particle current. Unlike true plane waves,[125] they only occupy every $d_n$th site and the different sublattices that arise in this way are indexed by $d$, restricted to $1 \le d \le d_n$.

In a scattering problem, an incoming mode incident on a central region is scattered into outgoing modes. Consider a mode $|l_{n,d,\varepsilon}\rangle$ in the

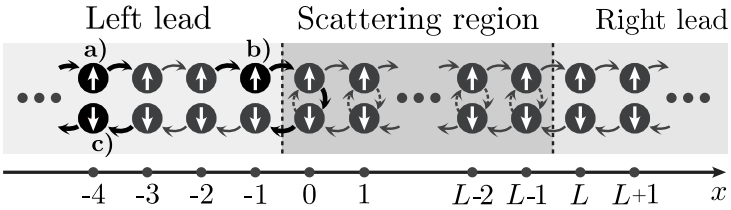


**Figure 2.2:** Scattering setting for the simple quantum walk, Eq. (2.8). The lattice is divided in three regions: a left lead ($x < 0$), a right lead ($x \geq L$) and a scattering region in between. Each site contains two internal spin states. The shift operators of the protocol act throughout the whole system (solid black arrows), shifting a walker with state $\uparrow$ to the right, and state $\downarrow$ to the left. Rotations (dotted arrows) only change the internal state of the walker in the scattering region. **(a)** A walker with spin-up in the left lead is incident on the scattering region. **(b)** Once it reaches $x = 0$, it is subject to rotations and acquires a spin-down component, which is shifted in the opposite direction. The purple arrows illustrate a possible reflection process. **(c)** A walker with spin-down is propagated away from the scattering region. While **(a)**-**(c)** depict the scattering in time, the scattering states we consider are the corresponding quasienergy eigenstates.

left lead, with $s_n = +1$, so that it is incident on the central region. It is scattered into outgoing modes $|\Psi^{\text{out}}_{L,R}\rangle$ in both the left and the right lead. The corresponding scattering state is a Floquet eigenstate with quasienergy $\varepsilon$,

$$|\Psi_{n,d,\varepsilon}\rangle = |l_{n,d,\varepsilon}\rangle + |\Psi_C\rangle + |\Psi^{\text{out}}_L\rangle + |\Psi^{\text{out}}_R\rangle, \tag{2.14}$$

$$|\Psi^{\text{out}}_L\rangle = \sum_{n' \in M_-} \sum_{d'} r_{n'd',nd}(\varepsilon)\, |l_{n',d',\varepsilon}\rangle, \tag{2.15}$$

$$|\Psi^{\text{out}}_R\rangle = \sum_{n' \in M_+} \sum_{d'} t_{n'd',nd}(\varepsilon)\, |r_{n',d',\varepsilon}\rangle, \tag{2.16}$$

where $|\Psi_C\rangle$ denotes the contribution of the state in the central region. This defines the matrix elements of both the reflection matrix $r(\varepsilon)$ and the transmission matrix $t(\varepsilon)$.

Using the Floquet operator of the scattering setting, we can write down the scattering state explicitly,

$$|\Psi_{n,d,\varepsilon}\rangle = \sum_{\nu=-\infty}^{\infty} e^{i\varepsilon\nu} \mathscr{F}^\nu |-d,n\rangle. \tag{2.17}$$

This really is a stationary state with quasienergy $\varepsilon$, as can be seen by application of $\mathscr{F}$ on Eq. (2.17). State $|\Psi_{n,d,\varepsilon}\rangle$ contains the correct incoming plane wave, since

$$|l_{n,d,\varepsilon}\rangle = \sum_{\nu=-\infty}^{0} e^{i\varepsilon\nu} \mathscr{F}^\nu |-d,n\rangle. \tag{2.18}$$

Furthermore, this state contains no incoming plane waves other than $|l_{n,d,\varepsilon}\rangle$, since terms in the above sum with $\nu > 0$ correspond to states that can be reached by propagating $|-d,n\rangle$ forward in time: they are in the central region and in the outgoing modes.

The reflection matrix elements are found from projections of $|\Psi_{n,d,\varepsilon}\rangle$ onto outgoing ($s_{n'} = -1$) states in the left lead, $|l_{n',d',\varepsilon}\rangle$. Using the definitions above, we obtain

$$\begin{aligned} r_{n'd',nd}(\varepsilon) &= \langle -d',n'| \sum_{\nu=-\infty}^{\infty} e^{i\varepsilon\nu} \mathscr{F}^{\nu} |-d,n\rangle \\ &= \langle -d',n'|(1-e^{i\varepsilon}\mathscr{F})^{-1}|-d,n\rangle\,. \end{aligned} \tag{2.19}$$

Similarly, the transmission matrix elements are

$$t_{n'd',nd}(\varepsilon) = \langle L-d',n'|(1-e^{i\varepsilon}\mathscr{F})^{-1}|-d,n\rangle\,. \tag{2.20}$$

for all $n'$ with $s_{n'} = +$. For numerical evaluation, the reflection and transmission matrices can be calculated from this formula using Floquet operators that are truncated in the leads. We discuss this in detail in Appendix 2.A.

Scattering matrices for DTQWs have been considered in a different formalism by Feldman and Hillery.[60,61] With an elegant mathematical duality transformation, they assign the walker to the edges rather than the nodes. We chose a different route from theirs, as outlined in this Section, for two reasons. First, our approach is easier to apply to multistep walks (i.e., DTQWs where the number of steps per cycle is $M > 2$). Second, and this is the more important reason: our approach allows for a transparent treatment of the relevant symmetries of the system. This is the topic we turn to in the next Section.

## 2.4 Symmetries of quantum walks

The standard band theory of topological insulators describes topological phases of Hamiltonians depending on three discrete symmetries: time-reversal symmetry (TRS), particle-hole symmetry (PHS), and chiral symmetry (CS). In this section we show how the definition of these symmetries translates to the Floquet operator and the scattering matrix of DTQWs.

A quantum walk has TRS if an antiunitary operator $\mathscr{T} = KU_T$ exists such that

$$U_T^\dagger \mathscr{F}^* U_T = \mathscr{F}^{-1} \quad \Leftrightarrow \quad U_T^\dagger H_{\text{eff}}^* U_T = H_{\text{eff}}. \tag{2.21}$$

Here $K$ denotes complex conjugation in the basis used in Eq. (2.1), and $U_T$ is a unitary operator acting on the internal state only. The TRS operator $\mathscr{T}$ transforms the time-evolution operator $\mathscr{F}$ into its inverse, justifying the term "time-reversal".

If a unitary operator $\Gamma$ achieves time reversal, this is referred to as CS,

$$\Gamma^\dagger \mathscr{F} \Gamma = \mathscr{F}^{-1} \quad \Leftrightarrow \quad \Gamma^\dagger H_{\text{eff}} \Gamma = -H_{\text{eff}}. \tag{2.22}$$

Finally, consider an anti-unitary operator $\mathscr{P} = KU_P$ that transforms the Floquet operator into itself,

$$U_P^\dagger \mathscr{F}^* U_P = \mathscr{F} \quad \Leftrightarrow \quad U_P^\dagger H_{\text{eff}}^* U_P = -H_{\text{eff}}. \tag{2.23}$$

A symmetry of this form is referred to as PHS, because of its existence in superconductors. In quantum walks, there is no natural concept of particles and holes, but a symmetry of this form might still be present.

Like in the symmetry classification of time-independent problems, the unitary symmetries present in the system are used to block diagonalize the Floquet operator (and, as a consequence, the effective Hamiltonian) before PHS, TRS and CS are analyzed. Then, $\mathscr{P}$ and $\mathscr{T}$, if present, will square to plus or minus unity, and chiral symmetry is related to the two by $\Gamma \propto \mathscr{T}\mathscr{P}$, if both are present. The possible presence or absence, as well as the squares of these symmetries, gives ten possible symmetry classes, which are referred to by so-called Cartan labels.[9,150]

We now turn to the discussion of symmetries in a scattering setup. The situation is is very similar to systems whose dynamics are governed by time-independent Hamiltonians. We thus refer the reader especially to Appendix A of Ref. 65.

If a scattering setup possesses one of the symmetries above, we can consider the action of the symmetry operators on the modes in the leads. TRS and CS reverse the action of the time evolution operator, and thus map incoming modes to outgoing modes and vice versa, while PHS will act on these spaces separately.

| Symmetry class | $\mathscr{T}^2$ | $\mathscr{P}^2$ | $\Gamma$ | $\mathcal{Q}_X = \mathcal{Q}_{X,0} \times \mathcal{Q}_{X,\pi}$ |
|---|---|---|---|---|
| AIII | $\times$ | $\times$ | ✓ | $\frac{1}{2}\mathrm{Tr}\, r(0) \times \frac{1}{2}\mathrm{Tr}\, r(\pi)$ |
| CII | $-1$ | $-1$ | ✓ | $\frac{1}{2}\mathrm{Tr}\, r(0) \times \frac{1}{2}\mathrm{Tr}\, r(\pi)$ |
| BDI | $+1$ | $+1$ | ✓ | $\frac{1}{2}\mathrm{Tr}\, r(0) \times \frac{1}{2}\mathrm{Tr}\, r(\pi)$ |
| D | $\times$ | $+1$ | $\times$ | $\frac{1}{2}\mathrm{Det}\, r(0) \times \frac{1}{2}\mathrm{Det}\, r(\pi)$ |
| DIII | $-1$ | $+1$ | ✓ | $\frac{1}{2}\mathrm{Pf}\, r(0) \times \frac{1}{2}\mathrm{Pf}\, r(\pi)$ |

**Table 2.1:** Symmetry classes with non-trivial topological invariants in gapped one-dimensional DTQWs. For TRS and PHS, the table gives the square values of the symmetry operators. For CS, existence is indicated by ✓. The full topological invariant $\mathcal{Q}_X$ is composed of invariants $Q_{X,\varepsilon}$ at quasienergies $\varepsilon = 0, \pi$ inside the two gaps of the quasienergy spectrum. The invariants as given in the table apply after a basis change on the reflection matrix, as detailed in Appendix 2.B.

We thus can write a time-reversed incoming state as a superposition of outgoing states. In the left lead this reads:

$$\mathscr{T}\,|l_{n,d,\epsilon}\rangle = \sum_{n' \in M_-} Q_{T,n'n}\,|l_{n',d,\epsilon}\rangle \text{ for } n \in M_+. \tag{2.24}$$

In the same manner, time-reversed outgoing states are superpositions of incoming states, with coefficients captured in the left lead by a matrix $V_T = \mathscr{T}^2 (Q_T)^T$. Similarly, the action of CS is given by matrices $Q_\Gamma$ and $V_\Gamma = \Gamma^2 Q_\Gamma^\dagger$. PHS on the other hand acts on right and left moving states separately, and we write

$$\mathscr{P}\,|l_{n,d,\epsilon}\rangle = \sum_{n' \in M_\pm} Q_{P\pm,n'n}\,|l_{n',d,\epsilon}\rangle \text{ for } n \in M_\pm. \tag{2.25}$$

Here the matrices $V_{P+}$ and $V_{P-}$ are independent and, in general, can have different dimensions.

The symmetries of the Floquet operator $\mathscr{F}$ translate to properties of the reflection matrix $r$:

$$r(\varepsilon) = Q_T\, r(\varepsilon)^T V_T^\dagger, \tag{2.26}$$

$$r(\varepsilon) = Q_\Gamma\, r(-\varepsilon)^\dagger V_\Gamma^\dagger, \tag{2.27}$$

$$r(\varepsilon) = Q_{P-}\, r(-\varepsilon)^* Q_{P+}^\dagger. \tag{2.28}$$

There is an important caveat here. The Floquet operator, and, consequently, the effective Hamiltonian and the scattering matrix, all depend

on the choice of time frame, as in the example of Eq. (2.10). As a consequence, the same DTQW can be seen to have a symmetry in one timeframe, while this symmetry might be hidden in another timeframe — this holds especially for TRS and CS. Therefore, finding the symmetries and the topological invariants includes going into the proper timeframe. In this section and in the rest of the chapter, we assume that this work has been done and that we are in a timeframe where the symmetries are explicit.

There are two special quasienergies: As can be seen from Eqs. (2.27) and (2.28), CS and PHS yield special constraints on the scattering matrix if $\varepsilon = -\varepsilon$, which, due to the periodicity of quasienergy, is fulfilled at both $\varepsilon = 0$ and $\varepsilon = \pi$. As we show in the following, this has the consequence that for DTQWs, topological invariants come in pairs.

## 2.5 Topological invariants of gapped quantum walks

In this section we consider balanced quantum walks, where the number $n_+$ of shift operators that shift to the right equals the number $n_-$ of shift operators that shift to the left in a period. For these walks, the quasienergy band structure generically has gaps around the special quasienergies $\varepsilon = 0$ and $\varepsilon = \pi$. Then, the transmission amplitudes at the two quasienergies are exponentially small in system size $L$, and, in the limit of large system size, the reflection blocks, $r(0)$ and $r(\pi)$, become unitary matrices.

### 2.5.1 Topological invariants

In five of the ten symmetry classes, unitarity of the reflection matrix allows us to define topological invariants, along the lines of the scattering theory of topological insulators and superconductors.[66] These classes are AIII, CII, D, BDI and DIII, as defined in Table 2.1, where we also summarize the main results of this section.

As a first step towards defining the topological invariants, a change of basis is performed separately for both in- and outgoing lead states, to simplify Eqs. (2.26), (2.27), and (2.28). Concrete recipes for the basis transformations are presented in Appendix 2.B for each class. In

the thus standardized form, the reflection matrices obey the following relations,

$$r(\epsilon) = r^*(-\epsilon) \qquad \text{for class D,} \tag{2.29}$$

$$r(\epsilon) = r^*(-\epsilon) = -r^T(\epsilon) \qquad \text{for class DIII,} \tag{2.30}$$

$$r(\epsilon) = r^\dagger(-\epsilon) \qquad \text{for classes AIII, CII and BDI,} \tag{2.31}$$

which we need to define the topological invariants. These follow from PHS, PHS + TRS and CS respectively after the simplifying basis changes.

In class D, $r(0)$ and $r(\pi)$ are real and due to unitarity they are orthogonal matrices. Hence they have determinant $\pm 1$. Four topologically distinct situations arise, distinguished by the $\mathbb{Z}_2 \times \mathbb{Z}_2$ invariant

$$\mathcal{Q}_{\mathrm{D}} = \tfrac{1}{2}\mathrm{Det}[r(0)] \times \tfrac{1}{2}\mathrm{Det}[r(\pi)] \quad \text{for class D.} \tag{2.32}$$

In symmetry class DIII, the reflection matrices $r(0)$ and $r(\pi)$ are both real and antisymmetric. Therefore, the invariant of (2.32), will be $(\frac{1}{2}, \frac{1}{2})$, as the eigenvalues of real antisymmetric matrices are purely imaginary and come in complex conjugate pairs. However, the determinant of an antisymmetric matrix is the square of a function of the matrix, the Pfaffian. The Pfaffian in this case can take values $\pm 1$. Thus, again four topologically different cases can be distinguished,

$$\mathcal{Q}_{\mathrm{DIII}} = \mathrm{Pf}[r(0)] \times \mathrm{Pf}[r(\pi)] \quad \text{for class DIII.} \tag{2.33}$$

In symmetry classes AIII, BDI, CII the reflection blocks $r(0)$ and $r(\pi)$ are Hermitian and unitary. Thus their eigenvalues are pinned to $\pm 1$ and their traces are quantized to integer values. This is expressed by the $\mathbb{Z} \times \mathbb{Z}$ topological invariant

$$\mathcal{Q}_{\mathrm{ch}} = \tfrac{1}{2}\mathrm{Tr}[r(0)] \times \tfrac{1}{2}\mathrm{Tr}[r(\pi)] \quad \text{for classes AIII,CII,BDI.} \tag{2.34}$$

In class CII, the traces can only take even integer values due to Kramers degeneracy of the scattering states. In principle, this invariant is also defined for $i\,r(0)$ and $i\,r(\pi)$ in symmetry class DIII, which we described before, but will always take the trivial value $(0,0)$, due to the antisymmetry of $r$.

In combination with the scattering formalism in Sec. 2.3, the topological invariants $\mathcal{Q}_{\mathrm{D}}$, $\mathcal{Q}_{\mathrm{DIII}}$ and $\mathcal{Q}_{\mathrm{ch}}$, are the main results of this work. Our approach is in agreement with the most recent analysis of topology

in DTQWs from a Floquet operator perspective,[14] as we will demonstrate for three examples in the next section. Similar invariants exist for reflection matrices of time-independent systems at zero energy,[66] but the time-periodicity of DTQWs leads to an extra contribution at quasienergy $\pi$.

### 2.5.2 Boundary states

The main reason bulk topological invariants are interesting is that they can be used to predict the number of protected midgap states at an interface between two bulk systems.[75] This applies to inhomogeneous DTQWs that have two domains, A ($x < 0$) and B ($x > 0$), governed by different quantum walk protocols, given that the complete system has the right combination of symmetries. If the topological invariant $\mathcal{Q}_X = \mathcal{Q}_{X,0} \times \mathcal{Q}_{X,\pi}$ with $X \in$ {D,DIII,ch} changes across the interface by $\Delta\mathcal{Q}_X = \Delta\mathcal{Q}_{X,0} \times \Delta\mathcal{Q}_{X,\pi} = \mathcal{Q}_X^A - \mathcal{Q}_X^B$, it can be shown that a number of $|\Delta\mathcal{Q}_{X,\{0,\pi\}}|$ quasienergy eigenstates are guaranteed to exist at quasienergies $\varepsilon = 0, \pi$ inside the gaps. These are bound to the interface and protected by the change of topological invariant. A full discussion based on reflection matrices is provided in Appendix 2.C.

In order to interface two DTQW protocols, such that they form an inhomogeneous system, the two protocols have to be compatible (we explain what we mean by this below). The shift operators are nonlocal, and thus to ensure that the Floquet operator of the combined system is unitary, they have to be applied throughout the system at the same time, and to the same internal states. Thus, two DTQW protocols A and B are compatible if $S_j^A = S_j^B$ for every $j$. The two DTQW protocols can only differ in their rotations.

Note that there is no unique DTQW analogue of open boundary conditions. Thus the bulk topological invariant alone does not predict the number of topologically protected edge states at the ends of a finite line segment on which an otherwise homogeneous DTQW takes place. Edge states can exist, but their number depends on the way the walk is terminated.[13] This is analogous to the situation of time-independent Hamiltonian systems with chiral symmetry.[66]

Note further that the values of the topological invariants depend on the starting time of the period of the DTQW, i.e., the choice of time frame for the Floquet operator. Nevertheless, the correct number of protected boundary states is obtained from the individual topological invariants

of two interfaced quantum walk domains when their starting times are chosen such that the walks are interfacable.

## 2.6 Topological invariant of unbalanced quantum walks

When a period of the quantum walk protocol contains a different number of shift operators that shift to the right than shift operators that shift to the left, $n_+ \neq n_-$, the quasienergy bandstructure shows a winding in quasienergy space.[98] This unique type of topology only can occur because of the $2\pi$-periodicity of quasienergy space. From a transport point of view, such a winding is produced when particles are pumped through the one dimensional system. A simple example is given by $F = S_{\uparrow}^{+}$ for which the quasienergy band structure is given by the raising half of the green dotted line in Fig. 2.1.

The scattering matrix of such a system has an unusual form since the reflection blocks $r$ and $r'$ of the scattering matrix are rectangular matrices of size $n_- \times n_+$ and $n_+ \times n_-$ respectively, while the transmission blocks are square matrices of differing sizes: $n_+ \times n_+ (t)$ and $n_- \times n_-(t')$. The ranks of the matrix products $rr^\dagger$ and $r'r'^\dagger$ is thus at most as large as $\min(n_+, n_-)$ and one of them has at least $|n_+ - n_-|$ zero eigenvalues. Due to the unitarity of the scattering matrix, $|n_+ - n_-|$ of the transmission eigenvalues of the larger transmission block have thus to be unity for all quasienergies. These perfectly transmitting channels in only one direction reflect the charge pumping through the system. Hence the topology of the quantum walk can be read off from the scattering matrix through the topological invariant

$$\mathscr{I} = \dim(t) - \dim(t'). \tag{2.35}$$

## 2.7 Examples

In this section, we consider three examples for gapped DTQWs and demonstrate how their topological properties can be analyzed by the scattering matrix approach. We first discuss the so-called split-step walk,[101] which includes the simple quantum walk of Eq. (2.8) as a special case. We then discuss a generalization of this protocol, which

contains four shift operators per period.[14] Depending on the choice of parameters, it can fall into several of the relevant symmetry classes, realizing either $\mathcal{Q}_{\mathrm{D}}$ or $\mathcal{Q}_{\mathrm{ch}}$. The third example has a larger internal space and is characterized by the invariant $\mathcal{Q}_{\mathrm{DIII}}$.

Finally, we show that the scattering matrix approach can also be used to define topological invariants in the presence of disorder and illustrate this using the simple quantum walk with disordered rotation angles.

### 2.7.1 Split-step walk

Extending the DTQW of Eq. (2.8) by adding another rotation, we obtain the so-called split-step walk[97]

$$\mathcal{F} = S_{\uparrow}^{+} R_2 S_{\downarrow}^{-} R_1. \tag{2.36}$$

Here, $R_j = R(\theta_j)$ is a rotation about the $y$ axis as defined in Eq. (2.9). The split-step walk is thus parametrized by two angles $\theta_1, \theta_2$. This DTQW has two internal states ($N = 2$), again referred to as a spin, with spin-up propagating to the right, and spin-down propagating to the left. Since $d_1 = d_2 = 1$, according to Sec. 2.3, the reflection matrix is a $1 \times 1$-matrix.

To find the topological properties of the split-step walk, we first need to understand its symmetries. According to Eq. (2.9), the rotation matrices are real matrices. The same applies for the shift matrices in position basis, so that $\mathcal{F}$ will be real and thus have PHS, with $\mathcal{P} = K$.[101] The protocol also has a chiral symmetry. This can be seen by choosing a different time frame,[14]

$$\mathcal{F}' = \sqrt{R_1} S_{\uparrow}^{+} R_2 S_{\downarrow}^{-} \sqrt{R_1}, \tag{2.37}$$

so that chiral symmetry is given by $\Gamma = \sigma_x$, which can be seen from $\sigma_x S_{\uparrow} \sigma_x = S_{\downarrow}^{-1}$ and $\sigma_x R \sigma_x = R^{-1}$. Thus the system falls in symmetry class BDI. Note that also the simple quantum walk is of this form if written as in Eq. (2.10), with $\theta_1 = 0$.

We calculated the reflection matrix in Eq. (2.19) numerically for the Floquet operator $\mathcal{F}'$, following the procedure described in Appendix 2.A. The resulting class BDI invariant $\mathcal{Q}_{\mathrm{ch}}$ is plotted in Fig. 2.3 as a function of the rotation angles $\theta_1, \theta_2$ for system size $L = 50$. The calculation is simplified by the fact that the chiral symmetry of $r$ is in its canonical form, Eq. (2.31), because $V_\Gamma = 1$. The topological invariant $\mathcal{Q}_{\mathrm{ch}}$ is thus

in fact half of the reflection matrix's only element, taken at energies 0 and $\pi$, with values $\mathcal{Q}_{\mathrm{ch}} \in (\pm\frac{1}{2}, \pm\frac{1}{2})$.

The results plotted in Fig. 2.3 are in agreement with topological invariants that were derived directly from the Floquet operator, by counting gap closings in the dispersion relation.[13]

### 2.7.2 Four-step walk

We now turn to a multistep walk, choosing a longer sequence that includes three different rotations,

$$\mathcal{F} = S_{\downarrow}^{-} R_3 S_{\downarrow}^{-} R_2 S_{\uparrow}^{+} R_1 S_{\uparrow}^{+}. \tag{2.38}$$

Here, we also allow for more general rotations

$$R(\theta, \chi) = \sum_x |x\rangle\langle x| \otimes e^{-i\theta(\sigma_y \cos\chi + \sigma_z \sin\chi)}, \tag{2.39}$$

so that the walk is parametrized by six angles, $\theta_j, \chi_j$, with $j \in 1,2,3$. This four-step walk has been introduced before in Ref. 14.

For the four-step walk, there are still only two internal states ($N = 2$), but the number of shift operators is larger ($d_\uparrow = d_\downarrow = 2$), leading to a $2\times 2$ reflection matrix. The symmetries of the system are fixed by restricting the parameters to certain subsets. To be precise, if we set $\chi_{1,2,3} = 0$, the rotation matrices are real, and the system has PHS, given by $\mathcal{P} = K$. On the other hand, if we require $R_1 = R_3$, the system has chiral symmetry given by $\Gamma = \sigma_x$. This walk thus serves as an illustrative example for the symmetry classes D, AIII, or BDI. We concentrate on the BDI case, where all $\chi = 0$ and $\theta_1 = \theta_3$.

In Fig. 2.3, we show the numerical result for the invariant $\mathcal{Q}_{\mathrm{ch}}$ from the scattering matrix. As defined in Sec. 2.5, the invariant is half the trace of the reflection block at quasienergies 0 and $\pi$, and here each of the two elements can take the values $\{-1, 0, 1\}$. Similar to the split-step walk above, the symmetry relations for $r$ are in their standard form already, so no basis transformation is required.

Our result for the the phase diagram agrees with Fig. 2 of Ref. 14, where the topological invariant was calculated by combining winding numbers from two different time frames. Interestingly, with the approach of this chapter, it suffices to consider the protocol in one time frame. This is because the scattering matrix method uses all possible

plane waves to probe the quantum walk, which reach the scattering region at different times. The reflection matrix thus contains information about the dynamics of the system during one timestep.

Quantum walks for classes AIII and D are obtained from this walk by breaking either particle-hole or chiral symmetry. In the former case, the topological invariant does not change, while in the latter case, the topological invariant is reduced to $\mathbb{Z}_2 \times \mathbb{Z}_2$.[14]

### 2.7.3 Symmetry class DIII

The construction of a DTQW that realizes $\mathscr{T}^2 = -1$ is more involved; some proposals have been given in Ref. 101. As an example, we now consider a protocol with DIII symmetry, which is constructed with four internal states $N = 4$, of which two are right-moving and two are left-moving. We consider these as two instances of a two-state quantum walk, which are governed by

$$\mathscr{F} = \begin{pmatrix} F_1 & 0 \\ 0 & F_2 \end{pmatrix} e^{i\sigma_z \tau_y \gamma} \begin{pmatrix} F_2 & 0 \\ 0 & F_1 \end{pmatrix}, \tag{2.40}$$

where $\sigma_i$ are Pauli matrices acting on the spin of each copy of the two-state quantum walk, while $\tau_y$ is a Pauli matrix that mixes the two instances. Here, $F_1$ and $F_2$ are both Floquet operators of the simple quantum walk in the form of Eq. (2.10), with different parameters $\theta_{1/2}$. The additional angle $\gamma$ provides a way to couples the two instances of the walk. This quantum walk has CS with $\Gamma = i\sigma_x\tau_y$, PHS with $\mathscr{P} = K$, and thus TRS with $\mathscr{T} = \sigma_x\tau_y K$, falling into symmetry class DIII.

According to Sec. 2.5, the calculation of the topological invariant from the reflection block $r$ requires us to find the basis in which $r$ is antisymmetric, in order to calculate the Pfaffian. From Appendix 2.B, it follows that this property is fulfilled by the matrix $\tilde{r} = V_T r$, so that the topological invariant in this example can be calculated as

$$\mathscr{Q}_{\mathrm{DIII}} = \mathrm{Pf}\big(\tau_y r(0)\big) \times \mathrm{Pf}\big(\tau_y r(\pi)\big). \tag{2.41}$$

The resulting phase diagram of this protocol, with $\theta_2 = 0$, is displayed in Fig. 2.3 (c). It realizes all possible topological phases of the symmetry class. Non-generic features can be observed at $\theta_1 = 0, \pi$ in the phase diagram, signalling unprotected gap closings at which the topological invariant does not change.

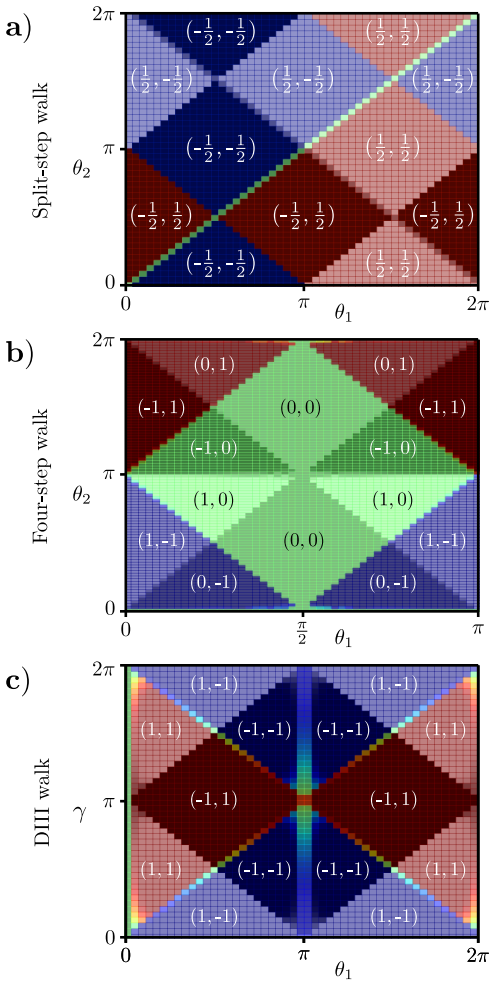


**Figure 2.3:** Topological phase diagrams for three quantum walk examples, obtained from the scattering matrix approach. All phases are labelled by their topological invariant $\mathcal{Q}_X$ and are furthermore encoded in brightness ($\mathcal{Q}_{X,0}$) and hue ($\mathcal{Q}_{X,\pi}$). (a) Topological invariant $\mathcal{Q}_{\mathrm{BDI}}$ of the split-step quantum walk (2.37). (b) Topological invariant $\mathcal{Q}_{\mathrm{BDI}}$ of the four-step quantum walk (2.38), where $\theta_1 = \theta_3$ and $\chi_{1,2,3} = 0$, so that falls into class BDI. (c) Topological invariant $\mathcal{Q}_{\mathrm{DIII}}$ of the quantum walk (2.40), with $\theta_2 = 0$. For all three examples, the length of the scattering region is $L = 50$. Close to phase boundaries, where the gap closes, $r$ becomes subunitary due to finite size effects and the invariants are not quantized. Otherwise the quantization of the invariants is evident.

### 2.7.4 Disorder

A major advantage of the classification of topological phases using the scattering matrix is that the topological invariants can also be defined for systems with spatial disorder.

As a proof of concept, let us now add disorder to the simple quantum walk, Eq. (2.10). Spatial disorder is introduced by drawing the the rotation angle $\theta(x)$ for each site $x$ from a Gaussian ensemble with mean $\langle\theta\rangle$ and variance $\delta\theta$, with no correlation for different $x$. This breaks neither PHS nor CS, so a BDI topological invariant is still defined if $r$ remains unitary.

As for the split-step walk, the BDI topological invariant is just half the reflection block itself, which is a single number. Furthermore, due to an additional symmetry,[97] $\mathcal{Q}_{\mathrm{ch},\pi} = -\mathcal{Q}_{\mathrm{ch},0}$, so we only have to consider quasienergy $\epsilon = 0$. We thus numerically calculated an ensemble average of $r(0)$ for a range of $\langle\theta\rangle$ and $\delta\theta$ which is presented in Fig. 2.4. Note that the topological invariant is stable against the introduction of small disorder unless very close to the transition, demonstrating the stability of the phases to disorder.

For strong disorder, the ensemble average approaches zero (the green region in Fig. 2.4). However, this is not due to the fact that $r$ becomes subunitary. On the contrary, the distribution of $r$ is strongly bimodal around $\pm 1$, indicating that individual systems are still insulating and allow for the definition of a topological invariant, whose value however can not be predicted for large disorder strengths.

## 2.8 Experiment

The scattering matrix of a discrete-time quantum walk is not only a theoretical construct but can also be directly measured. In this section we discuss the principle of such an experiment using the example of the split-step walk, introduced in Sec. 2.7.1. For the split-step walk, the reflection matrices are real numbers of unit magnitude, $(r(0), r(\pi)) =$

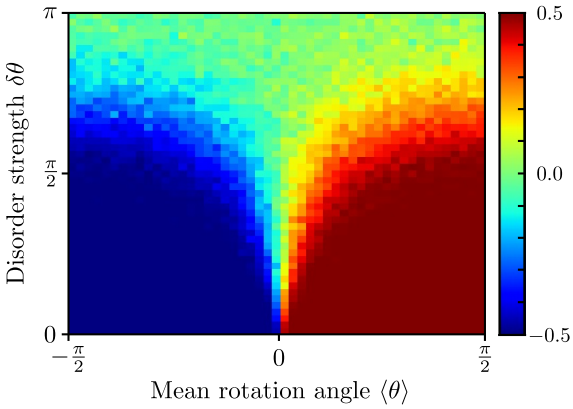


**Figure 2.4:** Disorder averaged invariant $\langle \mathcal{Q}_{\mathrm{ch},0} \rangle$ at $\varepsilon = 0$ for the simple quantum walk as a function of mean rotation angle and disorder strength. The transition region around $\langle \theta \rangle = 0$ is broadened with increasing disorder until the topological phases are not properly defined anymore (green region). System size is $L = 50$, the average is taken over $n = 100$ different disorder realizations.

$(\pm 1, \pm 1)$, and, using (2.19), the pair of topological invariants simplify to

$$\begin{aligned} \mathcal{Q}_{\mathrm{ch},0} &= \frac{1}{2} \sum_{\nu=1}^{\infty} \langle -1, \downarrow | \mathscr{F}^{\nu} | -1, \uparrow \rangle ; \\ \mathcal{Q}_{\mathrm{ch},\pi} &= \frac{1}{2} \sum_{\nu=1}^{\infty} (-1)^{\nu} \langle -1, \downarrow | \mathscr{F}^{\nu} | -1, \uparrow \rangle . \end{aligned} \tag{2.42}$$

These formulas suggest a measurement protocol for the topological invariants: (1) Initialize the walk with the walker at time $\tau = 0$ at $x = -1$, in state $\uparrow$. (2) Obtain the topological invariants as the sum, and alternating sum of the probability amplitudes for the walker at timestep $\tau \in \mathbb{N}$ to be at $x = -1$, in state $\downarrow$. This measurement can be straightforwardly conceived in optical realizations of quantum walks, as we show below.

We demonstrate our ideas using a simple beam splitter (BS) representation of the quantum walk, shown in Fig. 2.5. This layout can be easily adapted to many actual physical realizations, including integrated photonics,[152] or even optical feedback loops.[161*] It consists of an array of cascaded BS's, with a light pulse incident on the lower left BS. As

*Recently, there has in fact been a report of the realization of this experimental proposal in time-multiplexed quantum walk experiments using optical fiber loops, Ref. 18.

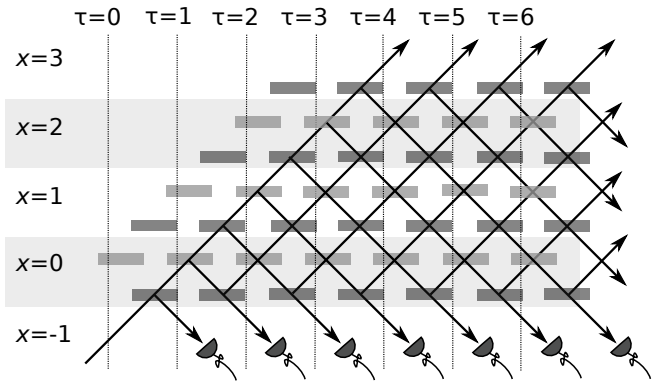


**Figure 2.5:** Schematic layout for the experimental measurement of the reflection amplitudes of a split-step quantum walk. An incident coherent light pulse at $\tau = 0$, $x = -1$ enters an array of beam splitters of two types (dark blue, light orange), where it is split and recombined repeatedly, thereby performing the quantum walk. A row of detectors at $x = -1$ measure the wave amplitudes $\langle -1, \downarrow | \mathscr{F}^{\tau} | -1, \uparrow \rangle$ leaving the quantum walk region. The reflection amplitudes $r(0)$ and $r(\pi)$ are given by the sum and and the alternating sum of the measured reflected amplitudes, Eqs. (2.42).

the light propagates in time, it spreads throughout the array in a way that can be interpreted as a quantum walk. The state of the light just before and just after the $n$th column of BS's is mapped to the state of the walker just before and just after the $n$th rotation operation. The direction of propagation of the modes is identified with the internal state of the walker, "right-up" representing $\uparrow$ and "right-down" representing $\downarrow$. The vertical coordinate in the arrays is identified with the position $x$ of the walker, as indicated in Fig. 2.5. We use two different types of BS's to realize the two rotations in the Floquet operator, Eq. (2.36).

In optical DTQW experiments, intensity measurements on the modes leaving the array at the right edge are used to read out the position distribution of the walker after $\tau$ steps. In our case, there are two differences. First, as indicated in Fig. 2.5, our output modes are not at the right edge, but rather at the bottom edge of the array. Second, intensity measurement on the output modes does not work for us, since it destroys the phase information that is crucial to obtain the topological invariants, as sums of probability amplitudes, Eq. (2.42).

A direct measurement of the probability amplitudes as required for the invariants is possible if the incident light pulse is a strong coherent state $|\alpha\rangle$, containing many photons. This is standard practice in some

photonic quantum walk experiments.[161] Strictly speaking the spreading of the light pulse is then not a quantum walk any more, since there is no entanglement at any point in the system. However, it simulates a single-photon quantum walk directly. At any time, the array contains coherent states $\Pi_j |\alpha_j\rangle$, with the coherent amplitudes $\alpha_j$ corresponding exactly to the probability amplitudes $\Psi_j$ of the walker, $\Psi_j = \alpha_j/\alpha$. This is used in experiments[160] to read out the state of the walker during the walk, and to measure the probability distribution after $N$ steps in one shot.

The 0 and $\pi$ quasienergy invariants are obtained by measuring the sum and the alternating sum of the outcoming coherent amplitudes, cf. Eqs. (2.42). This can be done practically by interfering each output mode with a local oscillator, or, interfering the output modes directly with each other on an N-port. Note that since the BS's have only real elements (no phase shifting), a single intensity measurement suffices. Moreover, in this setup, one can even use a CW laser instead of a laser pulse.

## 2.9 Conclusion

In this chapter we have classified the topological phases of one-dimensional discrete-time quantum walks using a scattering matrix approach. For this purpose, we generalized the concept of the scattering matrix to these periodically time-dependent systems.

We find that, dependent on their symmetries, gapped DTQWs are characterized by one of three different topological invariants, $\mathcal{Q}_{\mathrm{D}}$, $\mathcal{Q}_{\mathrm{DIII}}$ and $\mathcal{Q}_{\mathrm{ch}}$. They are calculated from the determinant, Pfaffian or trace of the reflection matrix as summarized in Table 2.1. In contrast to their analogs for time-independent systems,[66] the invariants consist of two independent contributions $\mathcal{Q} = \mathcal{Q}_0 \times \mathcal{Q}_\pi$ that are evaluated at the two special quasienergies $\varepsilon = 0, \pi$. Adapting arguments for topological insulators,[66] we found that an interface between two extended quantum walk regions hosts a number of protected boundary states that equals the difference of the invariants across the interface. These are stationary states of the walk where the walker stays exponentially close to the interface, and has quasienergy $\varepsilon = 0$ or $\varepsilon = \pi$.

We also considered unbalanced DTQWs where there is a difference $n$ in the number of left- and rightward shifts per cycle, producing a

quasienergy winding in the Brillouin zone. We found that they have $n$ channels that transmit perfectly in the majority direction. The characterization of transmission in this problem, including the transport time distribution of disordered quantum walks with quasienergy winding, poses an interesting direction for further investigation.

We provide a simple scheme to directly measure the reflection matrix — and, thus, the topological invariants — of a quantum walk. This scheme is well within the reach of current experiments working with light pulses [137,152,160,161].

Our scattering matrix approach complements existing methods based on Floquet operators in momentum space, with two important advantages. First, we provide a unified framework describing topological phases in different symmetry classes as simple functions of a single, typically small matrix. Second, our formulas use only a single time frame for the Floquet operator. This is in contrast with Ref. 14, which explicitly states that the topological invariants of chiral quantum walks can only be obtained by combining the winding numbers from different timeframes. The scattering matrix gets around this restriction, and probes the behavior of the system *during* a protocol by including contributions from plane wave-like modes that enter and exit the scattering region at intermediate times.

The scattering matrix formalism presented in this chapter gives a powerful new tool for the investigation of the effects of disorder on topological phases and transport in DTQWs. Depending on the types of disorder and symmetries, experiments and theory on DTQWs have already seen both Anderson localization, [159] and delocalization. [134] Our generalized scattering matrix formalism allows a continuation of this research to more general multistep DTQWs.

## 2.A Numerical implementation

According to Eq. (2.19) the scattering matrix is determined by following the time evolution of a particle which is placed in an incoming mode until it enters an outgoing mode. While doing so, most of the infinite Hilbert space of the scattering problem will not be reached by the particle. Consequently, we can evaluate this formula in a modified, finite Hilbert space.

We thus introduce a reduced circular system, which contains all states

of the $L$ sites in the system, and additional "buffer" states, which we now describe. Consider all lead states that are localized on a single lead site only and, after one period, will be shifted into the scattering region. These are the only lead states which are non-trivially involved during one time step, all other lead states are just shifted according to the lead propagator. Likewise, consider all localized lead states that are reached from the scattering region during one period. These two groups of states are arranged symmetrically with respect to the scattering center: Whenever a shift operator moves a state into the scattering region from one side, a corresponding state on the other side of the system is moved out of the system. To form the reduced finite space, we identify such pairs of lead states with each other. Each pair forms one of the buffer states, which in turn form a circular system when combined with the scattering region.

In summary, there are $d_n$ buffer states and $L$ system states in the reduced space for each internal state $n$. For exactly one time period, the time evolution of this finite system will be the same as for the original infinite system.

We can use this system to describe the complete scattering process, if before each step we initialize the buffer states with a wave function from the incoming leads, propagate for one unit of time, and then unload the buffer states as the outgoing mode. Denoting by $\psi_{\text{sys}}$ the wave function on the scattering sites and by $\psi_{\text{in/out}}$ the states of the buffer, the dynamics are described by:

$$\begin{pmatrix}\psi_{\text{sys}}(t+1)\\ \psi_{\text{out}}(t+1)\end{pmatrix} = V\begin{pmatrix}\psi_{\text{sys}}(t)\\ \psi_{\text{in}}(t)\end{pmatrix} = \begin{pmatrix}A & w_{\text{in}}\\ w_{\text{out}} & S_0\end{pmatrix}\begin{pmatrix}\psi_{\text{sys}}(t)\\ \psi_{\text{in}}(t)\end{pmatrix}, \tag{2.43}$$

where the matrix $V$ describes the effect of $\mathscr{F}$ on this reduced space. We note that this form corresponds to the standard form for discrete-time scattering problems given in Ref. 67.

We can write $V$ in terms of modified shift and rotation operators:

$$V = V_S^{(M)} V_R^{(M)} \cdots V_S^{(2)} V_R^{(2)} V_S^{(1)} V_R^{(1)}. \tag{2.44}$$

Here, the effect of $S^{(j)}$ on our reduced space is given by a shift matrix

$$V_S^{(j)} = \sum_n \sum_{x=-d_n}^{L} |x + s_{n_j}, n\rangle \langle x, n|, \tag{2.45}$$

which is circular because of the identification of incoming and outgoing localized states $|L+1,n\rangle \simeq |-d_n,n\rangle$. Similarly, the effect of a rotation on this space is given by

$$V_R = \sum_{n,n'} \sum_{x=1}^{L} |x,n\rangle R_{nn'}(x) \langle x,n'| + \sum_{n} \sum_{x=-d_n}^{0} |x,n\rangle \langle x,n|, \tag{2.46}$$

applying the rotation to the system, but not to the buffer.

It can then be shown[67] that the scattering matrix (reflection and transmission) can be obtained from the finite matrix $V$ by

$$S = w_{\text{out}} \left( e^{-i\varepsilon} - A \right)^{-1} w_{\text{in}} + S_0, \tag{2.47}$$

in contrast to Eq. (2.19) which is defined on an infinite space.

# 2.B Symmetries of the reflection matrix

## 2.B.1 Derivation of the symmetry relations

We demonstrate how we obtain the symmetry relations Eqs. (2.26), (2.27), (2.28) for the reflection matrix. Assume that we are given a scattering state with one incoming mode ($n \in M_+$), so that

$$(\varepsilon - H_{\text{eff}}) \left[ |l_{n,d,\varepsilon}\rangle + r\,|l_{n,d,\varepsilon}\rangle + |\Psi_C\rangle \right] = 0. \tag{2.48}$$

The first term is the incoming mode and the second term describes the corresponding reflected modes, where we use operator notation for the reflection matrix:

$$r\,|l_{n,d,\varepsilon}\rangle = \sum_{n' \in M_-} \sum_{d'=1}^{d_{n'}} r_{n'd',nd}\,|l_{n',d',\varepsilon}\rangle. \tag{2.49}$$

The third term describes the wavefunction within the scatterer, cf. Eq. (2.16).

By application of the TRS operator $\mathcal{T}$ on Eq. (2.48), using the fact that it commutes with $H_{\text{eff}}$, and employing the representation of TRS on the scattering states, Eq. (2.24), we find that

$$(\varepsilon - H_{\text{eff}}) \left[ Q_T\,|l_{n,d,\varepsilon}\rangle + V_T r^*\,|l_{n,d,\varepsilon}\rangle + \mathcal{T}\,|\Psi_C\rangle \right] = 0, \tag{2.50}$$

where the complex conjugation occurs due to the antiunitarity of $\mathscr{T}$.

Thus we constructed another scattering state at energy $\varepsilon$, where the incoming modes are the time-reversed former outgoing modes: $V_T r(\varepsilon)^* |l_{n,d,\varepsilon}\rangle$, and outgoing modes are constructed from the time-reversed incoming mode: $Q_T |l_{n,d,\varepsilon}\rangle$. By the definition of $r$, we thus must have the relation

$$r(\varepsilon) V_T r(\varepsilon)^* |l_{n,d,\varepsilon}\rangle = Q_T |l_{n,d,\varepsilon}\rangle , \tag{2.51}$$

and as this holds for all $n \in M_+$ and corresponding $d$, we can conclude Eq. (2.26). Analogous arguments can be given to show Eq. (2.27) and Eq. (2.28).

## 2.B.2 Basis transformations

We next consider basis transformations of the incoming and outgoing modes in order to turn the symmetries of $r$ presented in Eqs. (2.26) to (2.28) into standard form. Because the incoming and outgoing modes are separate spaces, we can choose basis transformations for both independently. This amounts to a multiplication of $r$ with two unrelated unitary matrices from the left and right respectively.

In the following we assume that $r$ is taken at energies $\varepsilon = 0, \pi$ and we suppress energy dependence.

*Class D* If $\mathscr{P}^2 = 1$, it can be seen that $Q_{P\pm} = Q_{P\pm}^T$. Thus, we can find square roots $M_\pm^2 = Q_{P,\pm}$, which are also symmetric. It can then be checked that after the transformation

$$\tilde{r} = M_-^* r M_+^T , \tag{2.52}$$

Eq. (2.28) is equivalent to $\tilde{r} = \tilde{r}^*$.

*Class DIII* If $\mathscr{T}^2 = -1$, one can see that $Q_T^T = -V_T$. Again, we can find symmetric square roots,

$$M_+^2 = Q_{P,+} , \tag{2.53}$$

$$M_-^2 = Q_T^\dagger Q_{P,-} Q_T^* , \tag{2.54}$$

and performing the basis transformation

$$\tilde{r} = M_-^* V_T^* r M_+^T , \tag{2.55}$$

this leads from Eqs. (2.26) and (2.28) to $\tilde{r} = \tilde{r}^* = -\tilde{r}^T$. Importantly, one uses the fact that because of assumed irreducibility of any unitary symmetry operator, by Schur's lemma we must have $\mathscr{P}\mathscr{T}\mathscr{P}\mathscr{T} = e^{i\phi}$, from which one finds that $M_- M_+^T = e^{-i\phi/2}$.

*Chiral classes* For these classes, we have a chiral operator, obeying $V_\Gamma Q_\Gamma = \Gamma^2 = 1$. Then we can choose $\tilde{r} = V_\Gamma r$ and from Eq. (2.27) find $\tilde{r} = \tilde{r}^\dagger$.

We note that these transformation are not unique (for instance, in class D, any orthogonal transformation preserves $\tilde{r} = \tilde{r}^*$) , so that other possible choices exist. The actual value of topological invariants obtained from $\tilde{r}$ depend on the choice. However, because there is no unambiguous notion of a trivial vacuum for quantum walk systems, we do not impose further restrictions on the choice of basis, and instead remark that the definition of topological invariants is only possible after fixing a specific suitable basis.

## 2.C Protected boundary states

Here we derive the existence of protected boundary states caused by a change of topology across an interface between two domains with a different DTQW protocol. We exemplify the derivation for a class D quantum walk. For other symmetry classes, one can argue in a similar fashion.[66]

If two compatible DTQWs, a left (A) and right (B) one, are interfaced, a bound state occurs at the interface whenever $\mathrm{Det}\,(1 - r_A r'_B) = 0$, where $r'$ denotes the reflection matrix for incoming states from the right. Consider a fixed energy $\varepsilon \in 0, \pi$. The reflection matrices $r_A$ and $r'_B$ are orthogonal matrices at this energy, as is their product. Thus, $\mathrm{Det}\,(r_A r'_B) = \pm 1$.

The determinant $\mathrm{Det}\,(r_A r'_B)$ is the product of the eigenvalues of an orthogonal matrix, which in term come either in complex conjugate pairs or are 1 or $-1$.

For even matrix size and $\mathrm{Det}\,(r_A r'_B) = -1$, an odd number of eigenvalues has to be $-1$ and thus at least one eigenvalue 1. An eigenvalue of 1 amounts to a bound state at the given energy. For odd matrix size on the other hand, a positive determinant requires at least one eigenvalue 1 and thereby ensures a bound state.

To connect these bound states to the topological invariant $\mathcal{Q}_{\mathrm{D}}$, we first need to understand the relation between $r$ and $r'$. This can be deduced by requiring that by connecting two copies of the same quantum walk, no bound states should exist (they would be states in the middle of a gap). Thus for even matrix dimension, $\mathrm{Det}\, r = \mathrm{Det}\, r'$ while for odd matrix dimension $\mathrm{Det}\, r = -\mathrm{Det}\, r'$.

In conclusion this means that, when $\mathrm{Det}\, r_A \neq \mathrm{Det}\, r_B$, a bound state between the two regions is ensured by the change of topology across the boundary.

# 3 Chiral symmetry and bulk-boundary correspondence in periodically driven one-dimensional systems

## 3.1 Introduction

Controlling the topological phases of matter is an important challenge in solid state physics. In the recent years, periodic driving has emerged as an important tool to meet this challenge. Topologically protected edge states, the hallmarks of topological phases, have been predicted and observed in periodically driven systems, such as materials irradiated by light[51,100,116,176], in shaken optical lattices,[76,146] and in photonic crystals.[145] In the above cases, the principle of bulk—boundary correspondence[150] was applied to the effective (Floquet) Hamiltonian of the periodically driven system.

The variety of topological phases that periodically driven systems can display, however, is much wider than those of their Floquet Hamiltonians, and the systematic exploration of these phases has only just begun.[149] An important example is the case of periodically driven one-dimensional topological superconductors,where, the bulk $\mathbb{Z}_2$ invariant is replaced by a pair of $\mathbb{Z}_2$ invariants, whose calculation necessitates information beyond that represented by the Floquet Hamiltonian.[84] The edge states then are the Floquet Majorana fermions, with potential applications in quantum information processing.[117] Such states, not predicted by the bulk Floquet Hamiltonian, have also been observed in optical realization of a one-dimensional quantum walk.[99]

Simulations of one-dimensional periodically driven superconductors

have shown that they can host a large number of Floquet Majorana fermions at their ends.[170,172] This can be explained by an extra chiral symmetry (CS) of the Floquet Hamiltonian, which prevents Majorana fermions on the same sublattice from recombining into complex fermions. Although this explanation is sufficient in some cases,[170,172] it cannot be general as it only relies on the Floquet Hamiltonian. Thus, the question is still open: what are the bulk topological invariants for periodically driven systems with CS?

In this chapter, we find the bulk—boundary correspondence for periodically driven one-dimensional quantum systems with chiral symmetry, building on the theory of CS in discrete-time quantum walks.[13,14,97,101] We show how CS can be ensured in a periodically driven system, whose time evolution in a period starts with a unitary operator $F$, by choosing an appropriate second part for the period. We show that the topological invariants predicting the number of 0 and $\pi$ quasienergy end states are the winding numbers of the blocks of $F$ in a canonical basis. Our formulas give a direct recipe to tune the topological invariants using a sublattice shift operation. We give an example of how to realize this operation in the simplest periodically driven one-dimensional Floquet insulator with CS, the periodically driven Su-Schrieffer-Heeger (PDSSH) model. We show how this model realizes a discrete-time quantum walk, and how this can be used to calculate the topological invariants of particle-hole symmetric quantum walks.

## 3.2 Floquet formalism

We consider periodically driven single-particle lattice Hamiltonians, $H(t+1) = H(t)$. The long-time dynamics of $H(t)$, i.e., over many periods, is governed by the time-evolution operator of one period, the Floquet operator $U(\tau)$,

$$U(\tau) = \mathbb{T} e^{-i\int_{\tau}^{\tau+1} H(t)dt}, \tag{3.1}$$

where $\mathbb{T}$ stands for time ordering. If at time $\tau$ the system is in an eigenstate $|\Psi\rangle$ of the Floquet operator, $U(\tau)|\Psi\rangle = e^{-i\varepsilon}|\Psi\rangle$, then at all times $\tau + n$, for $n \in \mathbb{Z}$, it will be in state $e^{-in\varepsilon}|\Psi\rangle$. In this sense, the periodically driven system acts as a stroboscopic simulator of the effective (Floquet)

Hamiltonian $H_{\text{eff}}$,

$$H_{\text{eff}}(\tau) = i \ln U(\tau). \tag{3.2}$$

We fix the branch of the logarithm by restricting the eigenvalues $\varepsilon$ of $H_{\text{eff}}$, the quasienergies, to $-\pi < \varepsilon \leq \pi$.

The Floquet operator $U(\tau)$, and thus also the effective Hamiltonian $H_{\text{eff}}(\tau)$, depend on the choice of the starting time of the period, $\tau$. Changing $\tau$ amounts to a unitary transformation of the Floquet operator and the effective Hamiltonian (quasienergies are independent of $\tau$).

### 3.2.1 Chiral symmetry of periodically driven systems.

Ensuring CS of the periodically driven system amounts to ensuring that there is an initial time $\tau$ such that the corresponding effective Hamiltonian has CS, i.e., there is a unitary, Hermitian, and local (within a unit cell) operator $\Gamma$, that satisfies

$$\Gamma H_{\text{eff}}(\tau)\Gamma = -H_{\text{eff}}(\tau) \quad \Longleftrightarrow \quad \Gamma U(\tau)\Gamma = U^{-1}(\tau). \tag{3.3}$$

The effective Hamiltonian does not inherit CS from the instantaneous Hamiltonian, as is the case with particle—hole symmetry.[98] However, CS of the periodically driven system is ensured if there is an intermediate time $0 < t_1 < 1$ that splits the period into a first and second part in a special way. Let $F$ denote the time evolution of the first part of the cycle,

$$F = \mathbb{T} e^{-i \int_{\tau'}^{\tau'+t_1} H(t) dt}. \tag{3.4}$$

The second part of the cycle has to fulfill

$$\Gamma F^\dagger \Gamma = \mathbb{T} e^{-i \int_{\tau'+t_1}^{\tau'+1} H(t) dt}. \tag{3.5}$$

It is easy to check that in that case, not only $U' \equiv U(\tau')$, but also $U'' \equiv U(\tau'')$ have CS, where $\tau'' = \tau' + t_1$. These Floquet operators read

$$U' = \Gamma F^\dagger \Gamma F; \qquad U'' = F \Gamma F^\dagger \Gamma. \tag{3.6}$$

### 3.2.2 Topological invariants due to chiral symmetry

Consider a one-dimensional Floquet insulator: a long chain, with a translation invariant insulating bulk part, whose quasienergy spectrum has gaps around $\varepsilon = 0$ and $\pi$. If the system has CS, a local basis transformation can be performed that diagonalizes $\Gamma$, so that each lattice site has a sublattice index A or B, defined via the projectors $\Pi_{A/B} = (1 \pm \Gamma)/2$. We call such a basis a *canonical basis*. For the system to be a Floquet insulator, the number of A and B sites in each bulk unit cell has to be equal (or else the system would have flat bands at 0 or $\pi$ quasienergy). We denote this number by $N$. In a canonical basis, the CS operator acts in each unit cell independently, as $\Gamma = \sigma_z \otimes 1_N$.

The spectrum of an effective Hamiltonian with CS is symmetric: stationary states $|\Psi'\rangle$ of $H'_{\text{eff}}$ with quasienergy $\varepsilon \neq 0, \pi$ have chiral symmetric partners $\Gamma|\Psi'\rangle$, that are also eigenstates with quasienergy $-\varepsilon$. Such states can be chosen to have equal support on both sublattices. The system can also host states $|\Psi'\rangle_{L/R}$ with quasienergy $\varepsilon = 0$ or $\pi$, whose wavefunctions are expelled from the bulk to the left/right by the gaps in the bulk spectrum. These *end states* can be chosen to have support only on one sublattice.

The effective Hamiltonians $H'_{\text{eff}}$ and $H''_{\text{eff}}$ have CS, as per Eqs. (3.6), and thus can be assigned topological invariants $\nu'$ and $\nu''$. These are obtained by standard procedure,[150] whereby we first isolate the bulk part of $H'_{\text{eff}}$ and $H''_{\text{eff}}$, by imposing periodic boundary conditions on the translation invariant central part of these Hamiltonians, and taking the thermodynamic limit. The bulk Hamiltonians are periodic functions of the quasimomentum $k \in [-\pi, \pi]$, and, in the canonical basis, are block off-diagonal,

$$H_{\text{eff}}(k) = \begin{pmatrix} 0 & h(k) \\ h^\dagger(k) & 0 \end{pmatrix}. \tag{3.7}$$

Here, and later on, $H_{\text{eff}}$ refers to either of $H'_{\text{eff}}$ or $H''_{\text{eff}}$, and similarly for $U$ and $h$. The topological invariants are

$$\nu' = \nu[h']; \qquad \nu'' = \nu[h''], \tag{3.8}$$

where the function $\nu[h]$ is a winding number,

$$\nu[h] = \frac{1}{2\pi i} \int_{-\pi}^{\pi} dk \frac{d}{dk} \ln \text{Det}\, h(k). \tag{3.9}$$

These integers cannot change under adiabatic deformation of the bulk Hamiltonians, and so are equal to the winding numbers of the flat band limits of these Hamiltonians, which are the topological invariants of Ryu et al.[150] They can be interpreted as the dimensionless bulk sublattice polarization[127] of the effective Hamiltonians, at times $\tau'$ and $\tau''$.

### 3.2.3 Topological invariants of the driven system

To derive the topological invariants of the periodically driven system, we start by adopting the results obtained for discrete-time quantum walks (DTQW) with CS[14] to periodically driven systems. The derivations follow very closely those of Ref. 14, and so we omit them here, but for completeness, we give details in Appendix 3.A. As with DTQWs, also in periodically driven systems, the wavefunctions of quasienergy $\pi$ end states switch sublattices as they evolve from time $\tau'$ to $\tau''$, and so, neither $\nu'$, nor $\nu''$, on their own, give useful information about the number of end states (observations to the contrary in specific models[170,172] do not generalize). The winding numbers $\nu'$ and $\nu''$ must be combined to obtain the bulk topological invariants controlling the number of end states,

$$\nu_0 = \frac{\nu' + \nu''}{2}; \qquad \nu_\pi = \frac{\nu' - \nu''}{2}. \tag{3.10}$$

We now proceed to simplify Eqs. (3.10), and express them using the blocks of $F$ in the canonical basis:

$$F(k) = \begin{pmatrix} a(k) & b(k) \\ c(k) & d(k) \end{pmatrix}. \tag{3.11}$$

Along the way, we will use simple properties of the function $\nu[A(k)]$ of Eq. (3.9): $\nu[AB] = \nu[A] + \nu[B]$ and $\nu[A^\dagger] = -\nu[A]$, for arbitrary $A(k)$ and $B(k)$.

There are two constraints on the winding numbers of the blocks of the Floquet operator $F$ representing the first part of the drive cycle, both following from the unitarity of $F$. First, substituting Eqs. (3.11) directly into $F(k)F(k)^\dagger = 1$ gives $ac^\dagger = -bd^\dagger$. Taking the winding numbers of the two sides gives

$$\nu[c] - \nu[a] = \nu[d] - \nu[b]. \tag{3.12}$$

Second, $F$ represents an operation on an open chain, terminated at its ends. Thus, the average displacement of a state in the bulk, with this

average going over all possible states, has to be zero: Otherwise, unitarity of $F$ would be violated in the end regions. This average displacement is given by the winding number of $F$ itself,[98] which, since $F$ is unitary, can be written as

$$\nu[F] = \frac{1}{2\pi i}\int dk \mathrm{Tr}\, F^\dagger(k)\frac{d}{dk}F(k). \tag{3.13}$$

Inserting the decomposition of $F$ in the canonical basis, Eq. (3.11), into $\nu[F] = 0$, gives

$$\nu[F] = \nu[a] + \nu[c] + \nu[b] + \nu[d] = 0. \tag{3.14}$$

To use the relations derived above, we note, that

$$U = e^{-iH_{\mathrm{eff}}} = \cos H_{\mathrm{eff}} - i \sin H_{\mathrm{eff}}. \tag{3.15}$$

Because of the block off-diagonal structure of $H_{\mathrm{eff}}$, the first term in the sum above corresponds to the block diagonal and the second to the block off-diagonal parts of $U$. Now since $\mathrm{sign}(\varepsilon) = \mathrm{sign}\,(\sin\varepsilon)$ for $\varepsilon \in [-\pi, \pi]$, the winding number of $H_{\mathrm{eff}}$ is the same as that of $\sin H_{\mathrm{eff}}$. Therefore, in Eq. (3.9) above, we can substitute the off-diagonal block of $U$ in a canonical basis: $h \to iU_{12}$. For the topological invariants of the effective Hamiltonians $H'_{\mathrm{eff}}$ and $H''_{\mathrm{eff}}$, using Eqs. (3.6), substituting the blocks of $F$, we obtain $\nu' = \nu[a^\dagger b - c^\dagger d]$ and $\nu'' = \nu[-ac^\dagger + bd^\dagger]$. We can simplify these using the unitarity of $F$, whereby $a^\dagger b + c^\dagger d = 0$ and $ac^\dagger + bd^\dagger = 0$, and the fact that $\nu[\alpha c] = \nu[c]$ for any $\alpha \in \mathbb{C}$. We obtain

$$\nu' = \nu[b] - \nu[a] = \nu[d] - \nu[c]; \tag{3.16a}$$

$$\nu'' = \nu[a] - \nu[c] = \nu[b] - \nu[d]. \tag{3.16b}$$

Inserting these equations into Eqs. (3.10), together with Eqs. (3.14) and (3.12), gives us

$$\nu_0 = \nu[b]; \qquad \nu_\pi = \nu[d]. \tag{3.17}$$

These equations are the central result of this chapter: In one-dimensional periodically driven systems with CS, the windings of the determinant of the off-diagonal and the diagonal blocks of the Floquet operator in a canonical basis fix the number of end states at quasienergy 0 and $\pi$, respectively.

Eqs. (3.17) determine the topological invariant $\nu_0$ ($\nu_\pi$) even if the gap of $H_{\text{eff}}$ at quasienergy $\varepsilon = \pi$ ($\varepsilon = 0$) is closed, a problem raised by Tong et al.[172] Consider

$$\cos H'_{\text{eff}} = 1 - 2\begin{pmatrix} c^\dagger c & 0 \\ 0 & b^\dagger b \end{pmatrix} = 2\begin{pmatrix} a^\dagger a & 0 \\ 0 & d^\dagger d \end{pmatrix} - 1. \tag{3.18}$$

If there is a quasimomentum $k$ where the gap of $H'_{\text{eff}}$ closes around $\varepsilon = 0$, then $\cos H'_{\text{eff}}(k)$ has a doubly degenerate eigenvalue $+1$. At that $k$, using the first relation of Eq. (3.18), either $c(k)$ or $b(k)$ (or both) have an eigenvalue zero. This means $\nu_0$ is not well defined, and neither are $\nu'$ or $\nu''$. However, $\nu_\pi$ of Eq. (3.17) is still well defined. Similarly, if at some $k$ the gap of $H'_{\text{eff}}$ around $\varepsilon = \pi$ closes, then, using the second relation of Eq. (3.18), $a(k)$ or $d(k)$ must have an eigenvalue zero, and $\nu_\pi$ is not well defined, but $\nu_0$ is.

### 3.2.4 Geometrical picture

In case of a two-band 1D Floquet insulator with CS, we can give a geometrical interpretation for the topological invariants $\nu_0$ and $\nu_\pi$. We relegate details to Appendix 3.B, and just summarize the results here.

Disregarding an irrelevant global phase, the evolution operator for the first half of the period reads $F(k) = e^{-i\vec{f}(k)\vec{\sigma}}$, with $\vec{f}(k)$ a three-dimensional real vector inside a unit sphere of radius $\pi$, all points on whose surface are identified with each other, and $\vec{\sigma}$ the vector of Pauli matrices. As $k$ traverses the Brillouin zone $[-\pi, \pi]$, $\vec{f}(k)$ describes a directed, smooth, closed loop. If the gap around $\varepsilon = 0$ is open, the loop of $\vec{f}(k)$ cannot touch the $z$-axis or the surface of the sphere, and we find that the invariant $\nu_0$ is given by the winding of the loop around the $z$ axis. If the gap of $H_{\text{eff}}$ around $\varepsilon = \pi$ is open, the path of $\vec{f}(k)$ cannot touch the circle in the $xy$ plane of radius $\pi/2$. In that case, $\nu_\pi$ is given by the winding of the loop around that circle.

### 3.2.5 Tuning the invariants

Formulas (3.17) allow for a simple way to tune the topological invariants of a periodically driven system, using a unitary sublattice shift operation $S(n)$, whose bulk part reads

$$S(n,k) = \exp(-in\Gamma k). \tag{3.19}$$

In the bulk, $S(n)$ displaces sites on sublattice $A$ ($B$) to the right (left) by $n$ sites. Therefore, at the left/right end, under the effect of $S(n)$, $n$ states must switch sublattices, transitioning $B \to A$ / $A \to B$ (if $n$ is negative, vice versa). How this transition happens depends on the details of $S(n)$ that have no influence on the topological invariants (nor on the number of end states).

To tune the invariants of a periodically driven system, obeying Eq. (3.6), with some $F = F^{(0)}$, insert extra sublattice shifts before and after $F^{(0)}$,

$$F^{(1)} = S(m)F^{(0)}S(n). \tag{3.20}$$

Substituting into Eqs. (3.17), we obtain directly the topological invariants of the modified driven system,

$$\nu_0^{(1)} = \nu_0^{(0)} + m - n; \qquad \nu_\pi^{(1)} = \nu_\pi^{(0)} - m - n. \tag{3.21}$$

## 3.3 Example: the periodically driven SSH model

We now illustrate the concepts introduced above on the PDSSH model, given by

$$H_{\mathrm{SSH}}(t) = \sum_{j=1}^{M} \left( v(t) c_{2j} c_{2j-1}^\dagger + w(t) c_{2j+1} c_{2j}^\dagger \right) + \mathrm{h.c.}, \tag{3.22}$$

where $c_x$ annihilates the fermion on site $x$. For simplicity, we keep the intracell hopping amplitudes $v(t)$ and the intercell hopping amplitudes $w(t)$ real, homogeneous in space, and modulated periodically, with period 1. We fix open boundary conditions by identifying $c_{2M+1} = 0$ (as opposed to periodic boundary conditions, which would require $c_{2M+1} = c_1$).

The sublattice shift operator $S(n)$ can be realized[149] by the following drive sequence: a pulse of $v$ of area $\pi/2$, followed by a pulse of $w$ of area $-\pi/2$. This allows us to realize a discrete time quantum walk as a periodically driven lattice Hamiltonian.

As a concrete example, we consider the PDSSH model on an open chain of 40 sites ($M = 20$ unit cells). The drive sequence, shown in Fig. 3.1 (a), consists of a train of nine pulses, chosen to be Gaussian for numerical convenience, applied to $v$ and $w$ homogeneously. We ensure

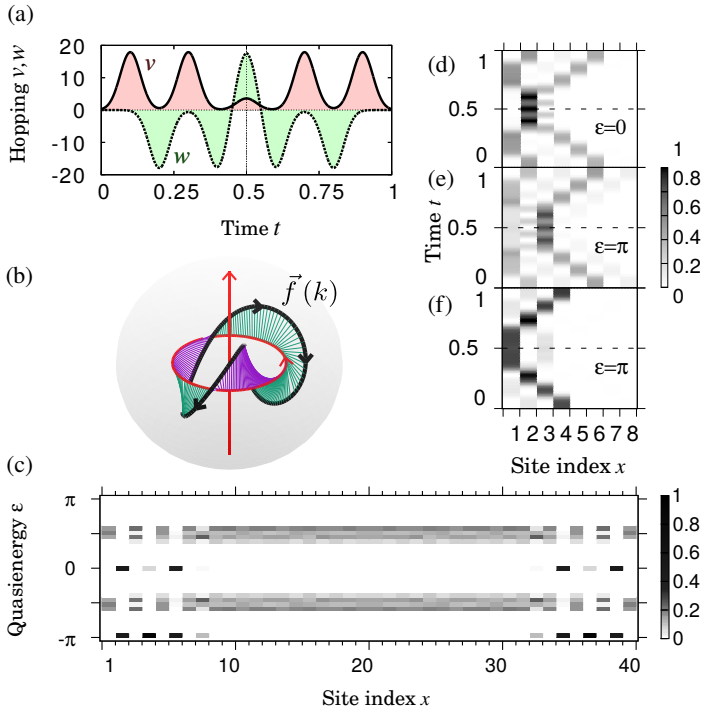


**Figure 3.1:** Floquet eigenstates of a periodically driven SSH chain of 40 sites. (a) Time dependence of the intracell (continuous) and intercell (dotted) hopping amplitudes. (b) The curve $\vec{f}(k)$, which winds -1 times around the z axis (red) and -2 times around the circle of radius $\pi/2$ on the $xy$ plane, showing that $\nu_0 = -1$ and $\nu_\pi = -2$. (c) Local Density of States of the effective Hamiltonian $H_{\text{eff}}(0)$. (d) Time evolution of the position distribution $|\langle\Psi(t)|x\rangle|^2$ of the single end state with $\varepsilon = 0$, and (e,f) of two orthogonal end states with $\varepsilon = \pi$.

CS by way of Eq. (3.6), with $t_1 = 0.5$, by choosing both $v(t)$ and $w(t)$ to be even functions of time.

We follow the recipe of Eq. (3.20), to realize $\nu_0 = -1, \nu_\pi = -2$. The role of role of $F^{(0)}$ is played by the first half of the central Gaussian pulse, where $w = 5v$: thus, it is a short pulse $e^{-i\pi/2H_1}$, where $H_1$ is an SSH Hamiltonian in the topologically nontrivial phase. So, we have $\nu_0^{(0)} = 1$, $\nu_\pi^{(0)} = 0$. To test the robustness of the recipe, we realize the sublattice displacement $S(n = 2)$ only approximately by allowing considerable overlaps between the $\pi/2$ area pulses of $v$ and the $-\pi/2$ area pulses of $w$.

We find that the bulk topological invariants and the end states agree

perfectly with the theory above. The invariants are the winding numbers of the curve of Fig. 3.1 (b), which are $\nu_0 = -1, \nu_\pi = -2$. Correspondingly, in the local density of states, Fig. 3.1 (c), at each end, we find two end states at $\varepsilon = \pi$, and 1 end state at $\varepsilon = 0$, exclusively localized on B/A sublattice at the left/right end. The time dependence of these end states, Fig. 3.1 (d-f), shows that that they indeed spread over both sublattices at intermediate times, but return to a single sublattice at $t = 0.5$. For the $0/\pi$ energy end states, this is the same/opposite sublattice as that occupied at $t = 0$.

Since we restricted the hopping amplitudes $v$ and $w$ to be real, the instantaneous SSH Hamiltonian, Eq. (3.22), has particle-hole symmetry (PHS), represented by $\Gamma K$, where $K$ denotes complex conjugation.The PDSSH model inherits this symmetry, and therefore, its the end states are analogous to 0 and $\pi$ quasienergy Floquet Majorana fermions. If CS is violated, but PHS is maintained, only the parity of the number of the Floquet Majorana fermions at each edge and at each quasienergy $0,\pi$ is protected. There is a corresponding pair of bulk $\mathbb{Z}_2$ topological invariants.[84] In the case of the PDSSH model, we can follow the construction of Jiang et al.[84] and find that the $\mathbb{Z}_2$ invariants can simply be obtained from the complete areas of the pulses of $v$ and $w$. For details, see Appendix 3.C.

## 3.4 Outlook

The topologically protected states our theory predicts should have experimental signatures in different kinds of setups. Optical experiments, where edge states are routinely imaged directly,[99,103] are in the best position to test our predictions. Alternatively, in transport measurements, the end states should give rise to transmission resonances, similar to the ones predicted for Floquet Majorana fermions.[105]

Our work leaves a couple of theoretical questions open. First, is the decomposition of the drive cycle $U$ into $F$ and $\Gamma F^\dagger \Gamma$, as per Eqs. (3.4-3.6), a necessary requirement for a periodically driven Hamiltonian to have CS? For previously studied cases[170,172] we can find such a decomposition, but if a counterexample were to be found, the theory we presented here would need to be expanded. Second, the bulk effective Hamiltonian $H_{\text{eff}}(\tau, k)$ of a one-dimensional Floquet insulator (with or without CS) is periodic in both $\tau$ and $k$, and thus has a Chern number. In all the

examples we examined numerically, we found this Chern number to be zero, but can it take on a nonzero value? If so, what is the physical interpretation of this number? Last, how can the topological invariants we found here be formulated in the frequency domain [149]? This is especially an interesting question, as previous work on the PDSSH model using this approach [70] has not detected the pair of topological invariants we found.

# 3.A Derivation of Eqs. (3.10)

To derive Eqs. (3.10), we follow closely the line of thought of Ref. 14. We consider an open, periodically driven chain with CS, which has one bulk and two ends. Let $n'_{A/B,0/\pi}$ denote the number of end states at the left end on the $A/B$ sublattice at quasienergy $0/\pi$ of the Hamiltonian $H'_{\text{eff}}$, and $n''_{A/B,0/\pi}$ the corresponding quantities for $H''_{\text{eff}}$. The bulk-boundary correspondence for the effective Hamiltonians $H'_{\text{eff}}$ and $H''_{\text{eff}}$ reads

$$\nu' = n'_{A,0} - n'_{B,0} + n'_{A,\pi} - n'_{B,\pi}; \tag{3.23a}$$

$$\nu'' = n''_{A,0} - n''_{B,0} + n''_{A,\pi} - n''_{B,\pi}. \tag{3.23b}$$

Topologically protected end states of periodically driven one-dimensional lattices with CS can be divided to two classes: (a), they have quasienergy 0 and are on the same sublattice at $\tau'$ and $\tau''$, or (b) have quasienergy $\pi$ and are on opposite sublattices. Indeed, consider a topologically protected end state $|\Psi'\rangle$, which is an eigenstate of $U'$ with eigenvalue $e^{-i\varepsilon}$, with $\varepsilon \in \{0,\pi\}$. It is only on a single sublattice: $\Gamma|\Psi'\rangle = e^{-i\gamma}|\Psi'\rangle$, with $\gamma = 0/\pi$ corresponding to sublattice $A/B$. Now consider the same end state at the other special time $\tau''$, $|\Psi''\rangle = F|\Psi'\rangle$. This is an eigenstate of $U''$ with the same quasienergy $\varepsilon$. This state is also on one sublattice only, because $\Gamma F|\Psi'\rangle = \Gamma F \Gamma e^{i\gamma}|\Psi'\rangle = \Gamma F \Gamma e^{i(\gamma-\varepsilon)} \Gamma F^{-1} \Gamma F \Psi' = e^{i(\gamma-\varepsilon)} F|\Psi'\rangle$. So $|\Psi''\rangle$ is on the same (opposite) sublattice as $|\Psi'\rangle$ if $\varepsilon = 0$ ($\varepsilon = \pi$). This can be written succinctly as

$$n''_{A,\pi} - n'_{B,\pi} = n''_{B,\pi} - n'_{A,\pi} = 0; \tag{3.24a}$$

$$n''_{A,0} - n'_{A,0} = n''_{B,0} - n'_{B,0} = 0. \tag{3.24b}$$

Using Eqs. (3.24) to simplify $\nu' + \nu''$ and $\nu' - \nu''$ from Eqs. (3.23), we obtain

$$\nu_0 = \frac{\nu' + \nu''}{2}; \qquad \nu_\pi = \frac{\nu' - \nu''}{2}, \tag{3.25}$$

which are Eqs. (3.10) we set out to demonstrate.

## 3.B Geometrical picture

For a two-band 1D Floquet insulator with CS, we can give a direct geometrical picture for the topological invariants $\nu_0$ and $\nu_\pi$. Since the global phase cannot wind ($F$ cannot have quasienergy winding), it can safely be disregarded, and the evolution operator for the first half of the period then reads $F(k) = e^{-i\vec{f}(k)\vec{\sigma}}$. Here $\vec{f}$ is a 3-dimensional vector, of magnitude $f \in [0,\pi]$ and $\vec{\sigma}$ the vector of Pauli matrices. The $k$-dependent vector $\vec{f}(k)$ is restricted inside a spherical ball of radius $\pi$, with all points on the surface identified with each other. The $a,b,c,d$ in Eq. (3.11) are just complex number valued functions of $k$,

$$F = \begin{pmatrix} \cos f - i \sin f \cos\theta & -i \sin f \sin\theta e^{-i\phi} \\ -i \sin f \sin\theta e^{i\phi} & \cos f + i \sin f \cos\theta \end{pmatrix}, \tag{3.26}$$

using spherical coordinates. As $k$ traverses the Brillouin zone, $\vec{f}(k)$ describes a directed, smooth, closed loop, that can at some $k$ exit the ball at a point on the surface and reenter at the same $k$ at the antipodal point.

If the gap around $\varepsilon = 0$ is open, the loop of $\vec{f}(k)$ cannot touch the $z$-axis, nor the surface of the sphere. Thus, the loop has a well defined winding number around the $z$ axis,

$$\nu_0 = \frac{1}{2\pi} \int dk \frac{d}{dk} \phi(k). \tag{3.27}$$

Since both $f(k), \theta(k) \in [0,\pi]$ for all $k$, this is the same as the winding number $\nu_0$ obtained by substituting (3.26) into Eq. (3.17).

The gap of $H_{\text{eff}}$ around $\varepsilon = \pi$ closes when $\vec{f}(k)$ is on the circle on the $n_z = 0$ plane of radius $\pi/2$ ($n_z = 0$ and $f = \pi/2$). Thus, if the gap around $\varepsilon = \pi$ is open, the loop of $\vec{f}(k)$ has a well defined winding number around that circle. To calculate this winding number, first discard the $\phi$ information, by setting $\phi = 0$. This transforms the 3D closed path of $\vec{f}(k)$ into a

2D path in a semicircle, with the points on the circular boundary with the same $x$ coordinate identified. We need the winding of this path around the single point, $f = \pi/2, n_z = 0$. This is found by deforming the semicircle yet again, by the transformation $(f\sin\theta, f\cos\theta) \to (\cos f, \sin f\cos\theta)$, into circle, into whose origin the point $f = \pi/2, n_z = 0$ is mapped. The winding number is then

$$\nu_\pi = \frac{1}{2\pi}\int dk \frac{d}{dk}\arctan\frac{\cos f(k)}{\sin f(k)\cos\theta(k)} \tag{3.28}$$

which is the same as $\nu_\pi$ obtained by substituting Eq. (3.26) into Eq. (3.17b).

## 3.C The $\mathbb{Z}_2 \times \mathbb{Z}_2$ invariant

The PDSSH model, Eq. (3.22), has particle-hole symmetry (PHS), represented by $\Gamma K$, where $K$ stands for complex conjugation. This antiunitary symmetry is inherited by the effective Hamiltonian from the instantaneous Hamiltonian.[98]

If we break CS in the PDSSH model, an end state can remain protected if it can have no PHS partner. This happens whenever the number of end states at a given energy and at a given end is odd: then, after breaking CS, a single end state is still protected by PHS. We illustrate this on the PDSSH model. If we break CS by delaying the intracell hopping amplitude $v$ by $\delta t$ with respect to the intercell hopping $w$ pulses, as shown in Fig. 3.2 (a), the lone end state at $\varepsilon = 0$ is still topologically protected, while the pair of end states at $\varepsilon = \pi$ hybridize and move away from the edge of the energy Brillouin zone (except for a time shift of 0.5, where the conditions for CS are again fulfilled). To break PHS, we can add a sublattice potential to the SSH model, obtaining the periodically driven Rice-Mele (PDRM) model,

$$H_{\mathrm{RM}}(t) = H_{\mathrm{SSH}}(t) + u(t)\sum_{x=1}^{M}\left(c^\dagger_{2x-1}c_{2x-1} - c^\dagger_{2x}c_{2x}\right). \tag{3.29}$$

Now, CS still holds if in addition to $v(t)$ and $w(t)$ being even functions of time, $u(t)$ is odd: $u(t) = -u(-t)$. We choose $u(t) = \sin(2\pi t)$. This time, if we break CS by shifting the $v(t)$ pulse in time with respect to the $w(t)$ and $u(t)$ pulses, as shown in Fig. 3.2 (b), all end states move away from their original energies (again except for the time shift of 0.5).

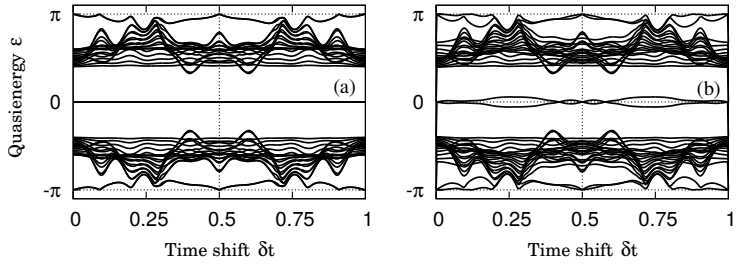


**Figure 3.2:** Effect of breaking CS by time-shifting the pulse of the intracell hopping $v(t)$ with respect to the other pulses. (a) In the PDSSH model, the extra PHS protects the end states at $\varepsilon = 0$. (b) In the PDRM model, there is no PHS, and all end state energies are affected by the time shift.

The extra PHS of the PDSSH model brings with it an extra pair of bulk topological invariants, $(Q_0, Q_\pi) \in \mathbb{Z}_2 \times \mathbb{Z}_2$, which predict the number of end states protected by PHS at 0 and $\pi$ energy. If we have CS, the invariants are just $Q_\varepsilon = \nu_\varepsilon \bmod 2$; if CS is broken, however, they can only be obtained by a procedure involving analytic continuation based on the full cycle $H(t)$, as found by Jiang et al.[84]

We find that for the PDSSH model, the invariant of Jiang et al.[84] can be given by simple closed formulas. At the momenta $k = 0$ and $k = \pi$, the Hamiltonians at different times all commute with each other, and therefore, all that matters is the total area under the $v$ and $w$ pulses,

$$V = \int_0^1 v(t)dt; \qquad W = \int_0^1 w(t)dt. \tag{3.30}$$

A short calculation gives

$$Q_0 = \operatorname{sgn}\left(\sin\frac{V+W}{2}\sin\frac{V-W}{2}\right); \tag{3.31}$$

$$Q_0 Q_\pi = \operatorname{sgn}\big(\sin(V+W)\sin(V-W)\big). \tag{3.32}$$

## 3.D Mapping to the discrete time quantum walk

The PDSSH model, besides being the simplest periodically driven topological insulator, also gives a lattice realization of the discrete time split-step quantum walk. For the quantum walk, we need to define the

basis states $|R/L,x\rangle$, for coin state predicting the next step right/left, and the walker at position $x$. These basis states are identified with states on the SSH chain as

$$c^\dagger_{2x+1}|0\rangle = |R,x\rangle\,; \tag{3.33}$$

$$c^\dagger_{2x}|0\rangle = -i\,|L,x\rangle\,. \tag{3.34}$$

The basic operations of the split-step walk are rotations of the internal state of the walker, $R(\theta) = e^{-i\theta\sigma_y}$, and shifts of the $R/L$ internal state to the right/left, given by $S_\pm = e^{-ik(\sigma_z\pm 1)}$. One timestep of the split-step walk is defined as

$$U = S_- e^{-i\theta_2\sigma_y} S_+ e^{-i\theta_1\sigma_y}. \tag{3.35}$$

A pulse of $v$ of area $V$ followed by a pulse of $w$ of area $W$, in the basis of Eq. 3.34, can be written as

$$U = e^{-iW(\cos k\sigma_y - \sin k\sigma_x)} e^{-iV\sigma_y}, \tag{3.36}$$

which reproduces the timestep of the split-step walk with the angles

$$\theta_2 = W + \pi/2; \qquad\qquad \theta_1 = V - \pi/2. \tag{3.37}$$

The above mapping is important as it allows us to apply results about the topological phases of periodically driven systems to quantum walks.

As an example, consider the invariants due to CS, via Eqs. (3.17), for the simple quantum walk, given by $U = S_- S_+ e^{-i\theta\sigma_y}$. According to the mapping above, the winding numbers are $\nu_0 = \nu[-i(s + ce^{ik})]$, $\nu_\pi = \nu[c - se^{-ik}]$, with $c = \cos(\pi/4+\theta/2)$, $s = \sin(\pi/4+\theta/2)$. We get $(\nu_0,\nu_\pi) = (+1,0)$ if $|c| > |s|$, i.e., if $\theta \in [-\pi,0]$, and $(0,-1)$ if $\theta \in [0,\pi]$. This is shifted by $(1/2,-1/2)$ from the invariants obtained by the scattering matrix method,[169] but such a shift is not physical: both methods predict a pair of end states at 0 and $\pi$ quasienergy at an interface between bulks with $\theta < 0$ and $\theta > 0$, as seen in simulations.[13]

Another example is the calculation of the invariants due to PHS in the split-step quantum walk. Compared to the invariants $Q_0^{(\mathrm{gap})}, Q_\pi^{(\mathrm{gap})}$, defined via gap closings in the parameter space,[13] the above mapping to the PDSSH model, together with Eqs. (3.32) gives $Q_0 = Q_0^{(\mathrm{gap})}$, and $Q_\pi = 1 - Q_\pi^{(\mathrm{gap})}$, which agrees in all the predictions concerning end states at interfaces. Compared to the scattering matrix topological invariants,[169] we of course find the same constant shift by $(1/2,-1/2)$ as for the invariants due to CS, which has no influence on the physical predictions.

# 4 Attractor-repeller pair of topological zero-modes in a nonlinear quantum walk

## 4.1 Introduction

A classical random walk is invariably associated with diffusive motion, but quantum superposition and interference allow for a more varied dynamics. A quantum walk can explore phase space more rapidly than its classical counterpart,[2,59,124] a shift from diffusive to ballistic dynamics that is at the origin of the quadratic speed-up of quantum search algorithms.[91,175] Diffusion is recovered for temporal disorder, while spatial disorder can induce an Anderson quantum phase transition to localized wave functions.[3,4,54,69,85,134,158]

Two recent developments have further enriched the phenomenology: One development is the discovery that quantum walks can exhibit a topological phase transition, at which a bound state (a so-called zero-mode) appears at a boundary or domain wall.[15,35,88,99,101,141,148,184,186] A second development involves the introduction of nonlinearities in the dynamics.[107,110] These have been associated with soliton structures[48,130] and investigated as a means to speed up the quantum search.[126] Here we wish to connect these two separate developments, and explore how nonlinearities manifest themselves in a topological quantum walk.

We consider the simplest case of a one-dimensional discrete-time quantum walk in the chiral orthogonal symmetry class (also known as class BDI, familiar from the Su-Schrieffer-Heeger model[166]). The topological phase transition manifests itself by the appearance of a pair of zero-modes of opposite chirality. We demonstrate that these zero-modes may survive in the presence of nonlinearities and moreover acquire a special role as the attractor and repeller of the nonlinear dynamics.

## 4.2 Formulation of the linear quantum walk

We study the one-dimensional dynamics of a two-level system, represented by a spin-$\frac{1}{2}$ degree of freedom on the lattice $x \in \mathbb{Z}$. We employ a stroboscopic description, so that time $t \in \mathbb{Z}$ is discretized as well as space. The linear dynamics is obtained by repeated applications of a unitary operator $U$ on a spinor $\psi$,

$$\psi_t = (U)^t \psi_0, \;\; \psi_t(x) = (u(x,t), v(x,t)). \tag{4.1}$$

Quite generally, a single time step of such a discrete-time quantum walk can be decomposed into two operations: A rotation $R_\vartheta$ of the spinor and a shift $S$ to the left or to the right dependent on the spin component:

$$\begin{aligned} R_\vartheta \psi &= e^{-i\vartheta\sigma_y}\psi = (u\cos\vartheta - v\sin\vartheta, u\sin\vartheta + v\cos\vartheta), \\ S(u(x,t), v(x,t)) &= (u(x-1,t), v(x+1,t)). \end{aligned} \tag{4.2}$$

We can combine the two operations as $SR_\vartheta$ or $R_\vartheta S$, but we prefer to take the symmetrized product,[14]

$$U = R_{\vartheta/2} S R_{\vartheta/2}. \tag{4.3}$$

The evolution operator (4.3) is representative of a chiral orthogonal quantum walk, meaning that $U = U^*$ is real orthogonal (particle-hole symmetry) and$(\sigma_x U)^2 = 1$ (chiral symmetry). This BDI symmetry class supports a topologically protected zero-mode bound to a domain wall where $\vartheta(x)$ changes sign. Its time-independent state $\Psi_\pm(x)$ satisfies*

$$U\Psi_\pm = \Psi_\pm, \;\; \sigma_x \Psi_\pm = \pm\Psi_\pm. \tag{4.4}$$

The eigenvalue $\pm 1$ of the Pauli matrix $\sigma_x$ distinguishes the chirality of the zero-mode.†

*In addition to the zero-mode with $U\Psi = \Psi$, the domain wall may also support a bound state with $U\Psi = -\Psi$. Because this state is rapidly oscillating on the scale of the lattice constant, it plays no role in the long-wave length dynamics considered here.

†The fact that the zero-mode is an eigenstate of $\sigma_x$ follows from $U\Psi = \Psi$ and $U\sigma_x\Psi = \sigma_x(\sigma_x U)^2 U^{-1}\Psi = \sigma_x\Psi$. Since the zero-mode is nondegenerate, the two states $\Psi$ and $\sigma_x\Psi$ must be linearly related.

## 4.3 Introduction of a nonlinearity

We now introduce a nonlinearity (strength $\kappa$) into the quantum walk by inserting a $\psi$-dependent rotation at each time step,

$$\psi_{t+1}(x) = U\bar{\psi}_t(x), \tag{4.5a}$$
$$\bar{\psi}_t(x) = \exp\left(-i\kappa M_z(x,t)\sigma_y\right)\psi_t(x), \tag{4.5b}$$
$$M_z(x,t) = \psi_t^\dagger(x)\sigma_z\psi_t(x) = |u(x,t)|^2 - |v(x,t)|^2. \tag{4.5c}$$

This nonlinear time-evolution conserves particle-hole symmetry (a real $\psi$ remains real), but chiral symmetry no longer applies. Still, a zero-mode $\Psi_\pm$ of the linear problem ($\kappa = 0$) remains a stationary state when we switch on the nonlinearity, because $M_z = 0$ for any eigenstate of $\sigma_x$.

To appreciate the new features introduced by the nonlinearity, it is helpful to look at a uniform $\vartheta$ and a real initial state $\psi = (\cos\alpha, \sin\alpha)$ without any spatial dependence. In one time step the angle $\alpha$ is mapped to $\alpha + \vartheta + \kappa\cos 2\alpha$. This map is invertible if $|\kappa| \le 1/2$, but it is not area preserving. The phase space contracts around one of two attractive fixed points, defined by $\cos 2\alpha_c = -\vartheta/\kappa$, $\sin 2\alpha_c > 0$. Note that this relaxation does not involve any loss of particles: $\sum_x(|u|^2 + |v|^2)$ is conserved by the nonlinear dynamics.

As we will now show, for a spatially dependent $\vartheta(x)$ the zero-mode at a domain wall becomes an attractive or repulsive fixed point, depending on its chirality. We first present numerical evidence and then give the analytical solution in the continuum limit.

## 4.4 Collapse onto a zero-mode

We take a lattice of length $L$ with periodic boundary conditions, $-L/2 < x < L/2$. The profile of $\vartheta(x)$ consists of two domains, with domain walls of width $\lambda \ll L$ at $x_\pm = \pm L/4$:

$$\vartheta(x) = \begin{cases} \vartheta_0 \tanh(x/\lambda - L/4\lambda) & \text{for } 0 < x < L/2, \\ -\vartheta_0 \tanh(x/\lambda + L/4\lambda) & \text{for } -L/2 < x < 0, \end{cases} \tag{4.6}$$

see Fig. 4.1. As initial condition for the numerics we take a real Gaussian wave packet centered at $x = 0$,

$$\psi_0 = (u_0, u_0),\ u_0(x) = (2\sigma\sqrt{\pi})^{-1/2}\exp(-x^2/2\sigma^2), \tag{4.7}$$

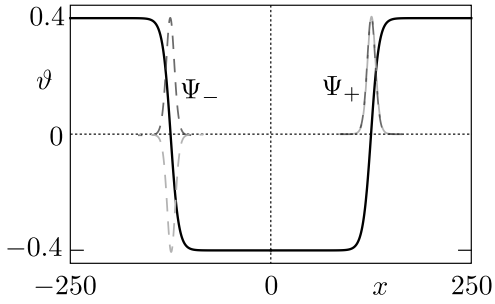


**Figure 4.1:** Solid curve: Position-dependent rotation angle $\vartheta(x)$ with a pair of domain walls at which the angle changes sign. Plotted is the profile (4.6) with $L = 500$, $\lambda = 10$, $\vartheta_0 = 0.4$ used in the numerical simulations. Dashed curves: The two (unnormalized) spinor components of the zero-modes bound to the two domain walls, calculated from Eq. (4.9). The state $\Psi_\pm$ is an eigenvector of $\sigma_x$ with eigenvalue $\pm 1$.

normalized to unity, $\int \psi_0^\dagger \psi_0 \, dx = 1$. Fig. 4.2 shows how this state collapses onto one of the two domain walls, depending on the sign of $\kappa$.

For the analytics we take the continuum limit of the discrete-time quantum walk, obtained from Eq. (4.5) under the assumption that the change $\delta\psi$ in one time step $\delta t$ is infinitesimal. The state-dependent rotation contributes a term $-i\delta t(\vartheta + \kappa\psi^\dagger\sigma_z\psi)\sigma_y\psi$ to $\delta\psi$, while the state-dependent shift contributes $-\delta t\sigma_z\partial\psi/\partial x$, resulting in the Dirac equation[124]

$$i\frac{\partial\psi}{\partial t} = -i\sigma_z\frac{\partial\psi}{\partial x} + \big(\vartheta(x) + \kappa\psi^\dagger\sigma_z\psi\big)\sigma_y\psi. \tag{4.8}$$

For large $L$ the two domain walls may be considered separately. The zero-mode bound to the domain wall at $x_\pm = \pm L/4$ is given by

$$\Psi_\pm \propto (u_\pm, \pm u_\pm), \;\; u_\pm(x) = \exp\left(\pm\int_x^0 \vartheta(x')dx'\right). \tag{4.9}$$

The time-independent state $\Psi_\pm$ is an eigenvector of $\sigma_x$ with eigenvalue $\pm 1$, selected by the sign of $\vartheta'(x)$ at the domain wall.

We now perform a linear stability analysis for a real perturbation $\psi(x,t) = \Psi_\pm(x) + \eta(x,t)$ of the zero-mode. To linear order in $\eta$ we have

$$\frac{\partial\eta}{\partial t} = -\sigma_z\frac{\partial\eta}{\partial x} - \vartheta(x)i\sigma_y\eta - 2\kappa u_\pm^2(x)(\pm\eta - \sigma_x\eta). \tag{4.10}$$

We focus on perturbations $\eta = e^{ikx}\eta(t)$ of the zero-mode with wave number $k \gtrsim 1/\lambda$, so we may neglect the spatial dependence of $\vartheta(x)$ and $u_\pm(x)$.

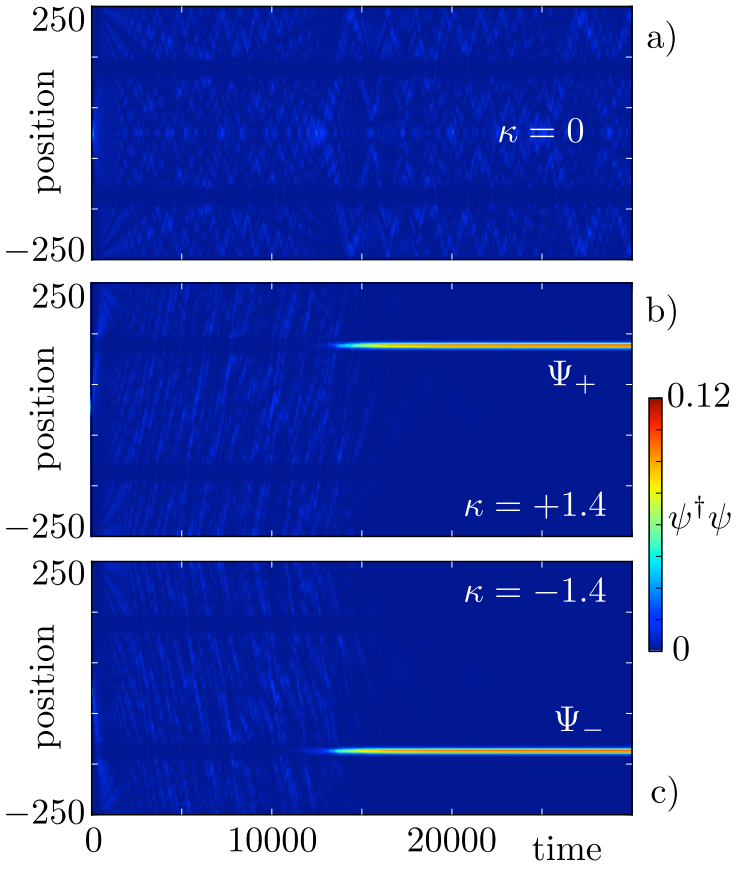


**Figure 4.2:** Time-evolution of the density $\psi_t^\dagger \psi_t$, starting from a real Gaussian wave packet $\psi_0 = (u_0, u_0)$ (given by Eq. (4.7) with $\sigma^2 = 50$), for the quantum walk with rotation angle profile of Fig. 4.1. The three panels show the result for the linear quantum walk (panel a, $\kappa = 0$) and for the nonlinear quantum walk (panels b and c, $\kappa = \pm 1.4$). Depending on the sign of the nonlinearity, the state collapses onto the zero-mode $\Psi_+$ or $\Psi_-$.

The resulting ordinary differential equation,

$$\frac{d\eta}{dt} = -\Gamma\eta,\ \Gamma = ik\sigma_z + i\vartheta\sigma_y + 2\kappa u_\pm^2(\pm 1 - \sigma_x), \tag{4.11}$$

has relaxation matrix $\Gamma$ with eigenvalues $\mu_1, \mu_2$ given by

$$\begin{aligned} &\mu_1 = \pm 2\kappa u_\pm^2 + \Delta,\ \mu_2 = \pm 2\kappa u_\pm^2 - \Delta, \\ &\Delta^2 = 4\kappa^2 u_\pm^4 - k^2 - \vartheta^2. \end{aligned} \tag{4.12}$$

We conclude that for $\kappa > 0$ the zero-mode $\Psi_+$ is an attractor ($\mathrm{Re}\,\mu_1, \mu_2 > 0$) and $\Psi_-$ is a repeller ($\mathrm{Re}\,\mu_1, \mu_2 < 0$), while for $\kappa < 0$ the roles are interchanged.

## 4.5 Initial states without particle-hole symmetry

Particle-hole symmetry ensures that a real $\psi$ remains real, but we might start with an initially complex state and ask for the stability of the zero-mode under complex perturbations. Substitution into Eq. (4.8) of $\psi = \Psi_\pm + \eta + i\zeta$, with real $\Psi_\pm, \eta, \zeta$, shows that to first order in $\eta, \zeta$ the nonlinear term contains only the real perturbation:

$$\begin{aligned} \frac{\partial}{\partial t}(\eta + i\zeta) = &-\sigma_z \frac{\partial}{\partial x}(\eta + i\zeta) - \vartheta(x) i\sigma_y(\eta + i\zeta) \\ &- 2\kappa u_\pm^2(x)(\pm\eta - \sigma_x\eta). \end{aligned} \tag{4.13}$$

The relaxation matrix for the real perturbation is as in Eq. (4.11), with eigenvalues $\mu_1, \mu_2$ given by Eq. (4.12). But the relaxation matrix for the imaginary perturbation,

$$\frac{d\zeta}{dt} = -\Gamma_0\zeta,\ \Gamma_0 = ik\sigma_z + i\vartheta\sigma_y, \tag{4.14}$$

has purely imaginary eigenvalues,

$$\mu_3 = i\sqrt{k^2 + \vartheta^2},\ \mu_4 = -i\sqrt{k^2 + \vartheta^2}. \tag{4.15}$$

More generally, a perturbation of a complex zero-mode

$$\Psi_\pm(x) = e^{i\phi}(u_\pm, u_\pm) \tag{4.16}$$

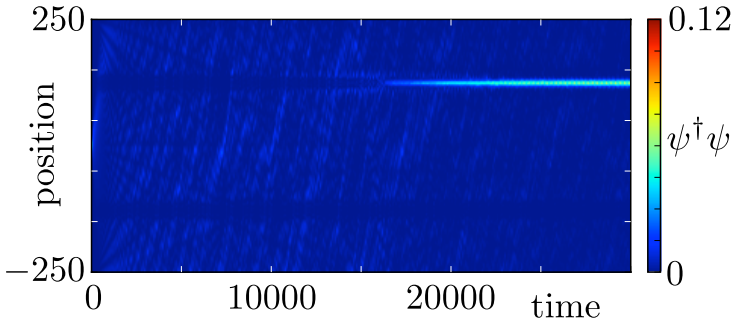


**Figure 4.3:** Same as Fig. 4.2b, but with a complex initial state $\psi_0 = (u_0, iu_0)$.

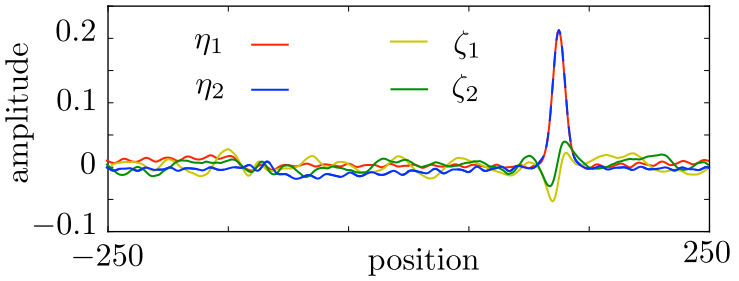


**Figure 4.4:** Decomposition of the state $\psi = e^{i\phi}(\eta + i\zeta)$ at a late time ($t = 8 \cdot 10^4$), starting from the complex state $\psi_0 = (u_0, u_0 + iu_0)$, with $u_0$ the Gaussian wave packet (4.7) ($\kappa = 1.4$, other parameters as in Fig. 4.1). The spinor $\eta = (\eta_1, \eta_2)$ is in-phase with the zero-mode $\Psi_+$, the spinor $\zeta = (\zeta_1, \zeta_2)$ is out-of-phase.

has (for $\kappa > 0$) a decaying in-phase component $e^{i\phi}\eta$ and a nondecaying out-of-phase component $ie^{i\phi}\zeta$ [with real spinors $\eta = (\eta_1, \eta_2), \zeta = (\zeta_1, \zeta_2)$]. Figs. 4.3 and 4.4 illustrate the resulting localized peak on the extended background.

## 4.6 Discussion

Fig. 4.2 summarizes our key finding: While the linear quantum walk is only slightly perturbed by the emergence of zero-modes at a topological phase transition, once we turn on the nonlinearity the wave packet is steered towards a domain wall and trapped in a zero-mode of definite chirality. This striking dynamics follows from a specific model calculation.

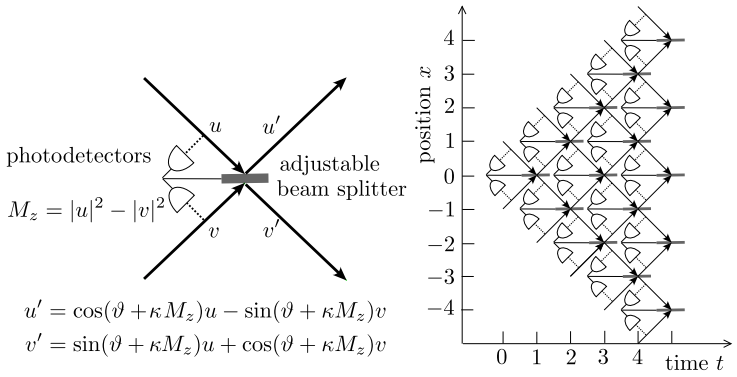


**Figure 4.5:** Optical Galton board consisting of an array of beam splitters with an adjustable transmission, conditioned on the output of a pair of photodetectors. The left panel shows a single element of the array, the right panel shows their combination.

How generic is it, and how might it be realized in an experiment?

For the experimental connection, we recall that quantum walks can be realized with true quantum mechanical elements [123] (ion traps, cold atoms, quantum dots) — or they can be simulated with classical waves, as in the optical Galton board [32,50,82,102,160]. Such a simulated quantum walk combines linear optical elements to mimic the quantum evolution of a spin-1/2 degree of freedom. Nonlinearities can be introduced via nonlinear optics, [164] or while staying within linear optics by introducing a feed-forward element conditioned on the output of a photodetector. [163] A scheme of the latter type* is illustrated in Fig. 4.5. This optical Galton board simulates a quantum walk with evolution operator $SR_\vartheta \exp(-i\kappa M_z \sigma_y)$, which differs from Eqs. (4.3) and (4.5) by the order of the operators ($SR_\vartheta$ instead of $R_{\vartheta/2}SR_{\vartheta/2}$). In the continuum limit of Eq. (4.8) this order is irrelevant, and we have checked numerically that the dynamics is essentially the same as in Fig. 4.2.

Concerning the generality of the result, we have two necessary conditions for the nonlinearity: it should preserve the zero-mode as a fixed point of the dynamics and it should contract phase space, breaking

*In the implementation of an optical Galton board shown in Fig. 4.5, the photon polarization plays no role and the spin-1/2 degree of freedom of the quantum walk is fully orbital. [15] The adjustable beam splitter combines the rotation and shift operators $R_\vartheta$ and $S$ in a single step. Alternative split-step implementations can use adjustable polarizers for $R_\vartheta$, followed by polarizing beam splitters [50] or birefringent displacers [99] for $S$.

the area-preservation of the linear dynamics. Both conditions hold if Eq. (4.5) is replaced by

$$\psi_{t+1} = U\bar{\psi}_t,\ \bar{\psi}_t = \exp(-i\tilde{\kappa}\tilde{M}\hat{n}\cdot\hat{\sigma})\psi_t, \qquad (4.17)$$
$$\tilde{M} = \psi_t^\dagger(\hat{m}\cdot\hat{\sigma})\psi_t,$$

with $\hat{\sigma} = (\sigma_x, \sigma_y, \sigma_z)$ and two unit vectors $\hat{n} = (0, n_y, n_z)$ and $\hat{m} = (0, m_y, m_z)$, satisfying $\hat{m}\times\hat{n} \neq 0$ (otherwise the map would be area preserving). Particle-hole symmetry is broken for $n_z \neq 0$, but the zero-mode $\Psi_\pm$ is preserved. A complex perturbation $\delta\psi$ has relaxation matrix $d\delta\psi = -\tilde{\Gamma}\delta\psi$ with eigenvalues $\tilde{\mu}_n$, $n = 1,2,3,4$, given by Eqs. (4.12) and (4.15), upon the replacement $\kappa \mapsto \tilde{\kappa}(\hat{n}\times\hat{m})\cdot\hat{x}$. The attractor-repeller pair is preserved, demonstrating the generality of our findings.

We finally note that discrete-time quantum walks have been used as a design principle for quantum algorithms. For instance, the search algorithms of Refs. 11,162 can be understood in terms of bound states in effectively one-dimensional quantum walks. The key observations in this chapter, namely the convergence towards certain bound states from arbitrary initial states, as well as the accelerated escape from unwanted bound states, thus may have promising implications for quantum algorithms. This is in line with several other recent results on continuous time quantum walks, where nonlinearities are observed to speed up quantum algorithms.[126]

# 5 Quench dynamics of fermion-parity switches in a Josephson junction

## 5.1 Introduction

Superconductors connected by a Josephson junction can freely exchange pairs of electrons, but single-electron transfer is suppressed by the superconducting gap.[171] The tunneling of an unpaired electron into the junction is an incoherent, stochastic source of charge noise in a Cooper pair transistor.[41] In contrast to this undesirable "quasiparticle poisoning", a controlled phase-coherent way to exchange single quasiparticles with a superconductor would be a desirable tool, that would complement existing single-electron sources in normal metals and semiconductors.[30,31,52,64,121,136]

Here we propose to exploit the phenomenon of a *fermion-parity switch* to transfer, phase coherently and on demand, a single quasiparticle of adjustable charge $Q$ from a Josephson junction to a metal probe (see Fig. 5.1a). A fermion-parity switch is a topological phase transition (zero-dimensional class D in the "ten-fold way" classification[9,150]) where the superconducting condensate can lower its ground-state energy by incorporating an unpaired electron and changing the number of electrons in the ground state from $\nu_{\mathrm{F}}$ even to $\nu_{\mathrm{F}}$ odd,[17] leaving behind as "defects" an odd number of quasiparticle excitations above the ground state.

In the quasiparticle excitation spectrum, the switch in the ground-state fermion parity is signaled by the crossing of a pair of bound states (Andreev levels) at $E = 0$ (the Fermi level). There may be an even number of switches when the phase difference $\phi$ across the Josephson junction is incremented by $2\pi$ — if there is an odd number of switches (as in Fig. 5.1b) the superconductor is topologically nontrivial. The two lowest Andreev levels $\pm E_0(\phi)$ of a nontrivial Josephson junction have a

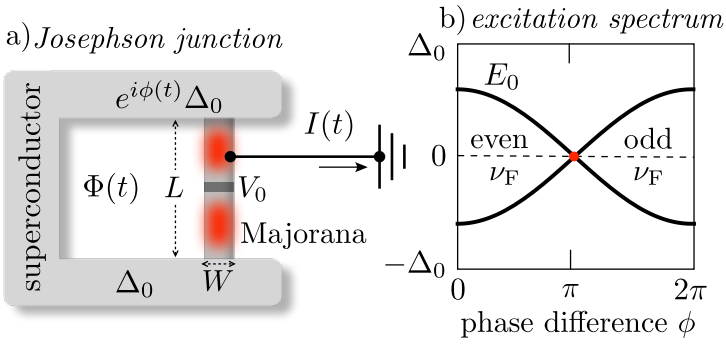


**Figure 5.1:** (a) Josephson junction formed by a superconducting ring interrupted by a nanowire. The junction contains two Majorana zero-modes, separated by a tunnel barrier (height $V_0$). A time-dependent flux $\Phi(t)$ through the ring drives the phase $\phi(t) = \Phi(t) \times 2e/\hbar$ through a fermion-parity switch, at which a quasiparticle is injected as a current $I(t)$ into the grounded metal probe. (b) Pair of phase-dependent Andreev levels $\pm E_0(\phi)$ in the closed Josephson junction (uncoupled from the metal). The switch in the ground-state fermion parity $\nu_F$ is signaled by a level crossing.

$\cos(\phi/2)$ phase dependence,[96]

$$E_0(\phi) = \Delta_0 \sqrt{T_0} \cos(\phi/2). \tag{5.1}$$

The superconducting gap is $\Delta_0$ and $T_0 \in (0,1)$ is the transmission probability through the junction. For small $T_0$ this describes a pair of bound states at nearly zero energy, consisting of an equal-weight superposition of electron and hole excitations. Such a charge-neutral quasiparticle is called a "Majorana fermion" (or Majorana zero-mode) because of the identity of particle and antiparticle. These objects have unusual non-Abelian statistics (see Refs. 24,45,113,177 for recent reviews), but here it is only their charge-neutrality that matters.

Fermion-parity switches are actively studied, theoretically and experimentally,* for the connection to topological superconductivity and Majorana fermions.[8,23,75,143] The *dynamics* of the transition is what concerns us here, in particular the quench dynamics, where $\phi(t)$ is driven rapidly through the switch from even to odd ground-state fermion parity.

The geometry of Fig. 5.1 that we consider is modeled after existing experiments (*e.g.*, Ref. 38), where a mesoscopic Josephson junction is formed by a semiconductor nanowire connecting two arms of a superconducting ring. A time-dependent flux $\Phi(t)$ enclosed by the ring

*For recent theoretical work, see Refs. 21,42,92,153,173,183. For expiremental work, see Refs. 38,111,112

imposes a time dependence on the phase difference $\phi(t) = \Phi(t) \times 2e/\hbar$ across the junction. When the Josephson junction is quenched through a fermion-parity switch there will appear a current pulse $I(t)$ from the superconductor (S) into the metal (N). We seek the quasiparticle content of that pulse. How many quasiparticles are transferred? What is the transferred charge? In particular, we wish to establish the conditions under which a single quasiparticle is transferred with vanishing charge expectation value.

We find that the quench dynamics transfers *one single* quasiparticle from the superconductor to the metal, as a wave packet that is a coherent superposition of electron and hole states near the Fermi level. A nearly charge-neutral equal-weight superposition is produced in a topologically nontrivial superconductor, if the metal probe couples predominantly to one of the two spatially separated Majorana zero-modes. More generally, for two arbitrary coupling constants $\gamma_1, \gamma_2$ we derive that the quantum quench injects a charge

$$Q_{\text{quench}} = 2e\sqrt{\gamma_1\gamma_2}/(\gamma_1 + \gamma_2) \tag{5.2}$$

into a single-channel point contact. For a multi-channel point contact the injected charge is reduced further by a factor $\mathscr{R}$ determined by the peak height $G_{\text{peak}} = (4e^2/h)(1 - \mathscr{R}^2)$ of the point contact conductance at resonance.

## 5.2 Microscopic model

Before proceeding to the mathematical analysis of the quench dynamics, we explore the relevant physical parameters in a microscopic model[165] for an InSb nanowire (length $L = 2.5\,\mu$m, width $W = 0.25\,\mu$m, Fermi energy $E_{\text{F}} = 1.52\,$meV, corresponding to 4 occupied electron subbands), coupled at both ends to a Nb superconductor (induced gap $\Delta_0 = 0.4\,$meV). Spin-rotation symmetry is broken by Rashba spin-orbit coupling (characteristic length $l_{\text{so}} = \hbar^2/m_{\text{eff}}\alpha_{\text{so}} = 0.25\,\mu$m), and time-reversal symmetry is broken by a magnetic field parallel to the wire (Zeeman energy $V_{\text{Z}} = \frac{1}{2}g_{\text{eff}}\mu_{\text{B}}B = 0.6\,$meV). For these parameters, the Josephson junction is in the nontrivial regime, with a pair of Majorana zero-modes at the two ends.[120,135] We tune the coupling strength of the Majoranas by means of a tunnel barrier of width 25 nm and adjustable height $V_0$ (which might be experimentally realized by means of a gate voltage).

The data shown in Fig. 5.2 is for $V_0 = 15\,\mathrm{meV}$. (See App. 5.A for details of the calculation.)

The Josephson junction is coupled by a point contact to a normal-metal probe, which plays the role of a fermion bath that can exchange quasiparticles with the superconductor. We assume that the charging energy of the junction is much smaller than the Josephson energy, to ensure that the Coulomb blockade of charge transfer is not effective. The Josephson junction is now an open system, with quasibound Andreev states $E_n - i\Gamma_n$ that acquire a finite life time $\hbar/2\Gamma_n$. The evolution of a pair of these states through the fermion-parity switch is shown in Fig. 5.2.[71] The coupling constants $\gamma_n$ that determine the transferred charge can be read off from

$$\pi\gamma_n = \lim_{\phi\to\pi} \Gamma_n(\phi). \tag{5.3}$$

Particle-hole symmetry requires that the complex energies come in pairs $\pm E - i\Gamma$, symmetrically arranged around the imaginary axis. This constraint produces a bifurcation point (pole transition[138] or exceptional point[151]) at which the real part is pinned to $E = 0$ and the decay rates $\Gamma_1$, $\Gamma_2$ become distinct — resulting in widely different $\gamma_1$, $\gamma_2$. The unusual extension of the level crossing over a finite interval seen in Fig. 5.2 is the key distinguishing feature of level crossings in superconducting and non-superconducting systems, and makes the dynamical problem considered here qualitatively different from the familiar Landau-Zener dynamics.[108]

## 5.3 Scattering formulation

The exchange of quasiparticles across the NS interface is described by the scattering matrix

$$S(t,t') = \delta(t-t') - 2\pi i W^\dagger G(t,t') W. \tag{5.4}$$

The coupling matrix $W$ to the fermion bath is assumed to be time-independent. The retarded Green's function $G(t,t')$ satisfies the differential equation[174]

$$\big(i\partial/\partial t - H[\phi(t)] + i\pi W W^\dagger\big) G(t,t') = \delta(t-t'), \tag{5.5}$$

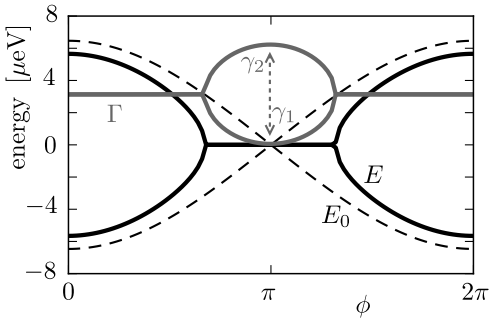


**Figure 5.2:** Phase dependence of the complex energies $E_n - i\Gamma_n$ of a pair of quasibound states of the open Josephson junction (solid curves), when the energies $\pm E_0$ of the closed junction (dashed curves) vary through the level crossing of Fig. 5.1b. At the fermion parity switch, the inverse lifetimes $\Gamma_n$ reach opposite extremal points $\pi\gamma_n$, $n = 1,2$.

where $H(\phi)$ is the Bogoliubov-De Gennes Hamiltonian of the Josephson junction at a fixed value $\phi$ of the superconducting phase difference. (We have set $\hbar \equiv 1$ for ease of notation.) Fourier transform to the energy domain is defined by

$$S(E,E') = \int_{-\infty}^{\infty} dt \int_{-\infty}^{\infty} dt'\, e^{iEt - iE't'} S(t,t'). \tag{5.6}$$

In a stationary situation, with a time-independent Hamiltonian $H$, the scattering matrix is diagonal in energy, $S(E,E') = 2\pi\delta(E-E')S_0(E)$, with $S_0$ given by the Mahaux-Weidenmüller formula,[122]

$$\begin{aligned} S_0(E) &= 1 - 2\pi i W^\dagger (E - H_{\rm eff})^{-1} W, \\ H_{\rm eff} &= H - i\pi W W^\dagger. \end{aligned} \tag{5.7}$$

The formulation of this dynamical problem in an open system in terms of an effective non-Hermitian Hamiltonian $H_{\rm eff}$ goes back to the early days of nuclear scattering theory.[63,118]

For a minimal description, we take a pair of Andreev levels in the Josephson junction coupled to a pair of electron-hole modes in a single-channel metal probe. (The multi-channel case is addressed in Sec. 5.5.) Both $H$ and $W$ are now $2\times 2$ matrices. Particle-hole symmetry requires that

$$H = -\sigma_x H^* \sigma_x, \;\; W = \sigma_x W^* \sigma_x. \tag{5.8}$$

(The Pauli matrix $\sigma_x$ interchanges electron and hole indices.) Particle-hole symmetry is the only symmetry constraint we impose on the system (symmetry class D), assuming that time-reversal symmetry and spin-rotation symmetry are both broken by magnetic field and spin-orbit coupling in the nanowire.

Using also that $H = H^\dagger$, we have the general form

$$H = E_0\sigma_z,\ W = e^{i\alpha'\sigma_z}\Lambda e^{i\alpha\sigma_z},\ \Lambda = \begin{pmatrix}\lambda_+ & \lambda_- \\ \lambda_- & \lambda_+\end{pmatrix}, \tag{5.9}$$

with real coefficients $\alpha, \alpha'$, $\lambda_\pm$. The eigenvalues $\gamma_1, \gamma_2 \geq 0$ of the coupling matrix product $WW^\dagger$ are given by

$$\gamma_1 = (\lambda_+ + \lambda_-)^2,\ \gamma_2 = (\lambda_+ - \lambda_-)^2. \tag{5.10}$$

The eigenvalues of $H_{\rm eff}$ (representing the poles of $S_0$ in the complex energy plane) are given by

$$E_\pm = -i\pi\bar{\gamma} \pm E_0\sqrt{1 + (\pi\tilde{\gamma}/E_0)^2 - (\pi\bar{\gamma}/E_0)^2}, \tag{5.11}$$

in terms of the arithmetic and geometric mean

$$\bar{\gamma} = \tfrac{1}{2}(\gamma_1 + \gamma_2),\ \tilde{\gamma} = \sqrt{\gamma_1\gamma_2}. \tag{5.12}$$

The evolution of $E_\pm$ through the fermion-parity switch is shown in Fig. 5.3. The relation $E_+ = -E_-^*$ required by particle-hole symmetry produces a bifurcation point at which the two quasibound states acquire distinct decay rates,[138,151] see also Fig. 5.2.

The time dependent phase difference $\phi(t)$ across the Josephson junction shakes up the fermion bath in the normal metal. We assume zero temperature, so that the unperturbed Fermi sea is the vacuum state $|0\rangle$ for excitations: $a(E)|0\rangle = 0$ for $E > 0$, with $a = (a_1, a_2)$ the two-component Nambu spinor of annihilation operators for Bogoliubov quasiparticles. The fermion-parity switch produces a superposition

$$|\Psi\rangle = \zeta_0|0\rangle + \textstyle\sum_{p=1}^\infty |\Psi_p\rangle \tag{5.13}$$

of the vacuum state with $p$-particle excited states

$$|\Psi_p\rangle = \left[\sum_{E>0}\sum_{E'<0} a^\dagger(E)S(E,E')a(E')\right]^p |0\rangle. \tag{5.14}$$

(The sum $\sum_E$ is evaluated as $(2\pi)^{-1}\int dE$.) The weight $\zeta_0$ of the unperturbed Fermi sea follows from the normalization $\langle\Psi|\Psi\rangle = 1$.

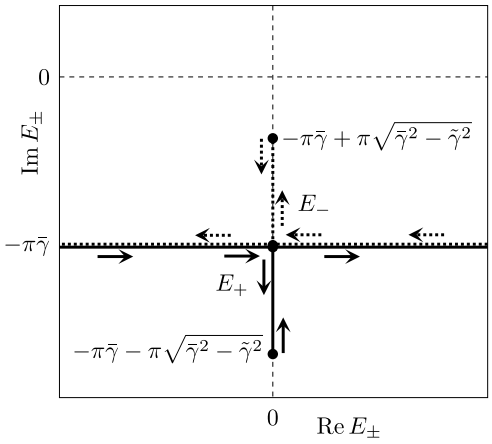


**Figure 5.3:** Evolution of the complex eigenvalues $E_\pm$ of the effective Hamiltonian (5.7) of the open Josephson junction (coupled to a metal probe), when the real eigenvalues $\pm E_0$ of the closed junction vary through a level crossing. At the fermion parity switch, $E_0 = 0$ and $E_\pm$ reach opposite extremal points on the imaginary axis.

## 5.4 Linear sweep through the fermion-parity switch

We now proceed to a complete solution of the dynamics of the fermion-parity switch, to derive the result (5.2) for the charge of the transferred quasiparticle. The non-superconducting counterpart to this problem was studied by Keeling, Shytov, and Levitov.[90] Their analysis provided much guidance and inspiration for what follows.

We calculate the scattering matrix for a linear sweep through the fermion parity switch: $E_0[\phi(t)] = \gamma_0^2 t$. Referring to Eq. (5.1), this linear approximation of the spectrum is justified for rapidities $\gamma_0^2 \ll \sqrt{T_0}\Delta_0\bar\gamma$. In the energy domain, Eqs. (5.4) and (5.5) then take the form

$$\begin{aligned} &S(E,E') = 2\pi\delta(E-E') - 2\pi i e^{-i\alpha\sigma_z}\Lambda G(E,E')\Lambda e^{i\alpha\sigma_z}, \\ &\big(i\gamma_0^2\sigma_z\partial/\partial E + E + i\pi\Lambda^2\big)G(E,E') = 2\pi\delta(E-E'). \end{aligned} \tag{5.15}$$

The solution for the Green's function factorizes,

$$G(E,E') = \frac{2\pi}{i\gamma_0^2} X(E)\Theta(E-E')\sigma_z X^{-1}(E')\sigma_z, \tag{5.16}$$

$$\Theta(E-E') = \begin{pmatrix} \theta(E-E') & 0 \\ 0 & \theta(E'-E) \end{pmatrix}. \tag{5.17}$$

Here $\theta(E)$ is the unit step function and the matrix $X(E)$ solves the homogeneous equation*

$$\left(i\gamma_0^2\sigma_z\partial/\partial E + E + i\pi\Lambda^2\right)X(E) = 0. \tag{5.18}$$

Because of particle-hole symmetry, $X$ has two rather than four independent elements,

$$X(E) = \begin{pmatrix} u(E) & v^*(-E) \\ v(E) & u^*(-E) \end{pmatrix}, \tag{5.19}$$

determined by

$$\gamma_0^2 u'' + (\varepsilon^2 + \delta^2 - i)u = 0,\ \ \delta v = i\varepsilon u - \gamma_0 u', \tag{5.20}$$

$$\varepsilon = (E + i\pi\bar{\gamma})/\gamma_0,\ \ \delta = \tfrac{1}{2}\pi(\gamma_1 - \gamma_2)/\gamma_0. \tag{5.21}$$

The retarded Green's function is specified by $G \to 0$ in the limits $E \to +\infty$ or $E \to -\infty$. The factor $\Theta$ in Eq. (5.16) ensures that this two-sided decay follows from the one-sided decay $u, v \to 0$ for $E \to +\infty$. With this condition the solution of Eq. (5.20) reads†

$$\begin{aligned} u(E) &= e^{i\varepsilon^2/2} U(-\tfrac{1}{4}i\delta^2, \tfrac{1}{2}; -i\varepsilon^2), \\ v(E) &= -\tfrac{1}{2}\delta e^{i\pi/4} e^{i\varepsilon^2/2} U(\tfrac{1}{2} - \tfrac{1}{4}i\delta^2, \tfrac{1}{2}; -i\varepsilon^2), \end{aligned} \tag{5.22}$$

where $U$ is the confluent hypergeometric function of the second kind.[1,109] The determinant of $X$ is particularly simple (see App. 5.B)

$$\mathrm{Det}\, X = \exp(-\pi\delta^2/4), \tag{5.23}$$

independent of energy.

*Since $X$ solves a homogeneous equation, the solution is only determined up to a multiplicative constant. This has no effect on the Green's function, because both $X$ and $X^{-1}$ appear in Eq. (5.16).

†To obtain $v$ from $u$ we used the identity $(d/dz)U(a,b;z) = -az^{-b}U(1+a-b,1-b;z)$.

The scattering matrix (5.15) results as the dyadic product of two vectors,

$$S_{nm}(E,E')|_{E>E'} = -\psi_n(E)\psi_m^*(-E'), \tag{5.24}$$

$$\psi(E) = (2\pi/\gamma_0)e^{\pi\delta^2/8}e^{-i\alpha\sigma_z}\Lambda\begin{pmatrix}u(E)\\ v(E)\end{pmatrix}. \tag{5.25}$$

Substitution into Eq. (5.14) gives $|\Psi_p\rangle = 0$ for $p \geq 2$ because of the anticommutation of the creation operators, so that only a single-particle excitation remains,*

$$|\Psi_1\rangle = -\sum_{E>0}\sum_{E'<0}[\psi(E)a^\dagger(E)][\psi^*(-E')a(E')]|0\rangle. \tag{5.26}$$

This absence of multi-particle excitations is a generic feature of rank-one scattering matrices.[89,90]

The normalization $\sum_{E>0}|\psi(E)|^2 = 1$ can be derived directly from Eq. (5.18). (See App. 5.B.) This implies that $\langle\Psi_1|\Psi_1\rangle = 1$, hence there is no contribution from the vacuum state [$\zeta_0 = 0$ in Eq. (5.13)]. Corrections of order $|e^{i\epsilon^2}| = \exp(-2\pi E\bar{\gamma}/\gamma_0^2)$ to the normalization appear because of the finite band width $E \lesssim \sqrt{T_0}\Delta_0$. Since we have assumed $\gamma_0^2 \ll \sqrt{T_0}\Delta_0\bar{\gamma}$ we can ascertain that the sweep through the fermion-parity switch will fail to produce a quasiparticle with exponentially small probability.

The Josephson junction thus injects a *single* Bogoliubov quasiparticle into the metal probe, in a pure state with wave function $\psi$ given by Eq. (5.25). The transfer of this quasiparticle is observable as an electrical current pulse, with expectation value

$$I(t) = e\int_0^\infty\frac{dE}{2\pi}\int_0^\infty\frac{dE'}{2\pi}\,e^{i(E'-E)t}\psi^*(E')\sigma_z\psi(E). \tag{5.27}$$

The expectation value of the total transferred charge $Q = \int_{-\infty}^{\infty}I(t)dt$ is given by

$$Q = \frac{2\pi e}{\gamma_0^2}(\lambda_+^2-\lambda_-^2)e^{\pi\delta^2/4}\int_0^\infty dE\left(|u(E)|^2-|v(E)|^2\right). \tag{5.28}$$

*Eq. (5.26) describes two equivalent copies of the single-particle excitation $\psi(E)$, one at $E>0$ and one at $E<0$. This double-counting is inherent in the Nambu representation of superconducting quasiparticles. It plays no role in Eqs. (5.27) and (5.28), where we restrict ourselves to $E>0$. In Eq. (5.30) we correct for double-counting by replacing the usual prefactor $1/2\pi$ by $1/4\pi$.

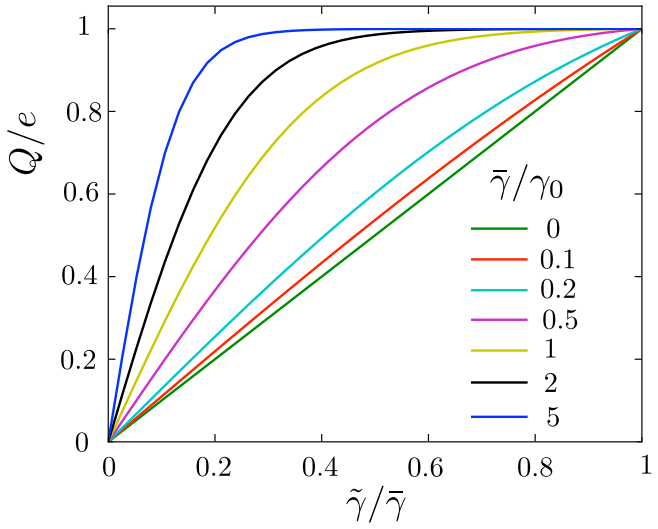


**Figure 5.4:** Expectation value of the charge of the quasiparticle transferred between the superconductor and a single-channel metal probe, following a fermion-parity switch with rapidity $\gamma_0$. The charge $Q$ is given as a function of the ratio $\tilde{\gamma}/\bar{\gamma}$ of the geometric and arithmetic mean of the coupling energies to the two Majorana operators involved in the transition. The curves are calculated numerically from Eq. (5.28). The quenched and adiabatic limits are given by Eqs. (5.29) and (5.32).

For definiteness we take $\lambda_+^2 \geq \lambda_-^2$ in what follows (otherwise the sign of currents and charges should be inverted).

## 5.5 Transferred charge

*Single-channel probe* A single quasiparticle passes through the NS interface irrespective of the rapidity $\gamma_0$, but the transferred charge differs. Fig. 5.4 shows results from a numerical evaluation of Eq. (5.28). Analytical results can be obtained in the quenched limit $\gamma_0 \gg \gamma_1, \gamma_2$ of a fast fermion-parity switch and in the opposite adiabatic limit $\gamma_0 \ll \gamma_1, \gamma_2$ of a slow switch.

In the quenched limit we set $\delta \to 0$ and since $U(0, \frac{1}{2}; -i\varepsilon^2) = 1$ we have $u \to \exp(i\varepsilon^2/2)$, $v \to 0$. The current and transferred charge evaluate to

$$I_{\text{quench}}(t) = 2\pi e\tilde{\gamma}\exp(-2\pi\bar{\gamma}t)\theta(t),\ Q_{\text{quench}} = e\tilde{\gamma}/\bar{\gamma}. \tag{5.29}$$

This is the result (5.2) stated above.

The adiabatic limit may be obtained, with some effort, from the Fourier transform (5.27) in saddle-point approximation, or more easily by starting directly from the general scattering formula [16,19,29,34]

$$I_{\text{adiabatic}}(t) = \frac{ie}{4\pi} \operatorname{Tr} S_{\text{F}}^{\dagger}(0,t)\sigma_z \frac{\partial}{\partial t} S_{\text{F}}(0,t). \tag{5.30}$$

(A self-contained derivation of this formula is given in App. 5.C.) The adiabatic charge transfer is described by the "frozen" scattering matrix

$$S_{\text{F}}(E,t) = S_0(E)|_{\phi\equiv\phi(t)}, \tag{5.31}$$

with $S_0$ from Eq. (5.7) evaluated for a fixed value $\phi(t)$ of the phase across the Josephson junction. The result is

$$I_{\text{adiabatic}}(t) = \frac{e\sqrt{\gamma_1\gamma_2}}{\pi^2\gamma_1\gamma_2/\gamma_0^2 + \gamma_0^2 t^2}, \; Q_{\text{adiabatic}} = e. \tag{5.32}$$

The exponential versus Lorentzian current profiles (5.29) and (5.32) have the same form as in the non-superconducting problem of Ref. 90, but there the transferred quasiparticle was an electron of charge $e$. Here what is transferred is a Bogoliubov quasiparticle, which is not in an eigenstate of charge. In the quenched limit $Q$ can vary between 0 and $e$, depending on the ratio of the geometric and arithmetic mean of the two coupling energies $\gamma_1$, $\gamma_2$ of the metal probe to the Majorana operators of the zero-mode. A nearly charge-neutral quasiparticle is transferred if $\gamma_1 \ll \gamma_2$, when $Q = 2e\sqrt{\gamma_1/\gamma_2}$ in the quenched limit.

*Multi-channel probe* So far we have assumed that the metal probe supports a single electron-hole channel. More generally, the coupling between the superconductor and the metal would involve $N$ electron-hole channels, where $N$ would include both orbital and spin degrees of freedom. This multi-channel generalization is worked out in App. 5.D. A single quasiparticle is injected, as before, with a reduced charge $Q_N = \mathscr{R}Q_1$. The reduction factor $\mathscr{R} \in [0,1]$ is independent of the rapidity $\gamma_0$. It is determined entirely by the point contact conductance, which at the fermion parity switch has a resonant peak of height

$$G_{\text{peak}} = \frac{4e^2}{h}(1-\mathscr{R}^2). \tag{5.33}$$

## 5.6 Conclusion

In conclusion, we have investigated the phase-coherent, deterministic counterpart of incoherent, stochastic quasiparticle poisoning: A fermion-parity switch in a Josephson junction transfers a single quasiparticle into a metal contact, on demand and in a pure state. The quasiparticle is a coherent superposition of electron and hole, with a charge expectation value that can be adjusted between 0 and $e$. A nearly charge-neutral quasiparticle is produced in the quenched limit of a fast parity switch, if the metal couples predominantly to a single Majorana operator in the Josephson junction. This device could be used for superconducting analogues of single-electron collision experiments,[30,31,52,64,121,136] such as the Hanbury-Brown-Twiss or Hong-Ou-Mandel interferometer for Majorana fermions.[22,62]

Experimentally, one can determine the value of $Q$ by sweeping up and down through the fermion-parity switch and measuring the shot noise power $P_{\text{shot}}$. In each period $\tau$ a charge $\{0,+e,-e\}$ is transferred with probability $\{1-2p(1-p),p(1-p),p(1-p)\}$, where $Q/e=|1-2p|$ is the average charge transferred during a sweep up or down. The full distribution of the transferred charge is trinomial. The first moment vanishes and the second moment is given by

$$P_{\text{shot}} = 2p(1-p)(e^2/\tau) = \tfrac{1}{2}\tau^{-1}(e^2-Q^2). \tag{5.34}$$

Referring to the model calculation of Fig. 5.2, a band width of $\sqrt{T}_0\Delta_0 \simeq 10\,\text{GHz}$ at a driving frequency of $1/\tau \simeq 0.1\,\text{GHz}$ would imply a rapidity $\gamma_0 \simeq 1\,\text{GHz}$ (so that $\gamma_0^2\tau \simeq \sqrt{T}_0\Delta_0$). The escape rate $\bar{\gamma}$ could then vary between, say, 0.2 GHz and 2 GHz to vary between the adiabatic and the quenched regime. These frequencies should all lie above the decoherence rate of the Bogoliubov quasiparticle due to charge noise, which could be below 1 MHz.[156]

An alternative way to measure the transferred charge is to apply a voltage $V$ between the two superconductors. The phase will then advance with constant rate $d\phi/dt = 2eV/\hbar$, producing a current $I = Q \times 2eV/h$ (assuming a single level crossing in a $2\pi$ phase interval).

# 5.A Model Hamiltonian

The model Hamiltonian for the nanowire Josephson junction of Fig. 5.5 has the Bogoliubov-De Gennes form

$$H = \begin{pmatrix} H_0(\mathbf{p}) & \Delta \\ \Delta^* & -\sigma_y H_0^*(-\mathbf{p})\sigma_y \end{pmatrix}, \tag{5.35a}$$

$$H_0 = \frac{\mathbf{p}^2}{2m_{\rm eff}} - E_{\rm F} + \frac{\alpha_{\rm so}}{\hbar}(\sigma_x p_y - \sigma_y p_x) + \tfrac{1}{2} g_{\rm eff}\mu_{\rm B} B\sigma_x + V_0\,[\Theta(x - W_{\rm B}/2) - \Theta(x - W_{\rm B}/2)]. \tag{5.35b}$$

Electrons and holes are coupled by the induced $s$-wave pair potential $\Delta$ at the superconducting contacts, with a phase difference $\phi$. The single-particle Hamiltonian $H_0$ contains Rashba spin-orbit coupling and the Zeeman energy of a magnetic field parallel to the nanowire. A potential barrier of strength $V_0$ and width $W_{\rm B}$ is located at the center of the junction.

The Hamiltonian $H$ is discretized on a square lattice, to obtain a tight-binding model.[71] For the parameters indicated in the figure, the Josephson junction is in the nontrivial regime,[120,135] with a pair of Majorana zero-modes at the normal-superconducting (NS) interface, weakly coupled via the potential barrier. A normal-metal lead is attached perpendicular to the nanowire, coupling predominantly to one of the two zero-modes.

To obtain the complex energies of the quasibound states, the imaginary part of the lead self-energy is added to the tight-binding Hamiltonian of the junction. Diagonalization of this non-Hermitian Hamiltonian yields the complex eigenvalues $E_n(\phi) - i\Gamma_n(\phi)$ plotted in Fig. 5.2.

# 5.B Details of the calculation of the Green's function

## 5.B.1 Evaluation of the determinant

Since the expression (5.16) for the Green's function contains both the matrix $X(E)$ and its inverse, we need to evaluate the determinant of this $2 \times 2$ matrix. As a first step we will show that $\mathrm{Det}\,X$ is energy independent. This can be done directly from the differential equation (5.18) for $X$.

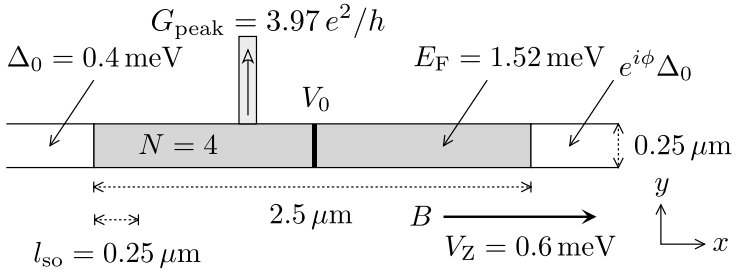


**Figure 5.5:** Nanowire Josephson junction modeled by the Hamiltonian (5.35), discretized on a square lattice (lattice constant $a = 25\,\mathrm{nm}$). The InSb nanowire is grey, with a tunnel barrier (width 25 nm) in black, the superconducting contacts are yellow, the normal-metal probe (width 100 nm) is blue. There are 4 electron subbands in the nanowire and 8 in the probe, counting spin. The peak conductance at the fermion-parity switch is indicated.

We write the determinant in the form

$$\mathrm{Det}\, X(E) = \begin{pmatrix} u^*(-E) \\ v^*(-E) \end{pmatrix}^{\mathrm{T}} \sigma_z \begin{pmatrix} u(E) \\ v(E) \end{pmatrix}, \tag{5.36}$$

and take the derivative with respect to $E$. The functions $u, v$ solve

$$\left(i\gamma_0^2 \sigma_z d/dE + E + i\pi\Lambda^2\right) \begin{pmatrix} u \\ v \end{pmatrix} = 0. \tag{5.37}$$

This allows us to express the derivatives

$$\frac{d}{dE} \begin{pmatrix} u(E) \\ v(E) \end{pmatrix} = \frac{i}{\gamma_0^2} \sigma_z (E + i\pi\Lambda^2) \begin{pmatrix} u(E) \\ v(E) \end{pmatrix}, \tag{5.38}$$

$$\frac{d}{dE} \begin{pmatrix} u^*(-E) \\ v^*(-E) \end{pmatrix} = -\frac{i}{\gamma_0^2} \sigma_z (E + i\pi\Lambda^{*2}) \begin{pmatrix} u^*(-E) \\ v^*(-E) \end{pmatrix}. \tag{5.39}$$

Since $\Lambda$ is a real and symmetric matrix, it follows that

$$\begin{aligned} \frac{d}{dE} \mathrm{Det}\, X &= \frac{i}{\gamma_0^2} \begin{pmatrix} u^*(-E) \\ v^*(-E) \end{pmatrix}^{\mathrm{T}} [(E + i\pi\Lambda^2) \\ &\quad - (E + i\pi\Lambda^{*2})^{\mathrm{T}}] \begin{pmatrix} u(E) \\ v(E) \end{pmatrix} \\ &= 0, \end{aligned} \tag{5.40}$$

so $\mathrm{Det}\, X$ is independent of $E$.

From Eq. (5.22) we have an explicit expression for the determinant of $X$:

$$\begin{aligned}\mathrm{Det}\,X = {} & U(-\tfrac{1}{4}i\delta^2, \tfrac{1}{2}; -i\varepsilon^2)U(\tfrac{1}{4}i\delta^2, \tfrac{1}{2}; i\varepsilon^2) \\ & - \tfrac{1}{4}\delta^2 U(\tfrac{1}{2} - \tfrac{1}{4}i\delta^2, \tfrac{1}{2}; -i\varepsilon^2)U(\tfrac{1}{2} + \tfrac{1}{4}i\delta^2, \tfrac{1}{2}; i\varepsilon^2). \end{aligned} \tag{5.41}$$

This is an analytic function of $\varepsilon = (E + i\pi\bar{\gamma})/\gamma_0$, which is independent of $E$ and hence independent of $\varepsilon$. At $\varepsilon = 0$ we may evaluate it by means of the identities [1]

$$U(a, \tfrac{1}{2}, 0) = \frac{\sqrt{\pi}}{\Gamma(\frac{1}{2} + a)}, \tag{5.42}$$

$$\begin{aligned}\Gamma(\tfrac{1}{2} + ia)\Gamma(\tfrac{1}{2} - ia) &= \frac{\pi}{\cosh \pi a}, \\ \Gamma(1 + ia)\Gamma(1 - ia) &= \frac{\pi a}{\sinh \pi a}. \end{aligned} \tag{5.43}$$

Substitution into Eq. (5.41) at $\varepsilon = 0$ gives

$$\mathrm{Det}\,X = \exp(-\pi\delta^2/4), \tag{5.44}$$

as in Eq. (5.23).

## 5.B.2 Normalization of the excited state

We wish to demonstrate that the wave function (5.25) of the single-particle excited state is normalized to unity. For that purpose we need to evaluate the integral

$$\mathcal{N} \equiv \langle \psi | \psi \rangle = \int_0^\infty \frac{2\pi dE}{\gamma_0^2 \mathrm{Det}\,X} \begin{pmatrix} u^*(E) \\ v^*(E) \end{pmatrix}^{\mathrm{T}} \Lambda^2 \begin{pmatrix} u(E) \\ v(E) \end{pmatrix}. \tag{5.45}$$

We again use the fact that $u, v$ solve Eq. (5.37). Substitution into Eq. (5.45) gives (denoting $u' = du/dE$)

$$\begin{aligned}\mathcal{N} &= \frac{-2}{\mathrm{Det}\,X} \int_0^\infty dE \left[ u^* u' - v^* v' - iE\gamma_0^{-2}(uu^* + vv^*) \right] \\ &= \frac{2}{\mathrm{Det}\,X} \left( |u(0)|^2 - |v(0)|^2 \right) \\ &\quad + \frac{2}{\mathrm{Det}\,X} \int_0^\infty dE \left[ uu^{*\prime} - vv^{*\prime} + iE\gamma_0^{-2}(uu^* + vv^*) \right] \\ &= 2 - \mathcal{N}^*, \end{aligned} \tag{5.46}$$

and because $\mathcal{N}$ is real, we indeed have $\mathcal{N} = 1$. Notice that $\langle\psi|\psi\rangle = 1$ also implies $\langle\Psi_1|\Psi_1\rangle = 1$ in Eq. (5.26).

## 5.C Scattering formula for the charge transfer in the adiabatic regime

The current passing through the NS interface in the adiabatic regime $\gamma_0 \ll \gamma_1, \gamma_2$ of a slow fermion-parity switch can be evaluated most easily from the scattering formula (5.30), which is the analogue for Bogoliubov quasiparticles of a well-known formula for normal electrons.[16,19,29,34] For completeness we give a derivation of Eq. (5.30).

One subtlety in this derivation is that Fourier transforms of quasiparticle annihilation operators $a(E)$ to the time domain need to include both positive and negative energies in order to produce a complete basis set. This results in a double counting of the quasiparticle excitations, because of the relation $a(-E) = \sigma_x a^\dagger(E)$. To correct for the double counting we include a factor 1/2 in the definition of the current operator,[22]

$$\begin{aligned} \mathscr{I}(t) &= \tfrac{1}{2} e a^\dagger_{\mathrm{out}}(t)\sigma_z a_{\mathrm{out}}(t), \\ a_{\mathrm{out}}(t) &= \int_{-\infty}^{\infty} \frac{dE}{2\pi}\, e^{-iEt} a_{\mathrm{out}}(E). \end{aligned} \tag{5.47}$$

The outgoing and incoming operators are related by the scattering matrix,

$$a_{\mathrm{out}}(E) = \int_{-\infty}^{\infty} \frac{dE'}{2\pi} S(E,E') a_{\mathrm{in}}(E'), \tag{5.48}$$

which satisfies the unitarity condition

$$\begin{aligned} \int_{-\infty}^{\infty} \frac{dE'}{2\pi} \sum_{n'} S_{nn'}(E_1,E') S^*_{mn'}(E_2,E') \\ = 2\pi\delta_{nm}\delta(E_1 - E_2). \end{aligned} \tag{5.49}$$

The incoming operators have the equilibrium expectation value

$$\langle a^\dagger_n(E) a_m(E')\rangle = 2\pi\delta(E-E')\delta_{nm} f(E), \tag{5.50}$$

with $f(E) = (1 + e^{(E/kT)^{-1}}$ the Fermi function at temperature $T$. We seek

the current expectation value $I(t) \equiv \langle \mathscr{I}(t) \rangle$, given by

$$I(t) = \tfrac{1}{2} e \int_{-\infty}^{\infty} \frac{dE}{2\pi} \int_{-\infty}^{\infty} \frac{dE'}{2\pi} \int_{-\infty}^{\infty} \frac{d\omega}{2\pi} e^{i\omega t} \times f(E') \mathrm{Tr}\, S^{\dagger}(E+\omega, E') \sigma_z S(E, E'). \tag{5.51}$$

Because of the unitarity condition (5.49), the integral over $E'$ without the factor $f(E')$ vanishes,

$$\int_{-\infty}^{\infty} \frac{dE'}{2\pi} \mathrm{Tr}\, S^{\dagger}(E+\omega, E') \sigma_z S(E, E') = 2\pi\delta(\omega) \mathrm{Tr}\, \sigma_z = 0. \tag{5.52}$$

We may therefore equivalently write

$$I(t) = \tfrac{1}{2} e \int_{-\infty}^{\infty} \frac{dE}{2\pi} \int_{-\infty}^{\infty} \frac{dE'}{2\pi} \int_{-\infty}^{\infty} \frac{d\omega}{2\pi} e^{i\omega t} \times [f(E') - f(E)] \mathrm{Tr}\, S^{\dagger}(E+\omega, E') \sigma_z S(E, E'). \tag{5.53}$$

It is convenient to introduce the Wigner transform

$$S_{\mathrm{W}}(E, t) = \int_{-\infty}^{\infty} \frac{dE'}{2\pi} e^{-iE't} S(E + \tfrac{1}{2}E', E - \tfrac{1}{2}E'), \tag{5.54}$$

because it becomes the frozen scattering matrix $S_{\mathrm{F}}(E, t)$ from Eq. (5.31) in the adiabatic limit.[174] More precisely,

$$S_{\mathrm{W}}(E + \delta E, t) = S_{\mathrm{F}}(E, t) + \mathscr{O}(\gamma_0 / E_{\mathrm{c}}) + \mathscr{O}(\delta E / E_{\mathrm{c}}), \tag{5.55}$$

with $E_{\mathrm{c}} = \min(\gamma_1, \gamma_2)$ the width of the quasi-bound state.

Fourier transformation of the time variable gives

$$S_{\mathrm{W}}(E, \omega) = \int_{-\infty}^{\infty} dt\, e^{i\omega t} S_{\mathrm{W}}(E, t) = S(E + \tfrac{1}{2}\omega, E - \tfrac{1}{2}\omega). \tag{5.56}$$

In terms of $S_{\mathrm{W}}(E, \omega)$ the expression (5.53) for the current reads

$$I(t) = \tfrac{1}{2} e \int_{-\infty}^{\infty} \frac{d\bar{E}}{2\pi} \int_{-\infty}^{\infty} \frac{d\omega'}{2\pi} \int_{-\infty}^{\infty} \frac{d\omega}{2\pi} e^{i\omega t} \times \left[ f(\bar{E} - \tfrac{1}{2}\omega') - f(\bar{E} + \tfrac{1}{2}\omega') \right] \times \mathrm{Tr}\, S_{\mathrm{W}}^{\dagger}(\bar{E} + \tfrac{1}{2}\omega, \omega + \omega') \sigma_z S_{\mathrm{W}}(\bar{E}, \omega'), \tag{5.57}$$

with the definitions $\bar{E} = \frac{1}{2}(E + E')$, $\omega' = E - E'$.

The integrals over $\omega$ and $\omega'$ contribute over the range $-\gamma_0 \lesssim \omega, \omega' \lesssim \gamma_0$. To leading order in $\gamma_0$ we therefore have

$$\begin{aligned} &\mathrm{Tr}\, S_{\mathrm{W}}^{\dagger}(\bar{E} + \tfrac{1}{2}\omega, \omega + \omega')\sigma_z S_{\mathrm{W}}(\bar{E}, \omega') = \\ &\quad \mathrm{Tr}\, S_{\mathrm{F}}^{\dagger}(\bar{E}, \omega + \omega')\sigma_z S_{\mathrm{F}}(\bar{E}, \omega') + \mathcal{O}(\gamma_0/E_{\mathrm{c}}), \end{aligned} \tag{5.58}$$

in view of Eq. (5.55). Substitution into Eq. (5.57), with a change of variables $\omega'' = \omega + \omega'$, results in

$$\begin{aligned} I(t) &= \tfrac{1}{2} e \int_{-\infty}^{\infty} \frac{d\bar{E}}{2\pi} \int_{-\infty}^{\infty} \frac{d\omega'}{2\pi} \int_{-\infty}^{\infty} \frac{d\omega''}{2\pi}\, e^{i(\omega'' - \omega')t} \\ &\quad \times \left[ f(\bar{E} - \tfrac{1}{2}\omega') - f(\bar{E} + \tfrac{1}{2}\omega') \right] \\ &\quad \times \mathrm{Tr}\, S_{\mathrm{F}}^{\dagger}(\bar{E}, \omega'')\sigma_z S_{\mathrm{F}}(\bar{E}, \omega')[1 + \mathcal{O}(\gamma_0/E_{\mathrm{c}})] \\ &= \tfrac{1}{2} e \int_{-\infty}^{\infty} \frac{d\bar{E}}{2\pi} \int_{-\infty}^{\infty} \frac{d\omega}{2\pi}\, e^{-i\omega t} \\ &\quad \times \left[ f(\bar{E} - \tfrac{1}{2}\omega) - f(\bar{E} + \tfrac{1}{2}\omega) \right] \\ &\quad \times \mathrm{Tr}\, S_{\mathrm{F}}^{\dagger}(\bar{E}, t)\sigma_z S_{\mathrm{F}}(\bar{E}, \omega)[1 + \mathcal{O}(\gamma_0/E_{\mathrm{c}})]. \end{aligned} \tag{5.59}$$

Since we do not wish to assume that $\gamma_0$ is small compared to $kT$, we expand the difference of Fermi functions in square brackets to all order in $\omega$,

$$\begin{aligned} &[f(\bar{E} - \tfrac{1}{2}\omega) - f(\bar{E} + \tfrac{1}{2}\omega)]e^{-i\omega t} = \\ &\quad = -2 \sum_{p=0}^{\infty} \frac{(\omega/2)^{2p+1}}{(2p+1)!} \frac{\partial^{2p}}{\partial \bar{E}^{2p}} f'(\bar{E}) e^{-i\omega t} \\ &\quad = -\left( \sum_{p=0}^{\infty} \frac{(i/2)^{2p}}{(2p+1)!} \frac{\partial^{2p}}{\partial \bar{E}^{2p}} \frac{\partial^{2p}}{\partial t^{2p}} \right) f'(\bar{E}) \omega e^{-i\omega t}. \end{aligned} \tag{5.60}$$

Upon partial integration, the sum over $p$ contributes to the integral (5.59) terms of order

$$\frac{\partial^{2p}}{\partial \bar{E}^{2p}} \frac{\partial^{2p}}{\partial t^{2p}} S_{\mathrm{F}}(\bar{E}, t) = \mathcal{O}(\gamma_0/E_{\mathrm{c}})^{2p}, \tag{5.61}$$

so only the $p = 0$ term needs to be retained to leading order.

We thus arrive at

$$\begin{aligned} I(t) &= -\tfrac{1}{2}e\int_{-\infty}^{\infty}\frac{d\bar{E}}{2\pi}\int_{-\infty}^{\infty}\frac{d\omega}{2\pi}f'(\bar{E})\omega e^{-i\omega t} \\ &\quad\times \mathrm{Tr}\, S_{\mathrm{F}}^{\dagger}(\bar{E},t)\sigma_z S_{\mathrm{F}}(\bar{E},\omega)[1+\mathcal{O}(\gamma_0/E_{\mathrm{c}})] \\ &= -\tfrac{1}{2}ie\int_{-\infty}^{\infty}\frac{d\bar{E}}{2\pi}f'(\bar{E}) \\ &\quad\times \mathrm{Tr}\, S_{\mathrm{F}}^{\dagger}(\bar{E},t)\sigma_z\frac{\partial}{\partial t}S_{\mathrm{F}}(\bar{E},t)[1+\mathcal{O}(\gamma_0/E_{\mathrm{c}})]. \end{aligned} \tag{5.62}$$

At zero temperature, when $-f'(E)\to\delta(E)$, we recover Eq. (5.30),

$$I_{\mathrm{adiabatic}}(t) = \frac{ie}{4\pi}\mathrm{Tr}\, S_{\mathrm{F}}^{\dagger}(0,t)\sigma_z\frac{\partial}{\partial t}S_{\mathrm{F}}(0,t). \tag{5.63}$$

# 5.D Multi-channel probe

## 5.D.1 Coupling matrix

In the main text we assumed that the pair of Andreev levels near the level crossing is coupled to a *single* pair of electron-hole modes in the normal-metal probe. This coupling is described by the $2\times 2$ coupling matrix $W$ defined in Eq. (5.9). More generally, a multi-channel probe has a $2\times 2N$ coupling matrix of the form

$$W=(W_1,W_2,\dots W_N),\ W_n=\begin{pmatrix}\alpha_n & \beta_n^*\\ \beta_n & \alpha_n^*\end{pmatrix}, \tag{5.64}$$

constrained by particle-hole symmetry: $W=\sigma_x W^*\sigma_x$. We collect the complex coefficients $\alpha_n,\beta_n$ in a pair of vectors,

$$\boldsymbol{\alpha}=(\alpha_1,\alpha_2,\dots\alpha_N),\ \boldsymbol{\beta}=(\beta_1,\beta_2,\dots\beta_N), \tag{5.65}$$

and define the inner products

$$\begin{aligned} &\langle\boldsymbol{\alpha}|\boldsymbol{\alpha}\rangle=\sum_{n=1}^{N}|\alpha_n|^2,\ \langle\boldsymbol{\beta}|\boldsymbol{\beta}\rangle=\sum_{n=1}^{N}|\beta_n|^2,\\ &\langle\boldsymbol{\alpha}|\boldsymbol{\beta}\rangle=\sum_{n=1}^{N}\alpha_n^*\beta_n. \end{aligned} \tag{5.66}$$

The decay rates $\gamma_1$, $\gamma_2$ of the pair of quasibound Andreev levels are the eigenvalues of the $2\times 2$ matrix

$$\begin{aligned} WW^\dagger &= \sum_{n=1}^{N} W_n W_n^\dagger \\ &= \begin{pmatrix} \langle\boldsymbol{\alpha}|\boldsymbol{\alpha}\rangle + \langle\boldsymbol{\beta}|\boldsymbol{\beta}\rangle & 2\langle\boldsymbol{\alpha}|\boldsymbol{\beta}\rangle^* \\ 2\langle\boldsymbol{\alpha}|\boldsymbol{\beta}\rangle & \langle\boldsymbol{\alpha}|\boldsymbol{\alpha}\rangle + \langle\boldsymbol{\beta}|\boldsymbol{\beta}\rangle \end{pmatrix}, \end{aligned} \tag{5.67}$$

$$\Rightarrow \begin{cases} \gamma_1 = \langle\boldsymbol{\alpha}|\boldsymbol{\alpha}\rangle + \langle\boldsymbol{\beta}|\boldsymbol{\beta}\rangle + 2|\langle\boldsymbol{\alpha}|\boldsymbol{\beta}\rangle|, \\ \gamma_2 = \langle\boldsymbol{\alpha}|\boldsymbol{\alpha}\rangle + \langle\boldsymbol{\beta}|\boldsymbol{\beta}\rangle - 2|\langle\boldsymbol{\alpha}|\boldsymbol{\beta}\rangle|. \end{cases} \tag{5.68}$$

As before, we define the arithmetic and geometric averages,

$$\bar{\gamma} = \tfrac{1}{2}(\gamma_1+\gamma_2),\ \tilde{\gamma} = \sqrt{\gamma_1\gamma_2}. \tag{5.69}$$

For later use, we also note that

$$W\sigma_z W^\dagger = \sum_{n=1}^{N} W_n\sigma_z W_n^\dagger = \big(\langle\boldsymbol{\alpha}|\boldsymbol{\alpha}\rangle - \langle\boldsymbol{\beta}|\boldsymbol{\beta}\rangle\big)\sigma_z. \tag{5.70}$$

## 5.D.2 Scattering matrix

Carrying through the same steps as in the single-channel case, we have the following expression for the $2N\times 2N$ scattering matrix $S$ in terms of the $2\times 2$ Green's function $G$:

$$\begin{aligned} &S(E,E') = 2\pi\delta(E-E') - 2\pi i W^\dagger G(E,E')W, \\ &\left(i\gamma_0^2\sigma_z\frac{\partial}{\partial E} + E + i\pi WW^\dagger\right)G(E,E') = 2\pi\delta(E-E'). \end{aligned} \tag{5.71}$$

The solution for $G$ has the factorized form (5.16), in terms of the $2\times 2$ matrix

$$X(E) = \begin{pmatrix} u(E) & v^*(-E) \\ v(E) & u^*(-E) \end{pmatrix} \tag{5.72}$$

that solves the homogeneous equation

$$\left(i\gamma_0^2\sigma_z\frac{\partial}{\partial E} + E + i\pi WW^\dagger\right)X(E) = 0. \tag{5.73}$$

The functions $u$ and $v$ are determined by

$$\gamma_0^2 u'' + (\varepsilon^2 + \delta^2 - i)u = 0,\ \zeta v = i\varepsilon u - \gamma_0 u', \tag{5.74}$$

$$\varepsilon = (E + i\pi\bar{\gamma})/\gamma_0,\ \zeta = (2\pi/\gamma_0)\langle \boldsymbol{\alpha}|\boldsymbol{\beta}\rangle^*, \tag{5.75}$$

$$\delta = |\zeta| = \tfrac{1}{2}(\pi/\gamma_0)(\gamma_1 - \gamma_2). \tag{5.76}$$

The solution is

$$u(E) = e^{i\varepsilon^2/2} U(-\tfrac{1}{4}i\delta^2, \tfrac{1}{2}; -i\varepsilon^2), \tag{5.77}$$

$$\zeta v(E) = -\tfrac{1}{2}\delta^2 e^{i\pi/4} e^{i\varepsilon^2/2} U(\tfrac{1}{2} - \tfrac{1}{4}i\delta^2, \tfrac{1}{2}; -i\varepsilon^2). \tag{5.78}$$

Finally, the scattering matrix has the dyadic form

$$S_{nm}(E,E')|_{E>E'} = -\psi_n(E)\psi_m^*(-E'), \tag{5.79}$$

$$\psi(E) = (2\pi/\gamma_0) e^{\pi\delta^2/8} W^\dagger \begin{pmatrix} u(E) \\ v(E) \end{pmatrix}. \tag{5.80}$$

## 5.D.3 Transferred charge

Because the scattering matrix is still of rank-one, a single quasiparticle is transferred as a result of the fermion-parity switch, irrespective of the number of channels $N$ in the metal probe. The charge expectation value of this quasiparticle is given by

$$\begin{aligned} Q &= e\int_0^\infty \frac{dE}{2\pi} \psi^*(E)\sigma_z\psi(E) \\ &= \frac{2\pi e}{\gamma_0^2} e^{\pi\delta^2/4} \int_0^\infty dE \begin{pmatrix} u^*(E) \\ v^*(E) \end{pmatrix} W\sigma_z W^\dagger \begin{pmatrix} u(E) \\ v(E) \end{pmatrix} \\ &= \frac{2\pi e}{\gamma_0^2} e^{\pi\delta^2/4} (\langle \boldsymbol{\alpha}|\boldsymbol{\alpha}\rangle - \langle \boldsymbol{\beta}|\boldsymbol{\beta}\rangle) \int_0^\infty dE \left(|u(E)|^2 - |v(E)|^2\right). \end{aligned} \tag{5.81}$$

Comparison with Eq. (5.28) shows that the transferred charge for a multi-channel contact differs from that in the single-channel case by a reduction factor

$$\begin{aligned} \mathscr{R} &= \frac{\langle \boldsymbol{\alpha}|\boldsymbol{\alpha}\rangle - \langle \boldsymbol{\beta}|\boldsymbol{\beta}\rangle}{\tilde{\gamma}} \\ &= \frac{\langle \boldsymbol{\alpha}|\boldsymbol{\alpha}\rangle - \langle \boldsymbol{\beta}|\boldsymbol{\beta}\rangle}{\sqrt{(\langle \boldsymbol{\alpha}|\boldsymbol{\alpha}\rangle + \langle \boldsymbol{\beta}|\boldsymbol{\beta}\rangle)^2 - 4|\langle \boldsymbol{\alpha}|\boldsymbol{\beta}\rangle|^2}} \in [0,1], \end{aligned} \tag{5.82}$$

independent of the rapidity $\gamma_0$ of the fermion-parity switch.

As a check, we can directly compute the transferred charge in the adiabatic limit from Eq. (5.30). Substitution of the frozen scattering matrix at the Fermi level,

$$S_0 = 1 + 2\pi i W^\dagger (E_0\sigma_z - i\pi WW^\dagger)^{-1} W, \tag{5.83}$$

gives the charge

$$\begin{aligned} Q_{\text{adiabatic}} &= \frac{ie}{4\pi}\int_{-\infty}^{\infty} dE_0\, \mathrm{Tr}\, S_0^\dagger \sigma_z \frac{\partial S_0}{\partial E_0} \\ &= \frac{e}{2}\int_{-\infty}^{\infty} dE_0\, \mathrm{Tr}(E_0\sigma_z + i\pi WW^\dagger)^{-1} W\sigma_z W^\dagger (E_0\sigma_z - i\pi WW^\dagger)^{-1}\sigma_z \\ &= e\big(\langle \boldsymbol{\alpha}|\boldsymbol{\alpha}\rangle - \langle \boldsymbol{\beta}|\boldsymbol{\beta}\rangle\big)\int_{-\infty}^{\infty} dE_0\, (E_0^2 + \pi^2\tilde{\gamma}^2)^{-1} \\ &= e\mathscr{R}. \end{aligned} \tag{5.84}$$

## 5.D.4 Relation of the reduction factor to the Andreev conductance

The charge reduction factor $\mathscr{R}$ from Eq. (5.82) is a property of the coupling matrix of the normal-metal probe to the Josephson junction. It can be expressed in terms of an independently measurable quantity, the Andreev conductance.

When the normal-metal probe is biased at a voltage $V$, a current $I$ is driven into the grounded superconductor by the process of Andreev reflection. The Andreev conductance $G_\mathrm{A} = \lim_{V\to 0} dI/dV$ is related to the scattering matrix $S_0$ at the Fermi level by

$$G_\mathrm{A} = \frac{e^2}{2h}\,\mathrm{Tr}(1 - S_0\sigma_z {S_0}^\dagger \sigma_z). \tag{5.85}$$

Near the level crossing a resonant peak appears in $G_\mathrm{A}$ as a function of $E_0$, with the Lorentzian line shape

$$G_\mathrm{A} = \frac{4e^2}{h}\,\frac{\pi^2\tilde{\gamma}^2}{E_0^2 + \pi^2\tilde{\gamma}^2}\big(1 - \mathscr{R}^2\big). \tag{5.86}$$

The resonant peak height of $(4e^2/h)(1-\mathscr{R}^2)$ directly determines the charge reduction factor.

# 6 Spin-orbit interaction in InSb nanowires

## 6.1 Introduction

Hybrid semiconductor nanowire-superconductor devices are a promising platform for the study of topological superconductivity.[7] Such devices can host Majorana fermions,[120,135] bound states with non-Abelian exchange statistics. The realization of a stable topological state requires an energy gap that exceeds the temperature at which experiments are performed (~50 mK). The strength of the spin-orbit interaction (SOI) is the main parameter that determines the size of this topological gap[154] and thus the potential of these devices for the study of Majorana fermions. The identification of nanowire devices with a strong SOI is therefore essential. This entails both performing measurements on a suitable material and device geometry as well as establishing theory to extract the SOI strength.

InSb nanowires are a natural candidate to create devices with a strong SOI, since bulk InSb has a strong SOI.[58,179] Nanowires have been used in several experiments that showed the first signatures of Majorana fermions.[40,44,46,128] Nanowires are either fabricated by etching out wires in planar heterostructures or grown bottom-up. The strong confinement in the growth direction makes etched wires two-dimensional (2D) even at high density. SOI has been studied in 2D InSb wires[86] and in planar InSb heterostructures,[87] from which a SOI due to structural inversion asymmetry,[144] a Rashba SOI $\alpha_R$, of 0.03 eVÅ has been obtained.[87] Bottom-up grown nanowires are three-dimensional (3D) when the Fermi wavelength is smaller than the wire diameter. In InSb wires of this type SOI has been studied by performing spectroscopy on quantum dots,[129,132] giving $\alpha_R = 0.16 - 0.22$ eVÅ.[129] However, many (proposed) topological nanowires devices[79,80,178] contain extended conducting regions, i.e. conductive regions along the nanowire much longer than the

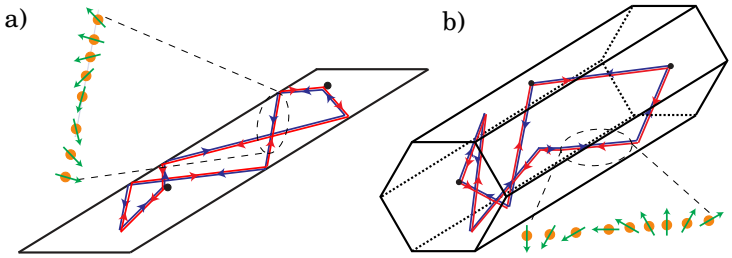


**Figure 6.1:** Quantum interference along time-reversed paths in 2D (a) and 3D (b) nanowires. In both cases an inversion symmetry induces spin precession in between (boundary) scattering events.

nanowire diameter. The SOI strength in these extended regions has not yet been determined. It is likely different from that in quantum dots, as the difference in confinement between both geometries results in a different effective electric field and thus different Rashba SOI. Measurements of SOI strength in extended InSb nanowire regions are therefore needed to evaluate their potential for topological devices. Having chosen a nanowire material, further enhancement of Rashba SOI strength can be realized by choosing a device geometry that enhances the structural inversion asymmetry.[56,133] Our approach is to use a high-k dielectric in combination with a top gate that covers the InSb nanowire.

## 6.2 Magnetoconductance measurements in 3D nanowires

The standard method to extract SOI strength in extended regions is through low-field magnetoconductance (MC) measurements.[78,81] Quantum interference (see Fig. 6.1) in the presence of a strong SOI results in an increased conductance, called weak anti-localization (WAL),[27] that reduces to its classical value when a magnetic field is applied.[10] From fits of MC data to theory a spin relaxation length is extracted. If spin relaxation results from inversion asymmetry a spin precession length and SOI strength can be defined. To extract SOI strength in nanowires the theory should contain (1) the length over which the electron dephases in the presence of a magnetic field, the magnetic dephasing length,[25] and (2) the relation between spin relaxation and spin precession length.[93] The magnetic dephasing and spin relaxation length depend, besides

magnetic field and SOI strength respectively, on dimensionality and confinement. For instance, in nanowires, the spin relaxation length increases when the wire diameter is smaller than the spin precession length[93,94,155]. Therefore the spin relaxation length extracted from WAL is not a direct measure of SOI strength. These effects have been studied in 2D wires,[25,93] but results for 3D wires are lacking. As geometry and dimensionality are different (see Fig. 6.1), using 2D results for 3D wires is unreliable. Thus, theory for 3D wires has to be developed.

In this chapter, we first theoretically study both magnetic dephasing and spin relaxation due to Rashba SOI in 3D hexagonal nanowires. We then use this theory to determine the spin-orbit strength from our measurements of WAL in dual-gate InSb nanowire devices, finding a strong Rashba SOI $\alpha_{\mathrm{R}} = 0.5 - 1\,\mathrm{eV\,\AA}$.

The WAL correction to the classical conductivity can be computed in the quasiclassical theory as[25,37,106]

$$\begin{aligned}\Delta G = -\frac{e^2}{h}\frac{1}{L}\Big[3\Big(\frac{1}{l_\varphi^2}+\frac{4}{3l_{\mathrm{so}}^2}+\frac{1}{l_B^2}\Big)^{-\frac{1}{2}}-\Big(\frac{1}{l_\varphi^2}+\frac{1}{l_B^2}\Big)^{-\frac{1}{2}}\\ -3\Big(\frac{1}{l_\varphi^2}+\frac{4}{3l_{\mathrm{so}}^2}+\frac{d}{l_e^2}+\frac{1}{l_B^2}\Big)^{-\frac{1}{2}}+\Big(\frac{1}{l_\varphi^2}+\frac{d}{l_e^2}+\frac{1}{l_B^2}\Big)^{-\frac{1}{2}}\Big].\end{aligned} \tag{6.1}$$

The length scales in this expression are the nanowire length $L$, the mean free path $l_e$, the phase coherence length $l_\varphi$, the magnetic dephasing length $l_B$, and the spin relaxation length $l_{\mathrm{so}}$. The mean free path $l_e = v_{\mathrm{F}}\tau_e$ where $\tau_e$ is the mean time between scattering events and $v_{\mathrm{F}}$ the Fermi velocity. In addition, the remaining length scales are also related to corresponding time scales as

$$l_{B,\varphi,\mathrm{so}} = \sqrt{D\tau_{B,\varphi,\mathrm{so}}}. \tag{6.2}$$

where $D = \frac{1}{d}v_{\mathrm{F}}l_e$ the diffusion constant in $d$ dimensions ($d = 3$ for bottom-up grown nanowires).

In the quasiclassical theory, $\tau_\varphi$ (and hence $l_\varphi$) is a phenomenological parameter. In contrast, $\tau_B$ and $\tau_{\mathrm{so}}$ are computed from a microscopic Hamiltonian, by averaging the quantum mechanical propagator over classical trajectories (the details of the theory are outlined in Sec. 6.3 below). $\tau_B$ and $\tau_{\mathrm{so}}$ thus depend not only on microscopic parameters (magnetic field $B$ and SOI strength, respectively), but through the average over trajectories also on dimensionality, confinement, and $l_e$. We

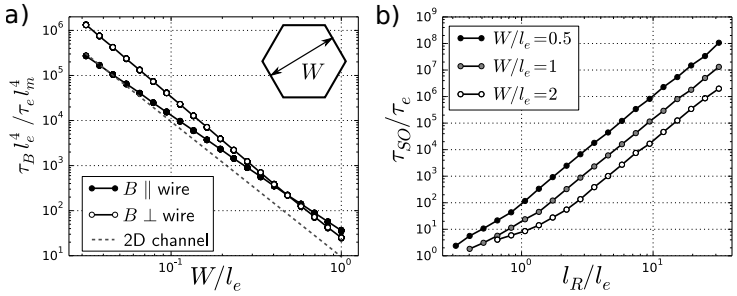


**Figure 6.2:** (a) Normalized dephasing time $\tau_B {l_e}^4/\tau_e {l_m}^4$ as a function of $W/l_e$ for a hexagonal nanowire (see inset) for field parallel (black) and perpendicular (red) to the nanowire. Dots are numerical data for different $l_m$ in the range $1-10^{2.5}$ ($10-20$ points per $W$), solid lines a fit to Eq. (6.3). Dashed line is the 2D wire result of Ref. 25. (b) $\tau_{\rm so}/\tau_e$ as a function of spin-orbit strength $l_{\rm R}/l_e$ and different wire diameters in a 3D hexagonal nanowire.

focus on the case where Rashba SOI due to an effective electric field in the $z$-direction, perpendicular to wire and substrate, dominates. Then the microscopic SOI Hamiltonian is $\frac{\alpha_{\rm R}}{\hbar}(p_x\sigma_y - p_y\sigma_x)$, where $\sigma_{x,y}$ are Pauli matrices and $p_{x,y}$ the momentum operators. The corresponding spin-orbit precession length, $l_{\rm R}$, equals $\hbar^2/m^*\alpha_{\rm R}$. In our treatment we neglect the Zeeman splitting, $E_{\rm Z}$ since we concentrate on the regime of large Fermi wave vector, $k_{\rm F}$, such that $\alpha_{\rm R}k_{\rm F} \gg E_{\rm Z}$.

The quasiclassical description is valid if the Fermi wave length $\lambda_{\rm F} \ll l_e, l_{\rm R}$, and much smaller than the transverse extent $W$ of the nanowire, i.e. for many occupied subbands. In particular, the quasiclassical method remains valid even if $l_{\rm R} < l_e, W$.[185]

We evaluate $\tau_B$ and $\tau_{\rm so}$ numerically by averaging over random classical paths for a given nanowire geometry. The paths consist of piece-wise linear segments of freely moving electrons with constant speed,[26,37] only scattered randomly from impurities and specularly at the boundary. These assumptions imply a uniform electron density in the nanowire. Specular boundary reflection is expected as our wires have no surface roughness.[181] (We extrapolate the results on InAsSb wires to InSb since the flatness of the facets results from the introduction of Sb.)

We apply our theory to nanowires with a hexagonal cross-section and diameter $W$ (see inset in Fig. 6.2a) in the quasi-ballistic regime, $l_e \gtrsim W$. Fig. 6.2(a) shows the magnetic dephasing time $\tau_B$ (normalized by $\tau_e l_m^4/l_e^4$ with $l_m = \sqrt{\hbar/eB}$) as a function of wire diameter. Both parallel and perpendicular field give rise to magnetic dephasing due

to the three-dimensionality of the electron paths, in contrast to two-dimensional systems where only a perpendicular field is relevant (see Fig. 6.1). The different field directions show a different dependence on $W$, with, remarkably, $\tau_B$ (and thus $l_B$) independent of field-orientation for $W/l_e = 0.5$. Our results for $\tau_{\mathrm{so}}$ as a function of $l_{\mathrm{R}}$ are shown in Fig. 6.2b. We find an increase of $\tau_{\mathrm{so}}$ as the wire diameter $W$ is decreased, indicating that confinement leads to increased spin relaxation times.

For $l_{m,\mathrm{R}}, l_e \gtrsim W$ we can fit our results reliably as

$$\tau_{B,\mathrm{so}} = C \frac{l_{m,\mathrm{R}}^4}{W^\gamma l_e^{(4-\gamma)}}. \tag{6.3}$$

This is shown for $\tau_B$ in Fig. 6.2a where data for different $l_m$ and $W$ collapse to one line. In particular for $\tau_B$, we find $C = 34.1 \pm 0.1$ and $\gamma = 2.590 \pm 0.002$ for parallel field, $C = 22.3 \pm 0.3$ and $\gamma = 3.174 \pm 0.003$ for perpendicular field. For $\tau_{\mathrm{so}}$ $C = 8.7 \pm 0.5$ and $\gamma = 3.2 \pm 0.1$. Note that our numerics is valid beyond the range where the fit (6.3) is applicable. For example, for $l_{\mathrm{R}} \lesssim W$ the numerical result deviates from the power-law of (6.3) as seen in Fig. 6.2b; in this regime only the numerical result can be used.

The fit (6.3) allows for a quantitative comparison of our 3D wire results to 2D wires: Both are similar in that there is flux cancellation ($\gamma > 2$)[25] and suppressed spin relaxation due to confinement. However, they exhibit a significantly different power-law. As an example, in Fig. 6.2a we compare to the 2D wire result for weak fields from Ref. 25 ($C = 10.8$, $\gamma = 3$) that can differ by an order of magnitude from our results. This emphasizes the need for an accurate description of geometry for a quantitative analysis of WAL.

## 6.3 Evaluation of weak (anti-)localization in the quasiclassical theory

### 6.3.1 The quasiclassical theory

Within the quasiclassical formalism, the weak (anti-) localization correction $\Delta G$ is given as[26,37,106]

$$\Delta G = -\frac{2e^2}{\pi\hbar}\frac{D}{L}\int_0^\infty dt\, C(t)(1 - e^{-t/\tau_e}) e^{-t/\tau_\varphi} \langle \mathscr{M}_B(t) \rangle \langle \mathscr{M}_{\mathrm{so}}(t) \rangle \tag{6.4}$$

In this expression, $L$ is the length of the nanowire, $C(t) = (4\pi D t)^{-1/2}$ is the 1D return probability, $D = \frac{1}{d} v_F l_e$ the diffusion coefficient ($d = 3$ for the nanowires). $\langle \ldots \rangle$ denotes an average over all classical paths that close after time $t$. $\mathcal{M}_B$ is due to the orbital effect of the magnetic field and reads[37]

$$\mathcal{M}_B(t) = e^{i\phi(t)}, \text{ with } \phi(t) = \frac{2e}{\hbar} \int_{\boldsymbol{x}(0)}^{\boldsymbol{x}(t)} \boldsymbol{A} \cdot d\boldsymbol{l}\,. \tag{6.5}$$

The Hamiltonian of spin-orbit interaction (SOI) can in general be written as

$$H_{\mathrm{SOI}} = \boldsymbol{\sigma} \cdot \boldsymbol{B}_{\mathrm{so}}(\boldsymbol{p}) \tag{6.6}$$

where $\boldsymbol{\sigma}$ is a vector of Pauli matrices and $\boldsymbol{B}_{\mathrm{so}}$ a momentum-dependent effective magnetic field due to the SOI. In the case of Rashba SOI as considered here we have $\boldsymbol{B}_{\mathrm{so}}(\boldsymbol{p}) = \frac{\alpha_R}{\hbar}(-p_y, p_x, 0)$. The SOI of Eq. (6.6) then gives rise to the modulation factor[37,185]

$$\begin{aligned} \mathcal{M}_{\mathrm{so}}(t) &= \frac{1}{2}\mathrm{Tr}\left(W(t)^2\right) \\ W(t) &= \mathcal{T} \exp\left[\frac{i}{\hbar}\int_0^t dt' \boldsymbol{\sigma} \cdot \boldsymbol{B}_{\mathrm{so}}(\boldsymbol{p}(t))\right] \end{aligned} \tag{6.7}$$

where $\mathcal{T}$ is the time-order operator.

When the motion along the longitudinal direction of wire is diffusive, the modulation factors generally decay exponentially with time,[37]

$$\langle \mathcal{M}_B(t) \rangle = e^{-t/\tau_B}, \text{ and } \langle \mathcal{M}_{\mathrm{so}}(t) \rangle = \tfrac{3}{2} e^{-4t/3\tau_{\mathrm{so}}} - \tfrac{1}{2}\,. \tag{6.8}$$

Note that $\tau_B$ and $\tau_{\mathrm{so}}$ depend explicitly on the magnetic field $B$ and the SOI strength through equations (6.5) and (6.7), respectively. However, through the average over classical paths, $\langle \ldots \rangle$ they also depend on the geometry of the nanowire and the mean free path $l_e$.

With the exponential form of the modulation factors in Eq. (6.8) the integral in Eq. (6.4) can be performed to give Eq. (6.1)

*Requirements of the quasi-classical theory* The quasiclassical description is valid if the Fermi wave length $\lambda_F$ is much smaller than the typical transverse extent of the nanowire $W$, i.e. for many occupied subbands. It also requires that the classical paths are neither affected by magnetic field nor SOI: The former requires that the cyclotron

radius $\lambda_{\mathrm{cyc}} \gg W, l_e$,[26,37] the latter that the kinetic energy dominates over the spin-orbit energy so that $l_{\mathrm{R}} \gg \lambda_F$.[185] In particular, the quasiclassical method is valid also for $l_{\mathrm{R}} < l_e, W$. Additional requirements are $\tau_B, \tau_{\mathrm{so}} \gg \tau_e$, for the exponential decay of magnetic dephasing time (length) and spin relaxation time to be valid.[26,185] In addition we must have $l_\varphi \gg W$ to be in the quasi-one-dimensional limit, where the return probability $C(t)$ in Eq. (6.4) is given by the 1D return probability.

These are the fundamental requirements for the quasiclassical theory to hold. They should not confused with the stronger requirements $l_{m,\mathrm{R},e} \gtrsim W$ needed for the validity of the fit of Eq. (6.3)

*Experimental fulfillment of quasi-classical requirements* The experimental details validating the applicability of the quasiclassical technique follow later in this chapter. The number of occupied subbands is discussed in Sec. 6.4.4. As shown in Fig. 6.5c below, $l_\varphi$ largely exceeds the wire diameter for a large range of conductance, thereby obeying the requirement for a one-dimensional quantum interference model. The range of $B$ (up to 200 mT) in the fits in Figs. 6.5 and 6.6 in general obey $\tau_B \gtrsim \tau_e$. Alternatively, fitting over a smaller $B$-range (up to 75 – 100 mT, fulfilling $l_m \gtrsim W$, $\tau_e$ and $\lambda_{\mathrm{cyc}} \gg W, l_e$ to a larger extent) can be performed on MC traces showing WAL without WL at larger $B$ (observed when $G \geq 2e^2/h$) with fixed $\Delta G(B \to \infty)$, yielding the same results within $\sim 20\%$.

### 6.3.2 Monte Carlo evaluation

In order to obtain the decay times in Eq. (6.8) as a function of mean free path $l_e$, wire diameter $W$, and magnetic field $B$ or Rashba spin-orbit strength $\alpha_R$, we performed Monte-Carlo simulations of quasiclassical paths in a hexagonal nanowire, as has been described before in Refs. 26,37 and 185.

*Model and Boltzmannian ensemble* We model the nanowire as a three-dimensional prism of infinite length, with a regular hexagon as cross-section.

A Boltzmannian ensemble of quasiclassical paths is created, with each path consisting of propagation along a sequence of straight line segments with constant velocity. For each path, after certain intervals, the direction of the particles velocity is changed at random, with

isotropic distribution, corresponding to collision of randomly distributed pointlike impurities. The distance of free propagation between collision is determined at random, Poisson-distributed $P(l) \propto e^{-l/l_e}$, so that the mean-free path is $l_e$. On impact with one of the nanowires walls, reflection occurs in a specular fashion, by reversing the velocity component perpendicular to the wall. The resulting ensemble will consist of paths which are open (start and end point do not coincide).

*Evaluation of $\mathcal{M}_B$, $\mathcal{M}_{\mathrm{so}}$* After obtaining an ensemble of Boltzmannian paths, for each path the integrals Eq. (6.5) or Eq. (6.7) are evaluated. Because the paths consist of straight line segments, the evaluation is elementary for each segment, and the integrals $\mathcal{M}_B$, $\mathcal{M}_{\mathrm{so}}$ are the products of these segments. For $\mathcal{M}_B$, these are the phase factors $e^{i\phi_n}$ accumulated along each segment, while for $\mathcal{M}_{so}$ we must multiply unitary two-by-two matrices which describe the spin dynamics along each segment. When calculating $\mathcal{M}$ at the same time as generating the path, only the last position, velocity and accumulated product of $\mathcal{M}_{B,\mathrm{so}}(t)$ need to be kept in memory.

*Magnetic field* To be more specific, for magnetic fields we choose the field to point along the $y$ direction, and the nanowire to lie along either the $x$ or $y$ direction, so that the magnetic field is either perpendicular or parallel to the nanowires axis. In the perpendicular case, the orientation of the nanowire was either such that the magnetic field penetrated one of the faces perpendicularly, or such that it was parallel to one of the faces (the difference being a rotation by 30 degrees). It was established that for the resulting $\tau_B$ there is no significant difference between these two orientations in the relevant regime.

When choosing the gauge,

$$A(\boldsymbol{r}) = (Bz, 0, 0) \tag{6.9}$$

the generation of open paths is sufficient for the evaluation of $\mathcal{M}_B(t)$ according to Eq. (6.5), because the average $\langle \mathcal{M}_B(t) \rangle$ over open and closed paths is then identical.[25] Since open and closed paths are equivalent in this situation, we use open paths that are easier to generate numerically than closed paths. In our simulations, we chose an ensemble size of $2^{14}$ open paths to for averaging.

*Spin-orbit* For $\langle \mathscr{M}_{so} \rangle$ an evaluation with open paths is not possible, and we have to average over an ensemble of closed paths, which is created as described in the following. By creating a number $N$ of open paths of length $L/2$, we can create a set of $N(N-1)/2$ statistically independent open paths of length $L$, by pairwise concatenation of two different paths. We restrict this much larger set of paths to those which are almost closed (with start and end point separated not further than $l_e$), and then insert an additional line segment that closes these paths. If the concatenated paths are of sufficient length, we assume that the insertion of this additional line segment with a slightly different length distribution than the other line segments does not change the ensemble properties appreciably. Because we thus could only use a subset of the generated paths, we chose an ensemble size of $2^{16}$ open paths in this case. (The size of the ensemble of closed paths decreases with increasing $L$).

*Fitting decay times* Finally, after having created ensembles of open or closed paths as described above for a set of different path lengths, which we chose to be logarithmically spaced, $t_n = (1.1)^n \tau_e$ with $n$ integer and $1 \leq t_n/\tau_e \leq 10^6$, we determined the averages $\langle \mathscr{M}_{B,so}(t) \rangle$ and numerically fitted the exponential decays according to Eqs. (6.8), resulting in estimates for the decay times $\tau_B$ and $\tau_{so}$.

*Validating against known results: Square nanowire* To validate the results of our simulations for $\mathscr{M}_B$, we also simulate other geometries, in which results have been found previously, numerically or analytically. First, instead of considering hexagonal nanowires, we change the shape of the nanowire to be square. If a square nanowire is placed in a perpendicular magnetic field and has specularly reflecting walls, we expect the result to be the same as for a 2D layer, as treated in Ref. 25. This is because reflections on the walls perpendicular to $B$ do not change the projection of the path along the direction of $B$, and thus are ineffective.

We should thus reproduce the result of Ref. 25, which in the "clean, weak field" limit reads

$$\frac{\tau_B}{\tau_e} = 12.1 \frac{l_m^4}{W^3 l_e} \tag{6.10}$$

and should hold for $W \ll l_e$ and $l_m \gg \sqrt{W l_e}$. In the left frame of Fig. 6.3 we show simulation results for both perpendicular and parallel field

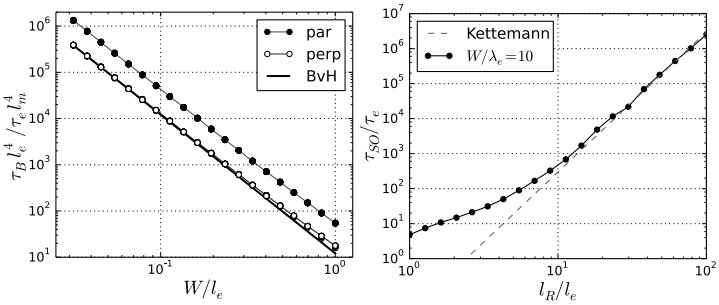


**Figure 6.3:** *Left:* Comparison to the analytical expression by Beenakker and van Houten.[25] Numerically obtained data points are shown for different magnetic field $l_e < l_m < 10^{1.5} l_e$, parallel ("par") and perpendicular ("perp") to the nanowire. The fact that points for different $l_m$ collapse shows the expected $l_m^4$ behavior. The black line "BvH" is the asymptotic expression Eq. (6.10) for $W \ll l_e$. For $W \simeq l_e$, a cross-over to the diffusive regime can be observed. *Right:* Comparison of the numerical evaluation of $\langle \mathscr{M}_{so} \rangle$ in a 2D strip (blue dots and line) and the diffusive result of Ref. 93 (dashed line). In the numerics, the width of the strip is $W = 10\ell_e$, so that motion is diffusive. The Cooperon-based treatment in Ref. 93 applies for $l_R > W$.

for a square nanowire. In perpendicular field, the data agrees to the analytical results in the regime of its validity (the onset of cross-over to the diffusive case can be seen). Remarkably, in parallel field, we also observe a $W^{-3}$ dependence, while for hexagonal geometry, the dependence on $W^{\gamma}$ has two different $\gamma$ for the two orientations.

*Validating against known results: Spin-orbit coupling in 2D strip* To check the calculations of $\mathscr{M}_{so}$, we compare our simulations to the expression for $\tau_{\mathrm{so}}$ for two-dimensional diffusive wires ($l_e \ll W$) with Rashba spin-orbit interaction from Kettemann.[93]

When comparing $\tau_{\mathrm{so}}$ between different sources it is important to note that different conventions for $\tau_{\mathrm{so}}$ exist (such as choosing a factor 4/3 in Eq. (6.8)). For consistency it is thus important to compare physical observables. For weak antilocalization this is the conductance correction. In order to describe the case of diffusive wires ($l_e \ll W$) we need to take the limit $l_e \to 0$ in Eq. (6.1):

$$\Delta G = -\frac{e^2}{h}\frac{\sqrt{D}}{L}\left[3\left(\frac{1}{\tau_\varphi} + \frac{4}{3\tau_{\mathrm{so}}} + \frac{1}{\tau_B}\right)^{-\frac{1}{2}} - \left(\frac{1}{\tau_\varphi} + \frac{1}{\tau_B}\right)^{-\frac{1}{2}}\right]. \tag{6.11}$$

Kettemann uses a Green's function based approach and arrives at:[93]

$$\Delta G = -\frac{e^2}{h}\frac{\sqrt{D}}{L}\left[2\left(\frac{1}{\tau_\varphi}+\frac{1}{2\tau_{\mathrm{so}}^*}+\frac{1}{\tau_B}\right)^{-\frac{1}{2}}+\left(\frac{1}{\tau_\varphi}+\frac{1}{\tau_{\mathrm{so}}^*}+\frac{1}{\tau_B}\right)^{-\frac{1}{2}}-\left(\frac{1}{\tau_\varphi}+\frac{1}{\tau_B}\right)^{-\frac{1}{2}}\right], \tag{6.12}$$

where $\tau_{\mathrm{so}}^*$ refers to the "$\tau_{\mathrm{so}}$" used in Ref. 93. In the limit of small spin-orbit splitting, $1/\tau_{\mathrm{so}} \to 0$, both expressions become equal if we identify

$$\tau_{\mathrm{so}} = 2\tau_{\mathrm{so}}^*. \tag{6.13}$$

Hence we need to take this factor of 2 into account when comparing our results to Kettemann's. Taking this factor into account, the expressions (6.11) and (6.12) not only agree for weak spin-orbit, but also never differ by more than 5% for all $\tau_{\mathrm{so}}$.

The right frame in Fig. 6.3 shows the comparison between the expression given in Ref. 93, which after conversion to the quantities used in this chapter is

$$\tau_{so}/\tau_e = 3l_R^4/W^2, \tag{6.14}$$

and numerical results we obtained for a diffusive 2D strip for different spin-orbit strengths.

## 6.4 Experiments

The experiments described below were performed in the QuTech lab and the Kavli Institute for Nanoscience in Delft, without direct involvement of the author of this thesis.

InSb nanowires[139] with diameter $W \approx 100\,\mathrm{nm}$ are deposited onto a substrate with a global back gate. A large ($\geq 2\,\mu\mathrm{m}$) contact separation ensures sufficient scattering between source and drain. After contact deposition a $HfO_2$ dielectric layer is deposited and the device is then covered by metal, creating an Ω-shaped top gate (Fig. 6.4a and insets of Fig. 6.4c-d). Nanowire conductance is controlled with top and back gate voltage, reaching a conductance up to $\sim 5e^2/h$ (Fig. 6.4b). The device design leads to a strong top gate coupling (Fig. 6.4c), while back gate coupling is weaker (Fig. 6.4d). From a field-effect mobility of $\sim 11{,}000\,\mathrm{cm}^2/\mathrm{Vs}$ a ratio of mean free path to wire diameter $l_e/W = 1-2$ is estimated[140], see Sec. 6.4.2.

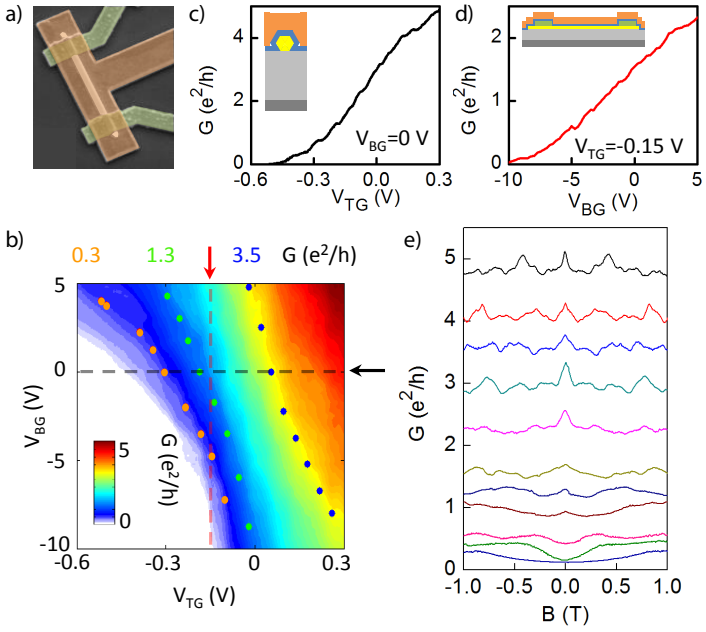


**Figure 6.4:** (a) False color scanning electron microscopy image of device I. Contact spacing is $2\mu$m. Device fabrication is described in Sec. 6.4.1 (b) Conductance $G$, as a function of top gate voltage, $V_{TG}$, and back gate voltage, $V_{BG}$. Arrows and dashed lines indicate cross sections shown in panels (c) and (d). Dots indicate voltages ($V_{BG}$,$V_{TG}$) at which traces in Fig. 6.5a were taken (same dot color corresponds to same $G$). Data taken with 10 mV voltage bias at a temperature of 4.2K. (c) $G$ as a function of $V_{TG}$ at $V_{BG} = 0$V. Inset: radial cross section of the device. The blue layer is $HfO_2$. (d) $G$ as a function of $V_{BG}$ at $V_{TG} = -0.15$V. Inset: axial cross section of the device. (e) Conductance, as a function of magnetic field at several values of device conductance controlled by $V_{TG}$, $V_{BG} = 0$V. Data taken with AC excitation $V_{AC} = 100\,\mu V_{RMS}$.

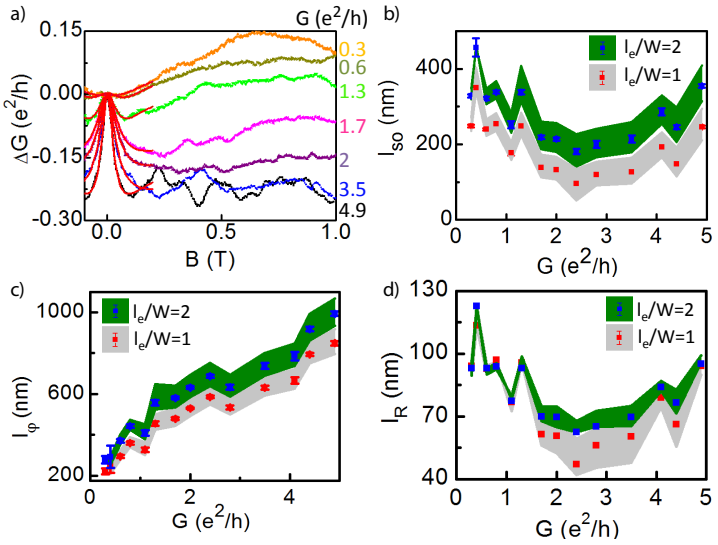


**Figure 6.5:** (a) Magnetoconductance (MC) obtained after averaging MC traces taken at the same $G$. For $G = 3.5, 1.3$ and $0.3e^2/h$ the voltages at which these MC traces were taken are indicated in Fig. 6.4b. Averaged MC traces have been centered to $\Delta G = 0$ at $B = 0$ T. $G$ ($B = 1$ T) is indicated on the right. Red curves are fits to the data assuming $\frac{l_e}{W} = 1$. (b) Spin relaxation length $l_{so}$ obtained from the fits of panel (a) ($\frac{l_e}{W} = 1$, blue points) and obtained from fits with $\frac{l_e}{W} = 2$ (red points). Standard deviation of the fit outcomes is indicated. The distribution around the blue and red points (green and gray bands, respectively) is given by the spin-orbit lengths obtained from fits with an effective width 15 nm smaller (resulting in longer $l_{so}$) or larger (resulting in shorter $l_{so}$) than the expected wire width $W = 90$ nm. (c) Phase coherence length, $l_\varphi$ and (d) spin precession length $l_R$ as a function of device conductance. Figure formatting is as in panel (b).

At large $G$ the magnetoconductance, measured with conductance controlled by the top gate at a temperature $T = 4.2$ K and with $B$ perpendicular to the nanowire and substrate plane, shows an increase of conductance of $\sim 0.2$ to $\sim 0.3\,e^2/h$ around $B = 0$ (Fig. 6.4e). $G(B)$ is, apart from reproducible conducantance fluctuations, flat at $B > 200$ mT, which is further evidence of specular boundary scattering.[26] On reducing conductance below $\sim 1.5\,e^2/h$ WAL becomes less pronounced and a crossover to WL is seen.

Reproducible conductance fluctuations, most clearly seen at larger $B$ (Fig. 6.4e), affect the WAL peak shape. To suppress these fluctuations several (7 – 11) MC traces are taken at the same device conductance (see Fig. 6.4b). After averaging these traces WAL remains while the

conductance fluctuations are greatly suppressed (Fig. 6.5a). Also here on reduction of conductance a crossover from WAL to WL is seen. Very similar results are obtained when averaging MC traces obtained as a function of top gate voltage with $V_{BG} = 0\,\mathrm{V}$. We expect that several ($\sim 10$) subbands are occupied at device conductance $G \gtrsim 2e^2/h$ (see estimation in Sec. 6.4.4). Hence, our quasiclassical approach is valid and we fit the averaged MC traces to Eq. (6.1) with $l_{\mathrm{so}}$, $l_\varphi$ and the conductance at large magnetic field $\Delta G(B \to \infty)$ as fit parameters. $l_{\mathrm{B}}$ is extracted from Eq. (6.3). Wire diameter and mean free path are fixed in each fit, but we extract fit results for a wire diameter deviating from its expected value and for both $\frac{l_e}{W} = 1$ and $\frac{l_e}{W} = 2$. We find good agreement between data and fits (see Fig. 6.5a). While showing fit results covering the full range of $G$, we base our conclusions on results obtained in the quasiclassical transport regime $G \gtrsim 2e^2/h$.

On increasing conductance, the spin relaxation length first decreases to $l_{\mathrm{so}} \approx 100 - 200\,\mathrm{nm}$, then increases again to $l_{\mathrm{so}} \approx 200 - 400\,\mathrm{nm}$ when $G \geq 2.5e^2/h$ (Fig. 6.5b). The phase coherence length (Fig. 6.5c) shows a monotonous increase with device conductance. This increase can be explained by the density dependence of either the diffusion constant or the electron-electron interaction strength,[115] often reported as the dominant source of dephasing in nanowires.[86,114]

Spin relaxation[180] in our device can possibly occur via the Elliot-Yafet[55,182] or the D'yakonov-Perel' mechanism,[53] corresponding to spin randomization at or in between scattering events, respectively. The Elliot-Yafet contribution can be estimated as[39]

$$l_{\mathrm{so,EY}} = \sqrt{\frac{3}{8}}\frac{E_G}{E_F} l_e \frac{(E_G + \Delta_{\mathrm{SO}})(3E_G + 2\Delta_{\mathrm{SO}})}{\Delta_{\mathrm{SO}}(2E_G + \Delta_{\mathrm{SO}})} \geq 300 - 600\,\mathrm{nm}, \qquad (6.15)$$

with band gap $E_G = 0.24\,\mathrm{eV}$, Fermi energy $E_F \leq 100\,\mathrm{meV}$, spin-orbit gap $\Delta_{\mathrm{SO}} = 0.8\,\mathrm{eV}$ and $\frac{l_e}{W} = 1 - 2$. For the D'yakonov-Perel' mechanism, we note that our nanowires have a zinc-blende crystal structure, grown in the [111] direction, where Dresselhaus SOI is absent for momentum along the nanowire.* We therefore expect that Rashba SOI is the dominant source of spin relaxation, in agreement with previous experiments.[129] As found in our theoretical analysis, it is then crucial to

*Furthermore, even for [100] nanowires Dresselhaus SOI is weak: In this case the maximum linear Dresselhaus SOI strength is $\gamma k_F^2$ (with $\gamma$ the cubic Dresselhaus SOI strength), yielding a spin-orbit length $l_{\mathrm{D}} = \hbar^2/m^*\gamma k_F^2$. With $\gamma = 437\,\mathrm{eV\,\AA^3}$[58] and $E_F \leq 100\,\mathrm{meV}$ we estimate $l_{\mathrm{D}} > 300\,\mathrm{nm}$.

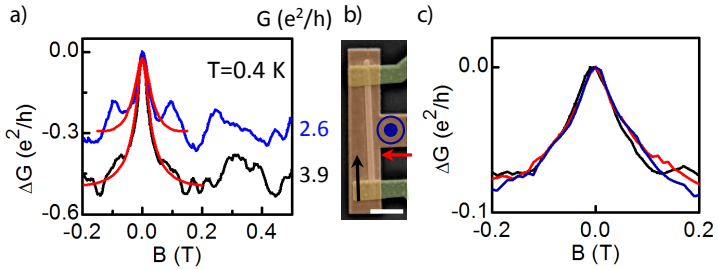


**Figure 6.6:** (a) Magnetoconductance (MC) at $T = 0.4\,\mathrm{K}$. Each MC trace is obtained after averaging 21 MC traces taken along the top-gate controlled pinch-off trace shown in Fig. 6.4c ($V_{BG} = 0\,\mathrm{V}$). Black (blue) trace is the average of traces taken between $V_{TG} = 0.34\,\mathrm{V}$ and $V_{TG} = 0.14\,\mathrm{V}$ ($V_{TG} = 0.12\,\mathrm{V}$ and $V_{TG} = -0.08\,\mathrm{V}$) with steps of 20 mV. The voltage excitation $V_{AC}$ was $10\,\mu V_{RMS}$. $G(B = 0.5\,\mathrm{T})$ is indicated on the right. Phase coherence and spin relaxation length obtained from fits (in red) to the traces is $1078 \pm 32\,(1174 \pm 39)\,\mathrm{nm}$ and of $95 \pm 18 (205 \pm 16)\,\mathrm{nm}$ respectively for $\frac{l_e}{W} = 1\,(2)$. Values obtained at $G = 2.6e^2/h$ are given below. (b) False color scanning electron microscope image of device II with different magnetic field orientations indicated by the arrows. Scale bar is $1\,\mu\mathrm{m}$. (c) MC obtained with $B$ parallel to the nanowire (in-plane angle w.r.t. nanowire $\theta \approx 5°$, black), $B$ perpendicular to the nanowire in the plane of the substrate ($\theta \approx 95°$, red) and $B$ perpendicular to the substrate plane (blue). $V_{TG} = 0.2\,\mathrm{V}$, $V_{BG} = 0\,\mathrm{V}$. Smaller $\Delta G$ compared to the preceding data is due to a larger contact resistance ($\sim 10\,\mathrm{k}\Omega$) of this device for which no correction was made.

capture confinement effects accurately. Our $l_{\mathrm{so}}$ correspond to $\frac{\tau_{\mathrm{so}}}{\tau_e} = 2 - 15$ that are captured well by our simulations.*

Given that $W \approx l_{\mathrm{R}}$, we extract the $l_R$ corresponding to our $\frac{\tau_{\mathrm{so}}}{\tau_e}$ directly from Fig. 6.2b. We extract spin precession lengths $l_{\mathrm{R}}$ of $50 - 100\,\mathrm{nm}$, shown in Fig. 6.5d, corresponding to $\alpha_{\mathrm{R}} = 0.5 - 1.0\,\mathrm{eV\,\mathring{A}}$. MC measurements on a second device show very similar $l_{\mathrm{R}}$, see Fig. 6.15.

To confirm the interpretation of our MC measurements we extract MC at a lower temperature $T = 0.4\,\mathrm{K}$ (Fig. 6.6a). We find larger WAL amplitudes of up to $\Delta G \sim 0.5e^2/h$, while the width of the WAL peak remains approximately the same as at $T = 4.2\,\mathrm{K}$, corresponding to a longer $l_\varphi$ at lower temperature, with approximately constant $l_{\mathrm{so}}$. A longer $l_\varphi$ is expected at lower temperature, as the rate of inelastic scattering, responsible for loss of phase coherence, is reduced in this regime.

Our theoretical analysis found similar dephasing times for magnetic fields perpendicular and parallel to the nanowire for our estimated

*Exceptions are the smallest values of $l_{\mathrm{so}}$ at $G = 2.4$ and $2.8e^2/h$: When assuming a wire width larger than the expected value ($W = 105\,\mathrm{nm}$) we find $\frac{\tau_{\mathrm{so}}}{\tau_e} \sim 1$. In this case the $l_{\mathrm{R}}$ corresponding to the lowest simulated value of $\frac{\tau_{\mathrm{so}}}{\tau_e}$ have been chosen as a lower bound.

mean free paths, $l_e/W = 1-2$. Indeed, we observe virtually identical WAL for fields parallel and perpendicular to the nanowire in our second device (see Figs. 6.6b-c). WAL in the first device is also very similar for both field directions, see Fig. 6.13. This is in striking contrast to MC measurements in two-dimensional systems where only a perpendicular magnetic field gives strong dephasing due to orbital effects. It also provides strong support for the assumptions made in our theory, and emphasizes the importance of including the three-dimensional nature of nanowires to understand their MC properties. In contrast, WL is anisotropic, which we attribute to a different density distribution at low conductance compared to the high conductance at which WAL is seen.

Relevant to Majorana fermion experiments is the spin-orbit energy, $E_{\mathrm{SO}} = \frac{m\alpha_{\mathrm{R}}^2}{2\hbar^2}$, that is $0.25-1\,\mathrm{meV}$ in our devices. These values compare favorably to InAs nanowires that yield $\alpha_{\mathrm{R}}^{\mathrm{InAs}} = 0.1-0.3\,\mathrm{eV\,\AA}$ [47,57,73,114,147] and corresponding $E_{\mathrm{SO}}^{\mathrm{InAs}} = 15-135\,\mu\mathrm{eV}$. $E_{\mathrm{SO}}^{\mathrm{InSb}}$ is similar or slightly larger than reported spin-orbit energies in Ge/Si core-shell nanowires ($E_{\mathrm{SO}}^{\mathrm{Ge/Si}} = 90-600\,\mu\mathrm{eV}$ [74,77]), while $\alpha_{\mathrm{R}}^{\mathrm{InSb}}$ is larger than $\alpha_{\mathrm{R}}^{\mathrm{Ge/Si}} = 0.07-0.18\,\mathrm{eV\,\AA}$. Note that the device geometries and expressions for $\alpha_{\mathrm{R}}(l_{\mathrm{so}})$ used by different authors vary and that often only $l_{\mathrm{so}}$, not $l_{\mathrm{R}}$ is evaluated. With our $E_{\mathrm{SO}}$ we then find, following the analysis of Ref. 154, a topological gap of $\sim 0.1-1\mathrm{K}$ (details in Sec 6.4.5) even for our moderate mobilities of order $10000\,\mathrm{cm^2/Vs}$. This gap largely exceeds the temperature and previous estimates. Hence, our findings underline the potential of InSb nanowires in the study of Majorana fermions.

### 6.4.1 Device fabrication

The nanowire is deposited onto a $p^{++}$-doped Si substrate covered by 285 nm $SiO_2$ (depicted in black in Fig. 6.4a). Contacts to the nanowire (green) are made by a lift-off process using electron beam lithography. Contact material is Ti/Au (25/125 nm). After passivation of the nanowire with a diluted ammoniumpolysulfur solution (concentration $(NH_4)S_X$:$H_2O$ 1:200) the chip is covered with $HfO_2$ (30 nm), deposited by atomic layer deposition. The dielectric is removed at the bonding pads by the writing of an etch mask (PMMA) followed by an HF etch. A top gate (brown) is deposited using a lift-off process with electron beam lithography. Top gate is defined using Ti/Au (25/175 nm). Lastly, an additional layer of Ti/Pt (5/50 nm) is deposited on the bond pads to

reduce the chance of leakage to the global back gate. Devices were only imaged optically during device fabrication. SEM imaging was performed only after the measurements.

### 6.4.2 Estimation of mobility, mean free path and $\frac{l_e}{W}$

Nanowire mobility, $\mu$, is obtained from pinch-off traces using the method described in section 3 of the Supplementary Material of Ref. 140. In short, mobility is obtained from the change of current, or conductance, with gate voltage. We thus extract field-effect mobility, whereby we rely on a fit of the gate trace to an expression for gate-induced transport. This expression includes a fixed resistance in series with the gated nanowire. To extract mobility and series resistances from device I (data shown in Fig. 6.4–6.6a as well as Fig. 6.7, Fig. 6.11, Fig. 6.12, Fig. 6.13, Fig. 6.14) in this way, a gate trace from pinch-off to saturation is needed. However, $I(V_{BG}, V_{TG} = 0\,\mathrm{V})$ obtained from Fig. 6.7a covers only an intermediate range (see 6.7b). Therefore traces at $I(V_{BG}$, $V_{TG} = -0.15,\mathrm{V})$ and $I(V_{BG}$, $V_{TG} = 0.15\,\mathrm{V})$, shown in Fig. 6.7b are also used. The three traces then together form a full pinch-off trace (see Fig. 6.7c) that is well approximated by Eq. (11) in Ref. 140, for which here an equivalent expression for current $I$ instead of conductance $G$ was used. Here the capacitance between back gate and nanowire $C_{BG} = 22\,\mathrm{aF}$, the series resistance $R_S = 10\,\mathrm{k\Omega}$, the mobility $\mu = 12{,}500\,\mathrm{cm^2/Vs}$ and the threshold voltage $V_{TG} = -16.5\,\mathrm{V}$ (see Fig. 6.7c). Other inputs are source-drain bias $V_{SD} = 10\,\mathrm{mV}$ and contact spacing $L = 2\,\mu\mathrm{m}$. The capacitance has been obtained from electrostatic simulations in which the hexagonal shape of the nanowire has been taken into account. The series resistance $R_S$ consists of instrumental resistances (RC-filters and ammeter impedance, together $8\,\mathrm{k\Omega}$) and a contact resistance $R_C$. The experimental pinch-off traces are best approximated by $R_C = 2\,\mathrm{k\Omega}$. Expressions for $I(V_{BG})$ with $R_C = 1\,\mathrm{k\Omega}$ and $R_C = 3\,\mathrm{k\Omega}$, also shown in Fig. 6.7c, deviate from the measured pinch-off traces. Mobility is also estimated from a linear fit to the top gate pinch-off trace shown in Fig. 6.7d. Prior to this fit instrumental and series resistances have been subtracted. From the fit $\mu \sim 9{,}000\,\mathrm{cm^2/Vs}$ is obtained, using $C_{TG} = 1440\,\mathrm{aF}$, obtained from electrostatic simulations, and $L = 2\,\mu\mathrm{m}$. Similarly, mobility in device III (see Fig. 6.7e, magnetoconductance data shown in Fig. 6.15 is extracted from a fit to the top gate pinch-off trace, giving $\mu \sim 10000\,\mathrm{cm^2/Vs}$ using $C_{TG} = 1660\,\mathrm{aF}$ and $L = 2.3\,\mu\mathrm{m}$. These mobilities are similar to those

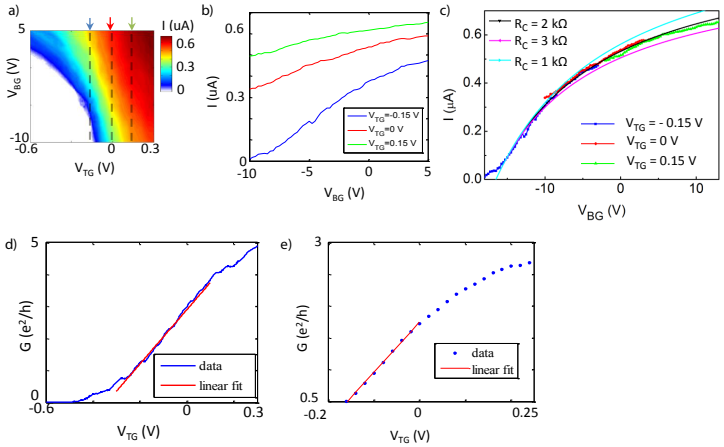


**Figure 6.7:** (a) Current, $I$, in device I as a function of top gate voltage, $V_{TG}$, and back gate voltage, $V_{BG}$. Cross sections corresponding to the $I(V_{BG})$ traces in panel b are indicated with arrows. Data taken with source-drain voltage $V_{SD} = 10\,\mathrm{mV}$. (b) $I(V_{BG})$ at $V_{TG} = 0.15\,\mathrm{V}$, $V_{TG} = 0\,\mathrm{V}$ and $V_{TG} = -0.15V$. (c) Traces at $I(V_{BG}, V_{TG} = -0.15\,\mathrm{V})$ (blue) and $I(V_{BG}, V_{TG} = 0.15\,\mathrm{V})$ (green) are displaced by $\Delta V_{BG} = -8\,\mathrm{V}$ and $\Delta V_{BG} = 8\,\mathrm{V}$, respectively, chosen such that their current is similar to that of the $I(V_{BG}, V_{TG} = 0\,\mathrm{V})$ trace (red). Data is well approximated by $I(V_{BG})$ (see text) with mobility $\mu \sim 12{,}500\,\mathrm{cm}^2/\mathrm{Vs}$ and contact resistance $R_C = 2\,\mathrm{k\Omega}$ (black). Traces with larger ($3\,\mathrm{k\Omega}$, pink) or smaller ($1\,\mathrm{k\Omega}$, cyan) contact resistance are also shown. (d) $G(V_{TG})$ in device I with $V_{BG} = 0\,\mathrm{V}$ (blue). A linear fit of the pinch-off traces (red) gives a slope $\frac{dG}{dV_{TG}} = 8.5(e^2/h)/\mathrm{V}$. (e) $G(V_{TG})$ in device III with $V_{BG} = 0\,\mathrm{V}$. A linear fit of the pinch-off traces (red) gives a slope $\frac{dG}{dV_{TG}} = 7.9(e^2/h)/\mathrm{V}$.

obtained in InSb nanowires that are gated using only a global back gate.[140] Mean free path, $l_e$, is estimated as $l_e = v_F \tau_e$, with $v_F$ the Fermi velocity and $\tau_e$ the scattering time. $\tau_e = \frac{\mu m^*}{e}$, with $e$ electron charge and $m^*$ the effective electron mass in InSb. Assuming a 3D density of states $v_F = \frac{\hbar}{m^*}(3\pi^2 n)^{\frac{1}{3}}$ with $\hbar$ the reduced Planck constant and $n$ electron density, $n$ is estimated from pinch off traces using $n = \frac{C(V_G - V_{TH})}{eAL}$ with $A$ the nanowire cross section, $V_G$ top or back gate voltage and $V_{TH}$ the threshold (pinch-off) voltage. In this way in device I $n$ up to $\sim 4 \cdot 10^{17}\,\mathrm{cm}^{-3}$ are obtained, giving $l_e$ up to $\sim 160\,\mathrm{nm}$. This estimate of $n$ agrees reasonably with densities obtained from a Schrödinger-Poisson solver (see Subsec. 6.4.4). In device III $n$ up to $\sim 4 \cdot 10^{17}\,\mathrm{cm}^{-3}$ gives $l_e \sim 150\,\mathrm{nm}$. Together with the facet-to-facet width $W$ (described in Fig. 6.8) these mean free paths yield a ratio $\frac{l_e}{W} = 1 - 2$.

### 6.4.3 Nanowire width

Nanowires were not imaged with scanning electron microscope prior to device fabrication to avoid damage due to electron irradiation. The wire diameter is estimated from a comparison of the nanowire width after fabrication to the nanowire diameter obtained from a number of wires from the same growth batch deposited on a substrate as described in Fig. 6.8.

### 6.4.4 Estimation of the number of occupied subbands

An estimate of the number of occupied subbands is calculated in two ways:

1. A self-consistent Schrodinger-Poisson calculation yields that 17 subbands contribute to transport at higher device conductance (density profile shown in the inset of Fig. 6.9). As contact screening has been neglected in these two-dimensional calculations the actual number of subbands may be slightly lower, but likely several ($\sim 10$) modes contribute at high device conductance.

2. The conductance, $G$, of a disordered quantum wire relates to the number of subbands, $N$, as[20]

$$G = \frac{NG_0}{1 + \frac{L}{l_e}}, \tag{6.16}$$

   which, using $\frac{L}{l_e} \approx 10 - 20$ (obtained from the estimate of $l_e$ above) yields $N \geq 25$.

### 6.4.5 Topological gap as a function of mobility and spin-orbit strength

We follow the theoretical analysis of Ref. 154 to compute the maximum topological gap that can be achieved at a given mobility $\mu$ and spin-orbit strength $\alpha_{\mathrm{R}}$. One should only be careful to note that the definition of $E_{\mathrm{SO}}$ in Ref. 154 differs by a factor of 4 from ours. Whenever we refer to $E_{\mathrm{SO}}$ here, we use our definition given in Sec. 6.4.

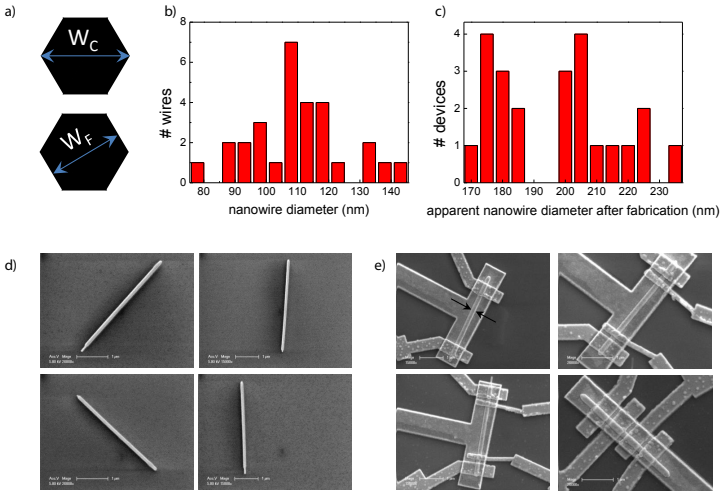


**Figure 6.8:** (a) Cross-sectional view of hexagonal nanowires with indicated widths $W_C$ and $W_F$. A top view of these nanowires (such as a scanning electron microscope image) shows the width from corner to corner, $W_C$. In our simulations of electron interference in hexagonal nanowires the facet-to-facet width, $W_F$, is used. The two widths are related by $W_F = \cos(\frac{\pi}{6})W_C$. (b) Distribution of nanowire diameters obtained from scanning electron microscope images of nanowires lying on a substrate. The imaged nanowires are from the same growth batch as the ones used in the experiment. The nanowire diameter is the width of the nanowire when lying on a substrate and thus corresponds to $W_C$ in panel a plus twice the native oxide thickness. Four imaged wires are shown in panel d. Average diameter is 110 nm, standard deviation is 15 nm. (c) Distribution of the apparent nanowire diameter after device fabrication. The distribution has been obtained from scanning electron microscope images of devices made in the same fabrication run (and thus with the same fabrication recipe) as the ones measured. The apparent diameter increases due to $HfO_2$ and top gate metal deposition. Average apparent diameter is 197 nm. Device I had an apparent diameter after fabrication of 200 nm, close to the average apparent nanowire device diameter, and therefore its wire diameter is estimated as 110 nm, the average the distribution of wire diameters in panel c. Device III has a diameter after fabrication of 180 nm, which is 17 nm below average. Wire diameter is therefore estimated as $110-17 = 93$ nm. Wires are covered by a native oxide of $\sim 2.5$ nm, giving an InSb diameter $W_C \approx 105$ nm and $W_C \approx 88$ nm for device I and device III respectively. Facet-to-facet diameter $W_F$, simply denoted by $W$ in the previous sections, is therefore $W \approx 90$ nm (device I) and $W_F = W \approx 75$ nm (device III). The standard deviation of wire diameter of 15 nm in panel b is used to define a range of wire diameters, $W \pm 15$ nm, for which spin relaxation length, spin precession length and phase coherence length are obtained in Fig. 6.5. (d) Scanning electron microscope image of four of the nanowires used to obtain the histogram of nanowire diameters of panel b. (e)Scanning electron microscope image of four of the devices imaged to obtain the apparent nanowire diameter after fabrication of panel c. The arrows in the upper left image indicate the apparent nanowire diameter.

In Fig. 6.10a we show the topological gap as a function of mobility for the spin-orbit energies estimated in the main text, with parameters suitable for the Majorana experiments in Ref. 128 We observe a nearly linear dependence of the topological gap on mobility for these parameters.

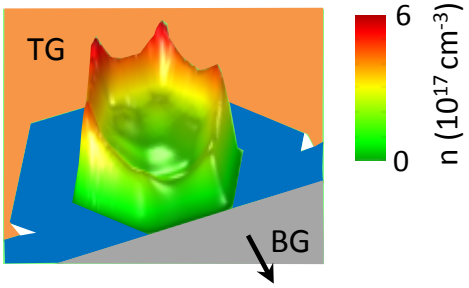


**Figure 6.9:** Electron density as a function of the nanowire cross section. Density is obtained from self-consistent Schrodinger-Poisson calculations with $V_{TG} = 0.5\,\mathrm{V}$ and $V_{BG} = 0\,\mathrm{V}$. TG (BG) denotes top (back) gate.

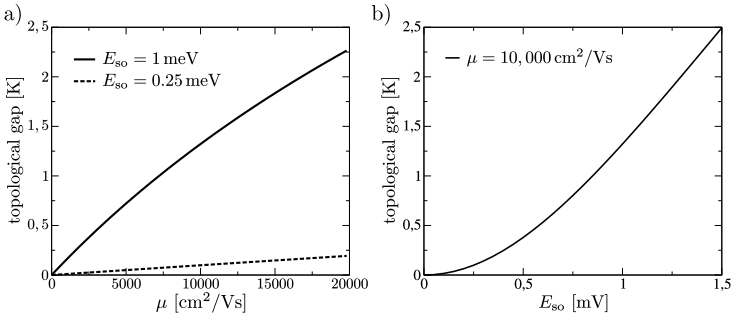


**Figure 6.10:** (a) Topological gap as a function of mobility for different values of $E_{so}$. (b) Topological gap as a function of $E_{so}$ for a fixed mobility of $10000\,\mathrm{cm}^2/\mathrm{Vs}$. The remaining parameters were chosen to be suitable for InSb nanowires in proximity to NbTiN: effective mass $m^* = 0.014\,m_e$ and superconducting gap $\Delta = 30\,\mathrm{K}$.

The topological gap can be rather sizable, and we find gaps of order 1 K for a moderate mobility of $\mu = 10{,}000\,\mathrm{cm}^2/\mathrm{Vs}$ for $E_{\mathrm{so}} = 1\,\mathrm{meV}$. From the figure it is also apparent that the topological gap depends rather strongly on $E_{\mathrm{so}}$.

We investigate the $E_{\mathrm{so}}$-dependence of the topological gap in Fig. 6.10b. At a mobility of $10{,}000\,\mathrm{cm}^2/\mathrm{Vs}$ the topological gap depends roughly quadratically on $E_{\mathrm{so}}$ up to $E_{\mathrm{so}} \sim 1\,\mathrm{meV}$, i.e. the topological gap increases as $\alpha_R^4$. This is in stark contrast to the clean case where the topological gap depends linearly on $\alpha_R$.

The different dependences of the topological gap on mobility (linear) and spin-orbit strength (to the fourth power) indicates that for current devices it may be more efficient to attempt to improve spin-orbit strength rather than mobility.

## 6.5 Supplementary experimental data

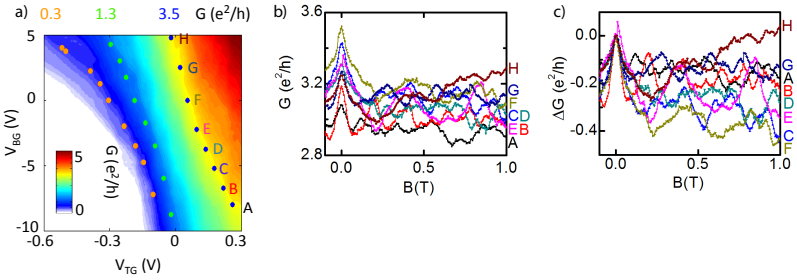


**Figure 6.11: Magnetoconductance traces at constant conductance.** (a) Conductance $G$, as a function of top gate voltage, $V_{TG}$, and back gate voltage, $V_{BG}$ as shown in Fig. 6.4b. Dots indicate voltages ($V_{BG}$,$V_{TG}$) at which traces in Fig. 6.5a were taken (same dot color corresponds to same G). The letters at the dots at $G = 3.5e^2/h$ refer to the magnetoconductance traces shown in panels b and c. Data obtained with 10 mV voltage bias at a temperature of 4.2 K. (b) Magnetoconductance traces taken at the points at $G = 3.5e^2/h$ shown in panel b. Data taken with AC excitation $V_{AC} = 100\,\mu\mathrm{V}_{RMS}$. The difference between the conductance of the dots in panel a and the conductance of the corresponding magnetoconductance traces in panel b is likely due to the difference in source-drain bias between both measurements. Also at other conductances (for instance at the green and orange dots in panel a) magnetoconductance traces generally show a conductance lower than those obtained in the gate-gate plot of panel a by a similar amount. For each of these traces the conductance denoted on the vertical axis of Fig. 4a and that on the horizontal axis of Fig. 4b-d is the conductance of the equiconductance points of Fig. 6.4b. (c) Magnetoconductance traces of panel b normalized to $\Delta G(B = 0) = 0$. By averaging over these traces the blue trace of Fig. 6.5a ($G = 3.5e^2/h$) is obtained.

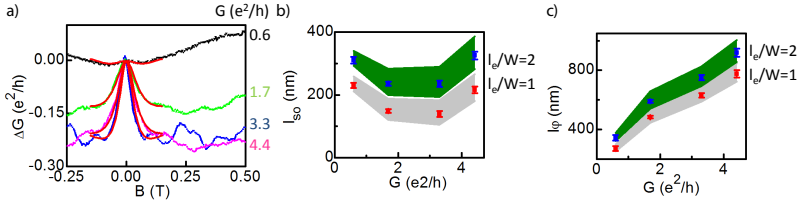


**Figure 6.12: Spin relaxation and phase coherence length obtained from top gate averaging in device I** (a) Magnetoconductance traces obtained after taking MC traces with top gate voltage spacing $\Delta V_{TG} = 20\,\mathrm{mV}$ between $V_{TG} = 0.34\,\mathrm{V}$ and $V_{TG} = -0.42\,\mathrm{V}$ and averaging 9 subsequent traces. $V_{BG} = 0\,\mathrm{V}$. Averaged MC traces have been centered to $\Delta G = 0$ at $B = 0\,\mathrm{T}$. $G(B = 0.5\,\mathrm{T})$ is indicated on the right. Red curves are fits to Eq. (6.1), wherein Eqs. (6.2) and (6.3) have been used to obtain $l_B$, using $l_e/W = 2$ and $W = 90\,\mathrm{nm}$. (b) Spin relaxation length, $l_{so}$, obtained from the fits of panel a ($\frac{l_e}{W} = 2$, red points) and obtained from fits with $\frac{l_e}{W} = 1$ (blue points). Standard deviation of the fit outcomes are indicated. The distribution around the blue and red points (in green and gray, respectively) is given by the spin-orbit lengths obtained from fits with an effective width 15 nm smaller or larger than the expected wire width $W = 90\,\mathrm{nm}$. (c) Phase coherence length, $l_\varphi$, obtained from fits of panel a. Figure formatting (colors, standard deviation and wire diameter dependence) is the same as in panel b.

| $(e^2/h)$ | $\frac{l_e}{W}$ | $l_{so}$ (nm) | $l_\varphi$ (nm) |
|---|---|---|---|
| 3.9 | 1 | $95 \pm 18$ | $1078 \pm 32$ |
| | 2 | $205 \pm 16$ | $1174 \pm 39$ |
| 2.6 | 1 | $171 \pm 26$ | $805 \pm 52$ |
| | 2 | $380 \pm 29$ | $937 \pm 60$ |

**Table 6.1: Phase coherence and spin relaxation length at $T = 0.4K$.** Spin relaxation length, $l_{so}$, and phase coherence length, $l_\varphi$, obtained from fits to the traces in Fig. 6.5a. $\frac{l_e}{W}$ denotes the ratio of mean free path, $l_e$, to wire width, $W$.

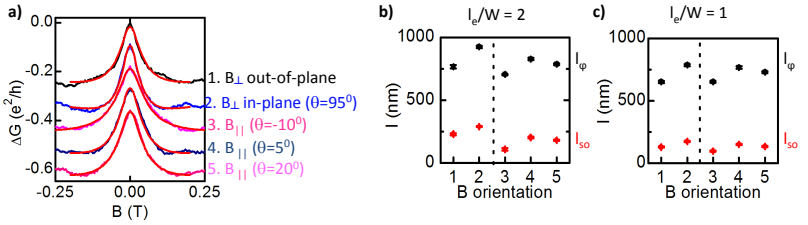


**Figure 6.13: Magnetoconductance in parallel and perpendicular field in device I.** (a) MC with parallel and perpendicular magnetic field orientation. Out-of-plane, $\perp$, (in-plane, $\parallel$,) denotes an orientation of the magnetic field (parallel) perpendicular to the substrate plane. $\theta$ denotes the in-plane angle of the magnetic field w.r.t. the nanowire. As the uncertainty in orientation of the in-plane magnetic field is 20° three parallel magnetoconductance traces with $|\theta| \leq 20°$ are shown. Each MC trace is an average of 7 traces taken at the same conductance $G = 3.5\,e^2/h$ by varying top and back gate voltage similar to the MC data of Fig. 6.2. No systematic change of MC along these equiconductance points was observed. As in device II (Fig. 6.6c) also here WAL in parallel and perpendicular magnetic field are very similar. Red curves are fits to Eq. (6.1) (in which Eqs. (6.2) and (6.3) have been used for $l_B$, with values of $C$ corresponding to parallel or perpendicular magnetic field orientation), using $\frac{l_e}{W} = 1$ and $W = 90\,\text{nm}$. (b) Spin relaxation length (red) and phase coherence length (black) obtained from fits of the MC traces in panel a using $\frac{l_e}{W} = 2$. B orientation numbers correspond to the traces numbered 1 to 5 in panel a. (c) Spin-orbit length (red) and phase coherence length (black) obtained from fits of the MC traces in a using $\frac{l_e}{W} = 1$. The slightly wider WAL peak in parallel magnetic field yields better agreement with $\frac{l_e}{W} = 1$ as spin-orbit lengths and phase coherence lengths obtained in parallel and perpendicular field with $\frac{l_e}{W} = 1$ are more similar than when assuming $\frac{l_e}{W} = 2$.

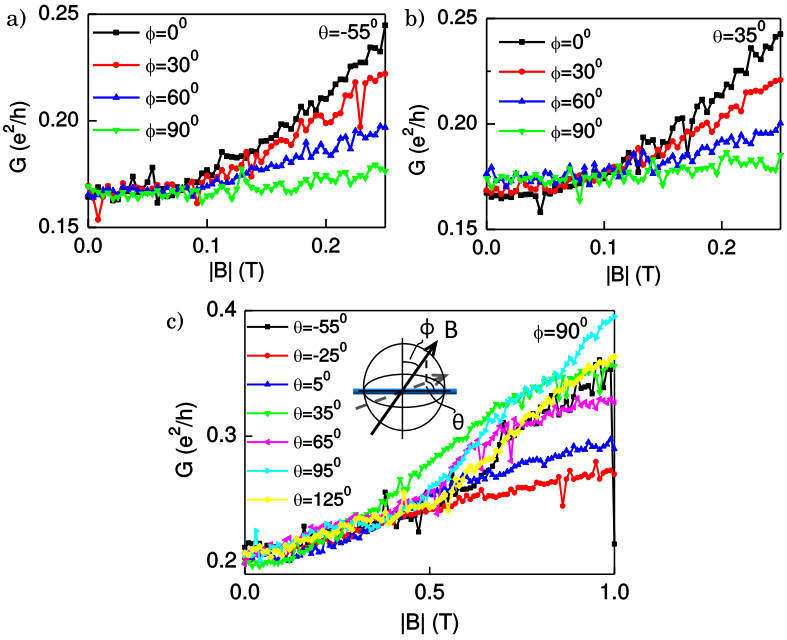


**Figure 6.14: Magnetoconductance for other angles of magnetic field in device I.** (a) MC as a function of out-of-plane angle, $\phi$, with in-plane angle w.r.t. the nanowire $\theta = -55 \pm 20°$. Angles $\theta$ and $\phi$ are shown in the schematic drawing in the inset of panel c. Out-of-plane (in-plane) denotes an orientation of the magnetic field (parallel) perpendicular to the substrate plane. $\phi = 0°$ (90°) is magnetic field perpendicular to (parallel to) the substrate plane. (b) MC as a function of out-of-plane angle $\phi$ with in-plane angle w.r.t. nanowire $\theta = 35 \pm 20°$. While weak anti-localization is (nearly) independent of magnetic field orientation, here we find that the suppression of weak localization by the magnetic field becomes less effective when rotating the field from perpendicular to parallel to the substrate plane. (c) MC as a function of in-plane angle $\theta$. Although the suppression of weak localization by magnetic field is much less effective for all magnetic fields oriented parallel to the substrate plane, a closer inspection shows that the magnetic field dependence is weakest when the magnetic field is approximately aligned with the nanowire. We suggest that the difference in dependence on magnetic field orientation between WAL and WL is due to a difference in charge distribution: while at the larger device conductance at which weak anti-localization is observed many subbands all across the nanowire cross section contribute to transport (see the inset of Fig. 6.2d), at low conductance, when weak localization is seen, transport takes place only a few modes, confined to a small region of the nanowire cross section. The low conductance situation may resemble a two-dimensional system, in which only the magnetic field component perpendicular to the substrate leads to a suppression of WL. This would lead to the reduction of positive MC when rotating the magnetic field from out-of-plane to in-plane. In all panels $V_{TG} = -0.36$V, $V_{BG} = 0$V. The difference in $G(B = 0\text{T})$ between panels a-b and c is due to a slight device instability at low conductance or due to hysteresis when sweeping $V_{TG}$.

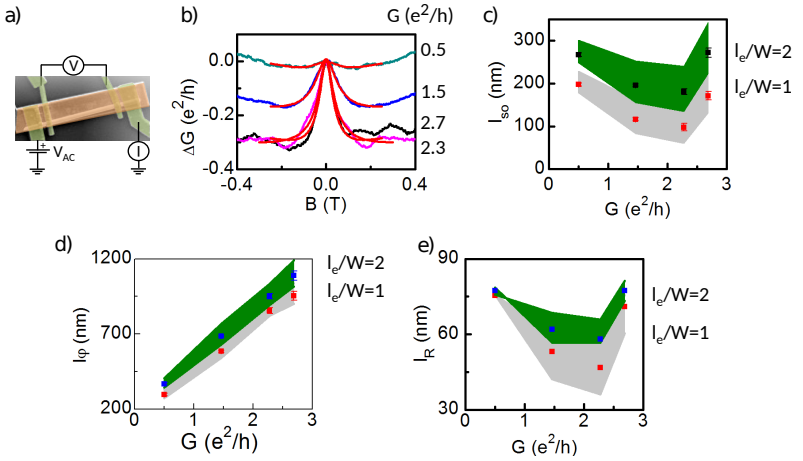


**Figure 6.15: Device III: Reproducibility of extracted spin relaxation and phase coherence length.** (a) False color scanning electron microscope image of device III. A voltage bias, $V_{AC}$, is applied across the outer contacts, after which simultaneously the current, $I$, through the device and the voltage across the inner contacts, $V$, is measured. Subsequently conductance $G = \frac{I}{V}$ is determined. (b) Averaged MC traces obtained after taking MC traces with top gate voltage spacing $\Delta V_{TG} = 20\,\mathrm{mV}$ between $V_{TG} = 0.3\,\mathrm{V}$ and $V_{TG} = -0.22\,\mathrm{V}$ and averaging 7 subsequent traces. $V_{BG} = 0\,\mathrm{V}$. $G(|B| = 0.5\,\mathrm{T})$ is indicated. Red curves are fits to Eq. (6.1), wherein Eqs. (6.2) and (6.3) have been used to obtain $l_B$, using $l_e/W = 1$ and $W = 75\,\mathrm{nm}$. (c) Spin relaxation length, $l_{so}$, obtained from the fits of panel b ($\frac{le}{W} = 1$, blue points) and obtained from fits with $\frac{le}{W} = 2$ (red points). Standard deviation of the fit outcomes is indicated. The distribution around the blue and red points (in green and gray, respectively) is given by the spin-orbit lengths obtained from fits with an effective width 15 nm smaller or larger than the expected wire width $W = 75\,\mathrm{nm}$. (d) Phase coherence length, $l_\varphi$, obtained from the fits of panel b ($\frac{le}{W} = 1$, blue points) and obtained from fits with $\frac{le}{W} = 2$ (red points). Figure formatting is the same as in panel c. (e) Spin precession length, $l_R$, as a function of device conductance, $G$, extracted from the spin relaxation lengths of panel c. Figure formatting is the same as in panel c. When assuming $W = 90\,\mathrm{nm}$ the $\frac{\tau_{so}}{\tau_e}$ corresponding to the $l_{so}$ at $G = 2.3e^2/h$ are below the simulation range. In this case the $l_R$ corresponding to the lowest simulated value of $\frac{\tau_{so}}{\tau_e}$ has been chosen.

# Bibliography


[1] M. Abramowitz and I. A. Stegun. *Handbook of Mathematical Functions*. Courier Corporation, 1964. ISBN 978-0-486-61272-0.

[2] Y. Aharonov, L. Davidovich, and N. Zagury. *Quantum random walks*. Phys. Rev. A **48**, 1687–1690, 1993.

[3] A. Ahlbrecht, V. B. Scholz, and A. H. Werner. *Disordered quantum walks in one lattice dimension*. J. Math. Phys. **52**, 102201, 2011.

[4] A. Ahlbrecht, H. Vogts, A. H. Werner, and R. F. Werner. *Asymptotic evolution of quantum walks with random coin*. J. Math. Phys. **52**, 042201, 2011.

[5] M. Aidelsburger, M. Atala, M. Lohse, J. T. Barreiro, B. Paredes, and I. Bloch. *Realization of the Hofstadter Hamiltonian with ultracold atoms in optical lattices*. Phys. Rev. Lett. **111**, 185301, 2013.

[6] A. R. Akhmerov, J. P. Dahlhaus, F. Hassler, M. Wimmer, and C. W. J. Beenakker. *Quantized conductance at the Majorana phase transition in a disordered superconducting wire*. Phys. Rev. Lett. **106**, 057001, 2011.

[7] J. Alicea. *New directions in the pursuit of Majorana fermions in solid state systems*. Rep. Prog. Phys. **75**, 076501, 2012.

[8] J. Alicea. *Exotic matter: Majorana modes materialize*. Nat. Nanotechnol. **8**, 623–624, 2013.

[9] A. Altland and M. R. Zirnbauer. *Nonstandard symmetry classes in mesoscopic normal-superconducting hybrid structures*. Phys. Rev. B **55**, 1142–1161, 1997.

[10] B. L. Al'tshuler, A. G. Aronov, A. I. Larkin, and D. E. Khmel'nitskii. *Anomalous magnetoresistance in semiconductors*. Sov. Phys. JETP **54**, 411, 1981.

[11] A. Ambainis, J. Kempe, and A. Rivosh. *Coins make quantum walks faster*. In *Proceedings of the Sixteenth Annual ACM-SIAM Symposium on Discrete Algorithms*, SODA '05, pp. 1099–1108. Society for Industrial and Applied Mathematics, Philadelphia, PA, USA, 2005. ISBN 978-0-89871-585-9.

[12] Y. Ando. *Topological insulator materials*. J. Phys. Soc. Jpn. **82**, 102001, 2013.

[13] J. K. Asbóth. *Symmetries, topological phases, and bound states in the one-dimensional quantum walk*. Phys. Rev. B **86**, 195414, 2012.

[14] J. K. Asbóth and H. Obuse. *Bulk-boundary correspondence for chiral symmetric quantum walks*. Phys. Rev. B **88**, 121406, 2013.

[15] J. K. Asbóth, B. Tarasinski, and P. Delplace. *Chiral symmetry and bulk-boundary correspondence in periodically driven one-dimensional systems*. Phys. Rev. B **90**, 125143, 2014.

[16] J. E. Avron, A. Elgart, G. M. Graf, and L. Sadun. *Geometry, statistics, and asymptotics of quantum pumps*. Phys. Rev. B **62**, R10618–R10621, 2000.

[17] A. V. Balatsky, I. Vekhter, and J.-X. Zhu. *Impurity-induced states in conventional and unconventional superconductors*. Rev. Mod. Phys. **78**, 373–433, 2006.

[18] S. Barkhofen, T. Nitsche, F. Elster, L. Lorz, A. Gabris, I. Jex, and C. Silberhorn. *Measuring topological invariants and protected bound states in disordered discrete time quantum walks*. arXiv:1606.00299, 2016.

[19] M. Büttiker, H. Thomas, and A. Prêtre. *Current partition in multiprobe conductors in the presence of slowly oscillating external potentials*. Z. Physik B - Condensed Matter **94**, 133–137, 1994.

[20] C. W. J. Beenakker. *Random-matrix theory of quantum transport*. Rev. Mod. Phys. **69**, 731–808, 1997.

[21] C. W. J. Beenakker. *Search for Majorana fermions in superconductors*. Annu. Rev. Condens. Matter Phys. **4**, 113–136, 2013.

[22] C. W. J. Beenakker. *Annihilation of colliding Bogoliubov quasiparticles reveals their Majorana nature*. Phys. Rev. Lett. **112**, 070604, 2014.

[23] C. W. J. Beenakker. *Random-matrix theory of Majorana fermions and topological superconductors*. Rev. Mod. Phys. **87**, 1037–1066, 2015.

[24] C. W. J. Beenakker, J. M. Edge, J. P. Dahlhaus, D. I. Pikulin, S. Mi, and M. Wimmer. *Wigner-Poisson statistics of topological transitions in a Josephson junction*. Phys. Rev. Lett. **111**, 037001, 2013.

[25] C. W. J. Beenakker and H. van Houten. *Boundary scattering and weak localization of electrons in a magnetic field*. Phys. Rev. B **38**, 3232–3240, 1988.

[26] C. W. J. Beenakker and H. van Houten. *Quantum transport in semiconductor nanostructures*. In D. Turnbull and D. Ehrenreich (editors), *Solid State Physics*, volume 44 of *Semiconductor Heterostructures and Nanostructures*, pp. 1–228. Academic Press, 1991.

[27] G. Bergmann. *Weak localization in thin films*. Phys. Rep. **107**, 1–58, 1984.

[28] N. Bhattacharya, H. B. van Linden van den Heuvell, and R. J. C. Spreeuw. *Implementation of quantum search algorithm using classical Fourier optics*. Phys. Rev. Lett. **88**, 137901, 2002.

[29] M. Blaauboer. *Charge pumping in mesoscopic systems coupled to a superconducting lead*. Phys. Rev. B **65**, 235318, 2002.

[30] E. Bocquillon, V. Freulon, J.-M. Berroir, P. Degiovanni, B. Plaçais, A. Cavanna, Y. Jin, and G. Fève. *Coherence and indistinguishability of single electrons emitted by independent sources*. Science **339**, 1054–1057, 2013.

[31] E. Bocquillon, V. Freulon, F. D. Parmentier, J.-M. Berroir, B. Plaçais, C. Wahl, J. Rech, T. Jonckheere, T. Martin, C. Grenier, D. Ferraro, P. Degiovanni, and G. Fève. *Electron quantum optics in ballistic chiral conductors*. Ann. Phys. **526**, 1–30, 2014.

[32] D. Bouwmeester, I. Marzoli, G. P. Karman, W. Schleich, and J. P. Woerdman. *Optical Galton board*. Phys. Rev. A **61**, 013410, 2000.

[33] M. A. Broome, A. Fedrizzi, B. P. Lanyon, I. Kassal, A. Aspuru-Guzik, and A. G. White. *Discrete single-photon quantum walks with tunable decoherence*. Phys. Rev. Lett. **104**, 153602, 2010.

[34] P. W. Brouwer. *Scattering approach to parametric pumping*. Phys. Rev. B **58**, R10135–R10138, 1998.

[35] F. Cardano, M. Maffei, F. Massa, B. Piccirillo, C. de Lisio, G. De Filippis, V. Cataudella, E. Santamato, and L. Marrucci. *Dynamical moments reveal a topological quantum transition in a photonic quantum walk*. arXiv:1507.01785, 2015.

[36] J. Cayssol, B. Dóra, F. Simon, and R. Moessner. *Floquet topological insulators*. Phys. Status Solidi RRL **7**, 101, 2013.

[37] S. Chakravarty and A. Schmid. *Weak localization: The quasiclassical theory of electrons in a random potential*. Phys. Rep. **140**, 193–236, 1986.

[38] W. Chang, V. E. Manucharyan, T. S. Jespersen, J. Nygård, and C. M. Marcus. *Tunneling spectroscopy of quasiparticle bound states in a spinful Josephson junction*. Phys. Rev. Lett. **110**, 217005, 2013.

[39] J. N. Chazalviel. *Spin relaxation of conduction electrons in n-type indium antimonide at low temperature*. Phys. Rev. B **11**, 1555–1562, 1975.

[40] H. O. H. Churchill, V. Fatemi, K. Grove-Rasmussen, M. T. Deng, P. Caroff, H. Q. Xu, and C. M. Marcus. *Superconductor-nanowire devices from tunneling to the multichannel regime: Zero-bias oscillations and magnetoconductance crossover*. Phys. Rev. B **87**, 241401, 2013.

[41] J. Clarke and F. K. Wilhelm. *Superconducting quantum bits*. Nature **453**, 1031–1042, 2008.

[42] F. Crépin and B. Trauzettel. *Parity measurement in topological Josephson junctions*. Phys. Rev. Lett. **112**, 077002, 2014.

[43] J. P. Dahlhaus, M. Gibertini, and C. W. J. Beenakker. *Scattering theory of topological invariants in nodal superconductors*. Phys. Rev. B **86**, 174520, 2012.

[44] A. Das, Y. Ronen, Y. Most, Y. Oreg, M. Heiblum, and H. Shtrikman. *Zero-bias peaks and splitting in an Al-InAs nanowire topological superconductor as a signature of Majorana fermions*. Nat. Phys. **8**, 887–895, 2012.

[45] S. Das Sarma, M. Freedman, and C. Nayak. *Majorana zero modes and topological quantum computation*. npj Quantum Information **1**, 15001, 2015.

[46] M. T. Deng, C. L. Yu, G. Y. Huang, M. Larsson, P. Caroff, and H. Q. Xu. *Anomalous zero-bias conductance peak in a Nb–InSb nanowire–Nb hybrid device*. Nano Lett. **12**, 6414–6419, 2012.

[47] S. Dhara, H. S. Solanki, V. Singh, A. Narayanan, P. Chaudhari, M. Gokhale, A. Bhattacharya, and M. M. Deshmukh. *Magnetotransport properties of individual InAs nanowires*. Phys. Rev. B **79**, 121311, 2009.

[48] G. Di Molfetta, F. Debbasch, and M. Brachet. *Nonlinear optical Galton board: Thermalization and continuous limit*. Phys. Rev. E **92**, 042923, 2015.

[49] M. Diez. *On electronic signatures of topological superconductivity*. Casimir PhD Series, 2015. ISBN 978-90-8593-225-3.

[50] B. Do, M. L. Stohler, S. Balasubramanian, D. S. Elliott, C. Eash, E. Fischbach, M. A. Fischbach, A. Mills, and B. Zwickl. *Experimental realization of a quantum quincunx by use of linear optical elements*. J. Opt. Soc. Am. B **22**, 499, 2005.

[51] B. Dóra, J. Cayssol, F. Simon, and R. Moessner. *Optically engineering the topological properties of a spin Hall insulator*. Phys. Rev. Lett. **108**, 056602, 2012.

[52] J. Dubois, T. Jullien, F. Portier, P. Roche, A. Cavanna, Y. Jin, W. Wegscheider, P. Roulleau, and D. C. Glattli. *Minimal-excitation states for electron quantum optics using levitons*. Nature **502**, 659–663, 2013.

[53] M. I. Dyakonov and V. I. Perel. *Spin relaxation of conduction electrons in noncentrosymmetric semiconductors*. Sov. Phys. Solid State **13**, 3023–3026, 1972.

[54] J. M. Edge and J. K. Asboth. *Localization, delocalization, and topological transitions in disordered two-dimensional quantum walks*. Physical Review B **91**, 104202, 2015.

[55] R. J. Elliott. *Theory of the effect of spin-orbit coupling on magnetic resonance in some semiconductors*. Phys. Rev. **96**, 266–279, 1954.

[56] G. Engels, J. Lange, T. Schäpers, and H. Lüth. *Experimental and theoretical approach to spin splitting in modulation-doped* $In_xGa_{1-x}As/InP$ *quantum wells for B→0*. Phys. Rev. B **55**, R1958–R1961, 1997.

[57] S. Estévez Hernández, M. Akabori, K. Sladek, C. Volk, S. Alagha, H. Hardtdegen, M. G. Pala, N. Demarina, D. Grützmacher, and T. Schäpers. *Spin-orbit coupling and phase coherence in InAs nanowires*. Phys. Rev. B **82**, 235303, 2010.

[58] J. Fabian, A. Matos-Abiague, C. Ertler, P. Stano, and I. Žutić. *Semiconductor spintronics*. Acta Phys. Slov. **57**, 2007.

[59] E. Farhi and S. Gutmann. *Quantum computation and decision trees*. Phys. Rev. A **58**, 915–928, 1998.

[60] E. Feldman and M. Hillery. *Quantum walks on graphs and quantum scattering theory*. Contemp. Math. **381**, 71, 2005.

[61] E. Feldman and M. Hillery. *Modifying quantum walks: A scattering theory approach*. arXiv:0705.4612, 2007.

[62] D. Ferraro, J. Rech, T. Jonckheere, and T. Martin. *Nonlocal interference and Hong-Ou-Mandel collisions of single Bogoliubov quasiparticles*. Phys. Rev. B **91**, 075406, 2015.

[63] H. Feshbach. *Unified theory of nuclear reactions*. Ann. Phys. **5**, 357–390, 1958.

[64] G. Feve, A. Mahe, J.-M. Berroir, T. Kontos, B. Placais, D. C. Glattli, A. Cavanna, B. Etienne, and Y. Jin. *An on-demand coherent single-electron source*. Science **316**, 1169–1172, 2007.

[65] I. C. Fulga, F. Hassler, and A. R. Akhmerov. *Scattering theory of topological insulators and superconductors*. Phys. Rev. B **85**, 165409, 2012.

[66] I. C. Fulga, F. Hassler, A. R. Akhmerov, and C. W. J. Beenakker. *Scattering formula for the topological quantum number of a disordered multimode wire*. Phys. Rev. B **83**, 155429, 2011.

[67] Y. Fyodorov and H.-J. Sommers. *Spectra of random contractions and scattering theory for discrete-time systems*. JETP Lett. **72**, 422–426, 2000.

[68] M. Genske, W. Alt, A. Steffen, A. H. Werner, R. F. Werner, D. Meschede, and A. Alberti. *Electric quantum walks with individual atoms*. Phys. Rev. Lett. **110**, 190601, 2013.

[69] J. Ghosh. *Simulating Anderson localization via a quantum walk on a one-dimensional lattice of superconducting qubits*. Phys. Rev. A **89**, 022309, 2014.

[70] A. Gómez-León and G. Platero. *Floquet-Bloch theory and topology in periodically driven lattices*. Phys. Rev. Lett. **110**, 200403, 2013.

[71] C. W. Groth, M. Wimmer, A. R. Akhmerov, and X. Waintal. *Kwant: A software package for quantum transport*. New J. Phys. **16**, 063065, 2014.

[72] L. K. Grover. *Quantum mechanics helps in searching for a needle in a haystack*. Phys. Rev. Lett. **79**, 325–328, 1997.

[73] A. E. Hansen, M. T. Björk, C. Fasth, C. Thelander, and L. Samuelson. *Spin relaxation in InAs nanowires studied by tunable weak antilocalization*. Phys. Rev. B **71**, 205328, 2005.

[74] X.-J. Hao, T. Tu, G. Cao, C. Zhou, H.-O. Li, G.-C. Guo, W. Y. Fung, Z. Ji, G.-P. Guo, and W. Lu. *Strong and tunable spin-orbit coupling of one-dimensional holes in Ge/Si core/shell nanowires*. Nano Lett. **10**, 2956–2960, 2010.

[75] M. Z. Hasan and C. L. Kane. *Colloquium: Topological insulators*. Rev. Mod. Phys. **82**, 3045–3067, 2010.

[76] P. Hauke, O. Tieleman, A. Celi, C. Ölschläger, J. Simonet, J. Struck, M. Weinberg, P. Windpassinger, K. Sengstock, M. Lewenstein, and A. Eckardt. *Non-Abelian gauge fields and topological insulators in shaken optical lattices*. Phys. Rev. Lett. **109**, 145301, 2012.

[77] A. Higginbotham, F. Kuemmeth, T. Larsen, M. Fitzpatrick, J. Yao, H. Yan, C. Lieber, and C. Marcus. *Antilocalization of Coulomb blockade in a Ge/Si nanowire*. Phys. Rev. Lett. **112**, 216806, 2014.

[78] S. Hikami, A. I. Larkin, and Y. Nagaoka. *Spin-orbit interaction and magnetoresistance in the two dimensional random system*. Prog. Theor. Phys. **63**, 707–710, 1980.

[79] M. Houzet, J. S. Meyer, D. M. Badiane, and L. I. Glazman. *Dynamics of Majorana states in a topological Josephson junction*. Phys. Rev. Lett. **111**, 046401, 2013.

[80] T. Hyart, B. van Heck, I. C. Fulga, M. Burrello, A. R. Akhmerov, and C. W. J. Beenakker. *Flux-controlled quantum computation with Majorana fermions*. Phys. Rev. B **88**, 035121, 2013.

[81] S. V. Iordanskii, Y. B. Lyanda-Geller, and G. E. Pikus. *Weak localization in quantum wells with spin-orbit interaction*. JETP Lett. **60**, 206, 1994.

[82] H. Jeong, M. Paternostro, and M. S. Kim. *Simulation of quantum random walks using the interference of a classical field*. Phys. Rev. A **69**, 012310, 2004.

[83] Y.-C. Jeong, C. D. Franco, H.-T. Lim, M. Kim, and Y.-H. Kim. *Experimental realization of a delayed-choice quantum walk*. Nat. Commun. **4**, 2471, 2013.

[84] L. Jiang, T. Kitagawa, J. Alicea, A. R. Akhmerov, D. Pekker, G. Refael, J. I. Cirac, E. Demler, M. D. Lukin, and P. Zoller. *Majorana fermions in equilibrium and in driven cold-atom quantum wires*. Phys. Rev. Lett. **106**, 220402, 2011.

[85] A. Joye and M. Merkli. *Dynamical localization of quantum walks in random environments*. J. Stat. Phys. **140**, 1025–1053, 2010.

[86] R. L. Kallaher, J. J. Heremans, N. Goel, S. J. Chung, and M. B. Santos. *Spin and phase coherence lengths in n-InSb quasi-one-dimensional wires*. Phys. Rev. B **81**, 035335, 2010.

[87] R. L. Kallaher, J. J. Heremans, N. Goel, S. J. Chung, and M. B. Santos. *Spin-orbit interaction determined by antilocalization in an InSb quantum well*. Phys. Rev. B **81**, 075303, 2010.

[88] M. Karski, L. Förster, J.-M. Choi, A. Steffen, W. Alt, D. Meschede, and A. Widera. *Quantum walk in position space with single optically trapped atoms*. Science **325**, 174–177, 2009.

[89] J. Keeling, I. Klich, and L. S. Levitov. *Minimal excitation states of electrons in one-dimensional wires*. Phys. Rev. Lett. **97**, 116403, 2006.

[90] J. Keeling, A. V. Shytov, and L. S. Levitov. *Coherent particle transfer in an on-demand single-electron source*. Phys. Rev. Lett. **101**, 196404, 2008.

[91] J. Kempe. *Quantum random walks: An introductory overview*. Contemp. Phys. **44**, 307–327, 2003.

[92] A. Keselman, L. Fu, A. Stern, and E. Berg. *Inducing time-reversal-invariant topological superconductivity and fermion parity pumping in quantum wires*. Phys. Rev. Lett. **111**, 116402, 2013.

[93] S. Kettemann. *Dimensional control of antilocalization and spin relaxation in quantum wires*. Phys. Rev. Lett. **98**, 176808, 2007.

[94] A. A. Kiselev and K. W. Kim. *Progressive suppression of spin relaxation in two-dimensional channels of finite width*. Phys. Rev. B **61**, 13115–13120, 2000.

[95] A. Kitaev. *Anyons in an exactly solved model and beyond*. Ann. Phys. **321**, 2–111, 2006.

[96] A. Y. Kitaev. *Unpaired Majorana fermions in quantum wires*. Phys. Usp. **44**, 131–136, 2001.

[97] T. Kitagawa. *Topological phenomena in quantum walks; elementary introduction to the physics of topological phases*. Quantum Inf. Process. **11**, 1107–1148, 2012.

[98] T. Kitagawa, E. Berg, M. Rudner, and E. Demler. *Topological characterization of periodically driven quantum systems*. Phys. Rev. B **82**, 235114, 2010.

[99] T. Kitagawa, M. A. Broome, A. Fedrizzi, M. S. Rudner, E. Berg, I. Kassal, A. Aspuru-Guzik, E. Demler, and A. G. White. *Observation of topologically protected bound states in a one dimensional photonic system*. Nat. Commun. **3**, 882, 2012.

[100] T. Kitagawa, T. Oka, A. Brataas, L. Fu, and E. Demler. *Transport properties of nonequilibrium systems under the application of light: Photoinduced quantum Hall insulators without Landau levels*. Phys. Rev. B **84**, 235108, 2011.

[101] T. Kitagawa, M. S. Rudner, E. Berg, and E. Demler. *Exploring topological phases with quantum walks*. Phys. Rev. A **82**, 033429, 2010.

[102] P. L. Knight, E. Roldán, and J. E. Sipe. *Quantum walk on the line as an interference phenomenon*. Phys. Rev. A **68**, 020301, 2003.

[103] Y. E. Kraus, Y. Lahini, Z. Ringel, M. Verbin, and O. Zilberberg. *Topological states and adiabatic pumping in quasicrystals*. Phys. Rev. Lett. **109**, 106402, 2012.

[104] Y. E. Kraus and O. Zilberberg. *Topological equivalence between the Fibonacci quasicrystal and the Harper model*. Phys. Rev. Lett. **109**, 116404, 2012.

[105] A. Kundu and B. Seradjeh. *Transport signatures of Floquet Majorana fermions in driven topological superconductors*. Phys. Rev. Lett. **111**, 136402, 2013.

[106] Ç. Kurdak, A. M. Chang, A. Chin, and T. Y. Chang. *Quantum interference effects and spin-orbit interaction in quasi-one-dimensional wires and rings*. Phys. Rev. B **46**, 6846–6856, 1992.

[107] Y. Lahini, M. Verbin, S. D. Huber, Y. Bromberg, R. Pugatch, and Y. Silberberg. *Quantum walk of two interacting bosons*. Phys. Rev. A **86**, 011603, 2012.

[108] L. D. Landau and E. M. Lifshitz. *Quantum Mechanics: Non-relativistic Theory*. Butterworth-Heinemann, 1977. ISBN 978-0-7506-3539-4.

[109] N. N. Lebedev and R. A. Silverman. *Special Functions and Their Applications*. Courier Corporation, 1972. ISBN 978-0-486-60624-8.

[110] C.-W. Lee, P. Kurzyński, and H. Nha. *Quantum walk as a simulator of nonlinear dynamics: Nonlinear Dirac equation and solitons*. Phys. Rev. A **92**, 052336, 2015.

[111] E. J. H. Lee, X. Jiang, R. Aguado, G. Katsaros, C. M. Lieber, and S. De Franceschi. *Zero-bias anomaly in a nanowire quantum dot coupled to superconductors*. Phys. Rev. Lett. **109**, 186802, 2012.

[112] E. J. H. Lee, X. Jiang, M. Houzet, R. Aguado, C. M. Lieber, and S. De Franceschi. *Spin-resolved Andreev levels and parity crossings in hybrid superconductor-semiconductor nanostructures*. Nat. Nanotechnol. **9**, 79–84, 2014.

[113] M. Leijnse and K. Flensberg. *Introduction to topological superconductivity and Majorana fermions*. Semicond. Sci. Technol. **27**, 124003, 2012.

[114] D. Liang and X. P. Gao. *Strong tuning of Rashba spin–orbit interaction in single InAs nanowires*. Nano Lett. **12**, 3263–3267, 2012.

[115] J. J. Lin and J. P. Bird. *Recent experimental studies of electron dephasing in metal and semiconductor mesoscopic structures*. J. Phys. Condens. Matter **14**, R501, 2002.

[116] N. H. Lindner, G. Refael, and V. Galitski. *Floquet topological insulator in semiconductor quantum wells*. Nat. Phys. **7**, 490–495, 2011.

[117] D. E. Liu, A. Levchenko, and H. U. Baranger. *Floquet Majorana fermions for topological qubits in superconducting devices and cold-atom systems*. Phys. Rev. Lett. **111**, 047002, 2013.

[118] M. S. Livshits. *The application of non-self-adjoint operators to scattering theory*. Sov. Phys. JETP **4**, 91–98, 1957.

[119] N. B. Lovett, S. Cooper, M. Everitt, M. Trevers, and V. Kendon. *Universal quantum computation using the discrete-time quantum walk*. Phys. Rev. A **81**, 042330, 2010.

[120] R. M. Lutchyn, J. D. Sau, and S. Das Sarma. *Majorana fermions and a topological phase transition in semiconductor-superconductor heterostructures*. Phys. Rev. Lett. **105**, 077001, 2010.

[121] A. Mahé, F. D. Parmentier, E. Bocquillon, J.-M. Berroir, D. C. Glattli, T. Kontos, B. Plaçais, G. Fève, A. Cavanna, and Y. Jin. *Current correlations of an on-demand single-electron emitter*. Phys. Rev. B **82**, 201309, 2010.

[122] C. Mahaux and H. A. Weidenmüller. *Shell-model approach to nuclear reactions*. North-Holland, 1969.

[123] K. Manouchehri and J. Wang. *Physical Implementation of Quantum Walks*. Springer Berlin Heidelberg, 2014. ISBN 978-3-642-36013-8.

[124] D. A. Meyer. *From quantum cellular automata to quantum lattice gases*. J. Stat. Phys. **85**, 551–574, 1996.

[125] D. A. Meyer. *Quantum mechanics of lattice gas automata: One-particle plane waves and potentials*. Phys. Rev. E **55**, 5261–5269, 1997.

[126] D. A. Meyer and T. G. Wong. *Quantum search with general nonlinearities*. Phys. Rev. A **89**, 012312, 2014.

[127] I. Mondragon-Shem, J. Song, T. L. Hughes, and E. Prodan. *Topological criticality in the chiral-symmetric AIII class as strong disorder*. Phys. Rev. Lett. **113**, 2014.

[128] V. Mourik, K. Zuo, S. M. Frolov, S. R. Plissard, E. P. A. M. Bakkers, and L. P. Kouwenhoven. *Signatures of Majorana fermions in hybrid superconductor-semiconductor nanowire devices*. Science **336**, 1003–1007, 2012.

[129] S. Nadj-Perge, V. S. Pribiag, J. W. G. van den Berg, K. Zuo, S. R. Plissard, E. P. A. M. Bakkers, S. M. Frolov, and L. P. Kouwenhoven.

*Spectroscopy of spin-orbit quantum bits in indium antimonide nanowires*. Phys. Rev. Lett. **108**, 166801, 2012.

[130] C. Navarrete-Benlloch, A. Pérez, and E. Roldán. *Nonlinear optical Galton board*. Phys. Rev. A **75**, 062333, 2007.

[131] C. Nayak, S. H. Simon, A. Stern, M. Freedman, and S. Das Sarma. *Non-Abelian anyons and topological quantum computation*. Rev. Mod. Phys. **80**, 1083–1159, 2008.

[132] H. A. Nilsson, P. Caroff, C. Thelander, M. Larsson, J. B. Wagner, L.-E. Wernersson, L. Samuelson, and H. Q. Xu. *Giant, level-dependent g-factors in InSb nanowire quantum dots*. Nano Lett. **9**, 3151–3156, 2009.

[133] J. Nitta, T. Akazaki, H. Takayanagi, and T. Enoki. *Gate control of spin-orbit interaction in an inverted* $In_{0.53}Ga_{0.47}As/In_{0.52}Al_{0.48}As$ *heterostructure*. Phys. Rev. Lett. **78**, 1335–1338, 1997.

[134] H. Obuse and N. Kawakami. *Topological phases and delocalization of quantum walks in random environments*. Phys. Rev. B **84**, 195139, 2011.

[135] Y. Oreg, G. Refael, and F. von Oppen. *Helical liquids and Majorana bound states in quantum wires*. Phys. Rev. Lett. **105**, 177002, 2010.

[136] F. D. Parmentier, E. Bocquillon, J.-M. Berroir, D. C. Glattli, B. Plaçais, G. Fève, M. Albert, C. Flindt, and M. Büttiker. *Current noise spectrum of a single-particle emitter: Theory and experiment*. Phys. Rev. B **85**, 165438, 2012.

[137] A. Peruzzo, M. Lobino, J. C. F. Matthews, N. Matsuda, A. Politi, K. Poulios, X.-Q. Zhou, Y. Lahini, N. Ismail, K. Wörhoff, Y. Bromberg, Y. Silberberg, M. G. Thompson, and J. L. OBrien. *Quantum walks of correlated photons*. Science **329**, 1500–1503, 2010.

[138] D. I. Pikulin and Y. V. Nazarov. *Topological properties of superconducting junctions*. JETP Lett. **94**, 693–697, 2012.

[139] S. R. Plissard, D. R. Slapak, M. A. Verheijen, M. Hocevar, G. W. G. Immink, I. van Weperen, S. Nadj-Perge, S. M. Frolov, L. P. Kouwenhoven, and E. P. A. M. Bakkers. *From InSb nanowires to nanocubes: Looking for the sweet spot*. Nano Lett. **12**, 1794–1798, 2012.

[140] S. R. Plissard, I. van Weperen, D. Car, M. A. Verheijen, G. W. G. Immink, J. Kammhuber, L. J. Cornelissen, D. B. Szombati, A. Geresdi, S. M. Frolov, L. P. Kouwenhoven, and E. P. A. M. Bakkers. *Formation and electronic properties of InSb nanocrosses*. Nat. Nanotechnol. **8**, 859–864, 2013.

[141] C. Poli, M. Bellec, U. Kuhl, F. Mortessagne, and H. Schomerus. *Selective enhancement of topologically induced interface states in a dielectric resonator chain*. Nat. Commun. **6**, 6710, 2015.

[142] E. Prodan and H. Schulz-Baldes. *Bulk and Boundary Invariants for Complex Topological Insulators*. Mathematical Physics Studies. Springer International Publishing, Cham, 2016. ISBN 978-3-319-29351-6.

[143] X.-L. Qi and S.-C. Zhang. *Topological insulators and superconductors*. Rev. Mod. Phys. **83**, 1057–1110, 2011.

[144] E. I. Rashba. *Properties of semiconductors with an extremum loop. 1. Cyclotron and combinational resonance in a magnetic field perpendicular to the plane of the loop.* Sov. Phys. Solid State **2**, 1109–1122, 1960.

[145] M. C. Rechtsman, J. M. Zeuner, Y. Plotnik, Y. Lumer, D. Podolsky, F. Dreisow, S. Nolte, M. Segev, and A. Szameit. *Photonic Floquet topological insulators*. Nature **496**, 196–200, 2013.

[146] M. D. Reichl and E. J. Mueller. *Floquet edge states with ultracold atoms*. Phys. Rev. A **89**, 063628, 2014.

[147] P. Roulleau, T. Choi, S. Riedi, T. Heinzel, I. Shorubalko, T. Ihn, and K. Ensslin. *Suppression of weak antilocalization in InAs nanowires*. Phys. Rev. B **81**, 155449, 2010.

[148] M. S. Rudner and L. S. Levitov. *Topological transition in a non-hermitian quantum walk*. Phys. Rev. Lett. **102**, 065703, 2009.

[149] M. S. Rudner, N. H. Lindner, E. Berg, and M. Levin. *Anomalous edge states and the bulk-edge correspondence for periodically driven two-dimensional systems*. Phys. Rev. X **3**, 031005, 2013.

[150] S. Ryu, A. P. Schnyder, A. Furusaki, and A. W. W. Ludwig. *Topological insulators and superconductors: Tenfold way and dimensional hierarchy*. New J. Phys. **12**, 065010, 2010.

[151] P. San-Jose, J. Cayao, E. Prada, and R. Aguado. *Majorana bound states from exceptional points in non-topological superconductors*. Sci. Rep. **6**, 21427, 2016.

[152] L. Sansoni, F. Sciarrino, G. Vallone, P. Mataloni, A. Crespi, R. Ramponi, and R. Osellame. *Two-particle bosonic-fermionic quantum walk via integrated photonics*. Phys. Rev. Lett. **108**, 010502, 2012.

[153] J. D. Sau and E. Demler. *Bound states at impurities as a probe of topological superconductivity in nanowires*. Phys. Rev. B **88**, 205402, 2013.

[154] J. D. Sau, S. Tewari, and S. Das Sarma. *Experimental and materials considerations for the topological superconducting state in electron- and hole-doped semiconductors: Searching for non-Abelian Majorana modes in 1D nanowires and 2D heterostructures*. Phys. Rev. B **85**, 064512, 2012.

[155] T. Schäpers, V. A. Guzenko, M. G. Pala, U. Zülicke, M. Governale, J. Knobbe, and H. Hardtdegen. *Suppression of weak antilocalization in $Ga_xIn_{1-x}As/InP_xIn_{1-x}As$ narrow quantum wires*. Phys. Rev. B **74**, 081301, 2006.

[156] M. J. Schmidt, D. Rainis, and D. Loss. *Decoherence of Majorana qubits by noisy gates*. Phys. Rev. B **86**, 085414, 2012.

[157] H. Schmitz, R. Matjeschk, C. Schneider, J. Glueckert, M. Enderlein, T. Huber, and T. Schaetz. *Quantum walk of a trapped ion in phase space*. Phys. Rev. Lett. **103**, 090504, 2009.

[158] A. Schreiber, K. N. Cassemiro, V. Potoček, A. Gábris, I. Jex, and C. Silberhorn. *Decoherence and disorder in quantum walks: From ballistic spread to localization*. Phys. Rev. Lett. **106**, 180403, 2011.

[159] A. Schreiber, K. N. Cassemiro, V. Potoček, A. Gábris, I. Jex, and C. Silberhorn. *Decoherence and disorder in quantum walks: From ballistic spread to localization*. Phys. Rev. Lett. **106**, 180403, 2011.

[160] A. Schreiber, K. N. Cassemiro, V. Potoček, A. Gábris, P. J. Mosley, E. Andersson, I. Jex, and C. Silberhorn. *Photons walking the line: A quantum walk with adjustable coin operations*. Phys. Rev. Lett. **104**, 050502, 2010.

[161] A. Schreiber, A. Gábris, P. P. Rohde, K. Laiho, M. Štefaňák, V. Potoček, C. Hamilton, I. Jex, and C. Silberhorn. *A 2D quantum walk simulation of two-particle dynamics*. Science **336**, 55–58, 2012.

[162] N. Shenvi, J. Kempe, and K. B. Whaley. *Quantum random-walk search algorithm*. Phys. Rev. A **67**, 052307, 2003.

[163] Y. Shikano, T. Wada, and J. Horikawa. *Discrete-time quantum walk with feed-forward quantum coin*. Sci. Rep. **4**, 2014.

[164] A. S. Solntsev, A. A. Sukhorukov, D. N. Neshev, and Y. S. Kivshar. *Spontaneous parametric down-conversion and quantum walks in arrays of quadratic nonlinear waveguides*. Phys. Rev. Lett. **108**, 023601, 2012.

[165] T. D. Stanescu and S. Tewari. *Majorana fermions in semiconductor nanowires: Fundamentals, modeling, and experiment*. J. Phys. Condens. Matter **25**, 233201, 2013.

[166] W. P. Su, J. R. Schrieffer, and A. J. Heeger. *Solitons in polyacetylene*. Phys. Rev. Lett. **42**, 1698–1701, 1979.

[167] K. Sun, W. V. Liu, A. Hemmerich, and S. Das Sarma. *Topological semimetal in a fermionic optical lattice*. Nat. Phys. **8**, 67–70, 2012.

[168] M. Szegedy. *Quantum speed-up of Markov chain based algorithms*. In *Proceedings of the 45th Annual IEEE Symposium on Foundations of Computer Science*, pp. 32–41. 2004.

[169] B. Tarasinski, J. K. Asbóth, and J. P. Dahlhaus. *Scattering theory of topological phases in discrete-time quantum walks*. Phys. Rev. A **89**, 042327, 2014.

[170] M. Thakurathi, A. A. Patel, D. Sen, and A. Dutta. *Floquet generation of Majorana end modes and topological invariants*. Phys. Rev. B **88**, 155133, 2013.

[171] M. Tinkham. *Introduction to Superconductivity*. Dover Publications, 2004. ISBN 978-0-486-43503-9.

[172] Q.-J. Tong, J.-H. An, J. Gong, H.-G. Luo, and C. H. Oh. *Generating many Majorana modes via periodic driving: A superconductor model*. Phys. Rev. B **87**, 201109, 2013.

[173] B. van Heck, S. Mi, and A. R. Akhmerov. *Single fermion manipulation via superconducting phase differences in multiterminal Josephson junctions*. Phys. Rev. B **90**, 155450, 2014.

[174] M. G. Vavilov, V. Ambegaokar, and I. L. Aleiner. *Charge pumping and photovoltaic effect in open quantum dots*. Phys. Rev. B **63**, 195313, 2001.

[175] S. E. Venegas-Andraca. *Quantum walks: A comprehensive review*. Quantum Inf. Process. **11**, 1015–1106, 2012.

[176] Y. H. Wang, H. Steinberg, P. Jarillo-Herrero, and N. Gedik. *Observation of Floquet-Bloch states on the surface of a topological insulator*. Science **342**, 453–457, 2013.

[177] F. Wilczek. *Majorana returns*. Nat. Phys. **5**, 614–618, 2009.

[178] M. Wimmer, A. R. Akhmerov, J. P. Dahlhaus, and C. W. J. Beenakker. *Quantum point contact as a probe of a topological superconductor*. New J. Phys. **13**, 053016, 2011.

[179] R. Winkler. *Spin-orbit Coupling Effects in Two-Dimensional Electron and Hole Systems*. Springer Science & Business Media, 2003. ISBN 978-3-540-01187-3.

[180] M. W. Wu, J. H. Jiang, and M. Q. Weng. *Spin dynamics in semiconductors*. Phys. Rep. **493**, 61–236, 2010.

[181] T. Xu, K. A. Dick, S. Plissard, T. H. Nguyen, Y. Makoudi, Maxime Berthe, J.-P. Nys, X. Wallart, B. Grandidier, and P. Caroff. *Faceting, composition and crystal phase evolution in III–V antimonide nanowire heterostructures revealed by combining microscopy techniques*. Nanotechnology **23**, 095702, 2012.

[182] Y. Yafet. *g-factors and spin-lattice relaxation of conduction electrons*. In F. Turnbull and D. Seitz (editors), *Solid State Physics*, volume 14, pp. 1–98. Academic Press, 1963.

[183] T. Yokoyama, M. Eto, and Y. V. Nazarov. *Josephson current through semiconductor nanowire with spin–orbit interaction in magnetic field*. J. Phys. Soc. Jpn. **82**, 054703, 2013.

[184] F. Zähringer, G. Kirchmair, R. Gerritsma, E. Solano, R. Blatt, and C. F. Roos. *Realization of a quantum walk with one and two trapped ions*. Phys. Rev. Lett. **104**, 100503, 2010.

[185] O. Zaitsev, D. Frustaglia, and K. Richter. *Semiclassical theory of weak antilocalization and spin relaxation in ballistic quantum dots*. Phys. Rev. B **72**, 155325, 2005.

[186] J. M. Zeuner, M. C. Rechtsman, Y. Plotnik, Y. Lumer, S. Nolte, M. S. Rudner, M. Segev, and A. Szameit. *Observation of a topological transition in the bulk of a non-hermitian system*. Phys. Rev. Lett. **115**, 040402, 2015.

# Samenvatting

Topologische eigenschappen van kwantummechanische golffuncties staan momenteel sterk in de belangstelling, vooral in verband met elektronen in de vaste stof. Een recente ontwikkeling in dit vakgebied is de aandacht voor systemen die periodiek in de tijd worden aangedreven, bijvoorbeeld door een elektromagnetisch wisselveld. Doorgaans behandelt men dit externe veld niet kwantummechanisch, het is slechts een middel om de eigenschappen van de elektronen in sterke mate te variëren, en zo de topologie van de elektrongolffunctie te beïnvloeden.

Het eenvoudigste en meest gangbare model dat periodieke aandrijving kan beschrijven is de zogenaamde kwantumwandeling, het kwantummechanische analogon van de toevals-wandeling ("random walk") in de klassieke mechanica. De aanwezigheid van een rijke verscheidenheid aan topologische kenmerken in een kwantumwandeling is al een tijd geleden opgemerkt, in de context van de “gebruikelijke” formulering van topologische invarianten door middel van eigenfuncties van de Hamiltoniaan. Een alternatieve formulering in termen van de verstrooiingsmatrix (S-matrix) is veel efficiënter gebleken voor niet-aangedreven systemen, en bovendien is zo’n formulering direct toepasbaar op wanordelijke systemen. In het tweede hoofdstuk van dit proefschrift (na de inleiding in hoofdstuk één) laten we zien hoe de S-matrix-aanpak toegepast kan worden op kwantumwandelingen, met dezelfde voordelen. Niet alleen is de S-matrix-aanpak nuttig voor theoretische computersimulaties, maar zij kan ook worden toegepast op optische experimenten, omdat de S-matrix een middel biedt om de topologische invariant heel direct uit een verstrooiingsexperiment af te leiden.

Er is een model dat lijkt op de kwantumwandeling, met een duidelijke onderbouwing op grond van een Hamiltoniaan met tijdsafhankelijke parameters, het zogenaamde Su-Schrieffer-Heeger (SSH) model. We verkennen in hoofdstuk drie onder welke omstandigheden de symmetrie van het statische SSH-model behouden blijft in de dynamische, in de tijd aangedreven, versie, en we geven eenvoudige uitdrukkingen voor de topologische invarianten in termen van het windingsgetal

van de tijdsevolutie-operator. We tonen aan dat dit systeem door een opeenvolging van verschillende topologische fasen kan worden geleid, eenvoudigweg door het aandrijvingspatroon aan te passen.

De aanwezigheid van een externe aandrijving kan ook een radicale verandering teweegbrengen in de invloed van kwantumruis en niet-lineaire effecten ten gevolge van de omgeving. Deze effecten kunnen in experimenten niet uitgesloten worden, en soms worden ze zelfs met opgezet aangebracht. We onderzoeken om deze reden in hoofdstuk vier een niet-lineaire variant van een kwantumwandeling, met inbegrip van termen die wrijving (relaxatie) veroorzaken. Als we in dit systeem een topologische domeinwand aanbrengen, dan vinden we dat voor sommige vormen van niet-lineariteit de topologisch beschermde gebonden toestand behouden blijft, en bovendien een speciale rol vervult als aantrekker of afstoter ("attractor/repellor") van de niet-lineaire dynamica.

De laatste twee hoofdstukken van het proefschrift behandelen iets andere vraagstukken. In hoofdstuk vijf onderzoeken we een aangedreven systeem dat in de belangstelling staat als een bron voor enkele elektronen: een zogenaamde kwantumdoos ("quantum dot") die aangedreven wordt door een tijdsafhankelijke spanning en dan één voor één elektronen of gaten injecteert in een reservoir. Ons doel is om een supergeleidende variant van dit systeem te construeren, waarbij de kwantumdoos vervangen is door een Josephsonjunctie tussen topologische supergeleiders. De geïnjecteerde deeltjes zijn nu zogenaamde Bogoliubov-quasideeltjes (een mengeling van elektronen en gaten). We leiden een expliciete uitdrukking af voor de golffunctie van de deeltjes en vinden dat zowel de injectiesnelheid als de aard van de koppeling tussen Josephsonjunctie en reservoir van cruciaal belang zijn voor de bepaling van de lading van het geïnjecteerde deeltje.

In hoofdstuk zes beschrijven we tenslotte de experimentele uitdaging om de spinbaankoppeling-sterkte te bepalen van de InSb (indium-antimoon) nanodraden die momenteel zo sterk in de belangstelling staan als topologische supergeleiders en bron van Majoranadeeltjes. De sterkte van de spinbaankoppeling kan in principe gehaald worden uit de details van geleidingsmetingen die het zogenaamde "zwakke localizatie effect" vertonen. Het gaat dan om een weerstandspiek rond magneetveld nul, die soms overgaat in een dip (men spreekt dan van "zwakker antilocalizatie"). Om de gewenste informatie uit de metingen te halen is het nodig om het geheel van de elektronenpaden in de

nanodraad te beschouwen, die beïnvloed worden door het magneetveld en de spinbaankoppeling. De InSb nanodraden hebben een zeshoekige doorsnede, die we nauwkeurig in rekening hebben gebracht in een numerieke simulatie. We vonden grote afwijkingen van resultaten in de literatuur voor platte draden, in het bijzonder machtswetten met niet-heeltallige exponenten. Onze resultaten konden direct toegepast worden op magnetoweerstand-metingen in het QuTech laboratorium aan de TU Delft.

# Summary

Topological properties of wave functions in quantum mechanics, especially in the context of electrons in condensed matter systems, have recently attracted a lot of theoretical and experimental attention. One of the more recent developments in this field is the attention to systems which are subject to external fields that vary periodically in time, so-called driven systems. The external fields themselves are typically not treated quantum mechanically, but can be used to influence and change the properties (topological and otherwise) of the electrons in a wide range.

As a minimal model that captures the physics introduced by external driving, an often considered model is the so-called (discrete time) quantum walk, a quantum mechanical analogue of the classical random walk. In the "usual" formulation of topological properties in terms of invariants of bulk wave functions, the richness of topological phases in quantum walks has been realized a while ago. Another formulation of topological invariants in terms of the scattering matrix has proven very useful for non-driven systems due to its numerical efficiency and easy extension to disordered systems. We show in the second chapter of this thesis (after the introductory first chapter) how this approach could be extended to quantum walks and find that the same advantages apply. We show that the scattering matrix approach is not only useful in theoretical numerical studies, but can also directly be implemented in photonic experiments as a direct probe for the topological invariant of a quantum walk.

A model actually derived from a driven Hamiltonian, the Su-Schrieffer-Heeger (SSH) model with driven time-dependent parameters, is closely related to the quantum walk. In chapter three we explore under what conditions the symmetries of the (static) SSH model carry over to the driven version and give simple closed expressions for the topological invariants in terms of winding numbers of the time-evolution operator, and thus the driving. We show that this system can be tuned through a manifold of different phases by only changing the driving pattern.

The presence of external driving can also radically change the role of quantum noise and non-linear effects due to the environment on the system, which is inadvertently present or can even be engineered in experiments. We thus study in chapter four a non-linear modification of the quantum walk which involves terms that lead to quantum friction and thus relaxation. In the presence of topological domain boundaries, we find that for certain forms of the non-linearity, the topologically protected bound states obtain a very special role as either attractors or repellors of the global dynamics of the system.

The last two chapters of this thesis consider slightly different questions. A driven system that has been subject to recent research is the so-called single electron emitter, which consists of a quantum dot subject to a time-dependent gate voltage which emits individual electrons or holes to a coupled electron reservoir. In chapter five, we attempt to construct a superconducting version of this system where the quantum dot is replaced by a Josephson junction between topological superconductors and calculate the properties of the emitted so-called Bogoliubov quasiparticles (superpositions of electrons and holes) in the aperiodic limit of driving. We derive an analytical expression for the wave function of the emitted particles and find that both the driving speed and the nature of the coupling between junction and reservoir are crucial in determining the charge of the emitted particle.

In the sixth and final chapter, we consider the experimental challenge of extracting spin-orbit coupling strength in InSb nanowires, which are the basis for constructing (non-driven) one-dimensional topological superconductors. Spin-orbit coupling strength can be obtained by magnetoconductance measurements, which contain weak localization and weak anti-localization features. In order to extract the desired information from these features, one needs to consider the ensemble of closed paths in the given geometry and the average effect of magnetic and spin-orbit fields on these paths. For hexagonal nanowires such as the InSb nanowires under consideration, we numerically determine those influences and found striking differences, such as non-integer power laws, in comparison to previous models *e.g.* for two-dimensional nanowires. We immediately apply these results to magnetoconductance measurements performed in the QuTech laboratory at the TU Delft.

# Zusammenfassung

Topologischen Eigenschaften von quantenmechanischen Wellenfunktionen, insbesondere im Kontext der Festkörperphysik, wurden in der letzten Zeit viel Aufmerksamkeit zuteil, sowohl theoretisch als auch experimentell. Eine der letzten Entwicklungen ist die Untersuchung von Systemen die von äußeren Feldern beeinflusst werden, welche periodisch von der Zeit abhängen, sogenannte getriebene Systeme. Die äußeren Felder werden für gewöhnlich nicht quantenmechanisch behandelt, aber sie können verwendet werden, um die Eigenschaften (topologische und andere) der Elektronen in großem Maße zu beeinflussen.

Ein minimales Modell, welches die Eigenschaften abbildet, die periodische äußere Felder mit sich bringen, ist der sogenannte (zeitdiskrete) Quantum Walk, ein quantenmechanisches Analogon zum klassischen Random Walk. In der üblichen Formulierung von topologischen Eigenschaften durch Invarianten von ausgedehnten Wellenfunktionen wurde die Reichhaltigkeit topologischer Phasen von Quantum Walks vor einiger Zeit erkannt. Eine andere Formulierung, die auf Streumatrizen basiert, hat sich bereits für nicht getriebene Systeme wegen seiner numerischen Effizienz und einfachen Übertragbarkeit auf ungeordnete Systeme als nützlich erwiesen. Im zweiten Kapitel dieser Arbeit (nach der Einleitung im ersten Kapitel) zeigen wir, wie dieser Ansatz auf Quantum Walks übertragen werden kann und dass die selben Vorteile zutreffen. Wir zeigen, dass der Streumatrixansatz nicht nur in theoretischen numerischen Studien von Nutzen ist, sondern dass er auch direkt in Experimenten mit Photonen zur Messung der topologischen Invarianten von Quantum Walks verwendet werden kann.

Ein mit Quantum Walks nahe verwandtes Modell, welches direkt durch ein getriebenen Hamiltonian gegeben ist, ist das Su-Schrieffer-Heeger-Modell (SSH-Modell) mit getriebenen zeitabhängigen Parametern. Wir untersuchen in Kapitel drei unter welchen Umständen die Symmetrieeigenschaften des ungetrieben SSH-Modells auf das getriebene Modell übertragen werden können, und geben einfache geschlossene Formeln für die topologischen Invarianten, ausgedrückt durch den Zeit-

entwicklungsoperator, und damit durch die treibenden Felder, an. Wir zeigen, dass dieses System nur durch Verändern der treibenden Felder eine Mannigfaltigkeit von topologischen Phasen erreichen kann.

Äußere Felder verändern auch grundlegend die Rolle von Quantenrauschen und nichtlinearen Effekten durch die Umgebung auf das System, welche in Experimenten immer vorhanden sind oder sogar gezielt manipuliert werden können. Wir untersuchen daher in Kapitel vier eine nichtlineare Variante des Quantum Walks, welches Terme enthält, die zu Quantenreibung und damit Relaxation führen. Bei Vorhandensein von topologischen Phasengrenzen im System finden wir, dass für manche Formen der Nichtlinearität die lokal gebundenen topologischen Zustände eine besondere Rolle als Attraktoren für die globale Zeitentwicklung des Systems einnehmen.

Die letzten beiden Kapitel sind etwas anders gearteten Fragen gewidmet. Ein getriebenes System, das in letzter Zeit häufig untersucht wurde, ist der Einzelelektronen-Emitter (engl. single electron emitter), der aus einem Quantenpunkt mit zeitabhänger Gatespannung besteht, welcher einzelne Elektronen oder Löcher in ein gekoppeltes Reservoir aussendet. Im fünften Kapitel versuchen wir, eine supraleitende Variante dieses Systems zu konstruieren, in dem der Quantenpunkt durch einen Josephson-Kontakt zwischen topologischen Supraleitern ersetzt wird, und leiten die Eigenschaften des ausgesendeten Bogoliubov-Quasiteilchens (eine quantenmechanische Superposition von Teilchen und Loch) im Grenzfall aperiodischen Treibens her. Wir erhalten analytische Ausdrücke für die Wellenfunktion der ausgesendeten Teilchen and finden, dass die Ladung des Teilchens stark von sowohl der Änderungsgeschwindigkeit des treibenden Feldes als auch von der Art der Kopplung an das Reservoir abhängt.

Im sechsten und letzten Kapitel betrachten wir das experimentelle Problem, die Stärke der Spinbahnkopplung in Indiumantimonid-Nanodrähten, die die Grundlage für die Konstruktion von eindimensionalen (nicht-getriebenen) topologischen Supraleitern bilden, zu bestimmen. Die Spinbahnkopplung kann aus magnetfeldabhängigen Leitwertmessungen erhalten werden, die schwache Lokalisierungs- und Antilokalisierungssignale enthalten. Um die gewünschte Information zu erhalten, muss das Ensemble geschlossener Pfade in der gegeben Geometrie und der Einfluss des Magnetfelds und Spinbahnfelds auf diese Pfade bestimmt werden. Für hexagonale Drähte bestimmen wir diesen Einfluss durch numerische Simulation und finden auffallende Unterschiede, wie

nichtganzzahlige Skalierungsexponenten, im Vergleich zu früheren Modellen für zum Beispiel zweidimensionale Nanodrähte. Wir wenden diese Ergebnisse auf experimentelle Ergebnisse an, die im QuTech-Labor an der TU Delft erhalten wurden.

# Curriculum Vitæ

I was born in Berlin, (West-)Germany, in 1988. After moving to Frankenthal (Pfalz) in 1995, where I attended primary school, I received my secondary education at Carl-Bosch-Gymnasium in Ludwigshafen am Rhein, where I graduated in 2006. In 2006–2007, I completed a nine months civil service at a hospital in Bad Dürkheim.

I moved back to Berlin in 2007 and enrolled for a Bachelor of Science in Physics at the Freie Universität Berlin, from which I graduated in 2010; my thesis "Edge state mixing in the quantum hall effect in p–n junctions in graphene" was supervised by Piet Brouwer. Immediately afterwards, I enrolled for the Master of Science in Physics at the same university, and graduated in 2012 with my thesis “Fluctuation corrections to conductivity in superconducting films and cylinders” which was supervised by Georg Schwiete, again in the group of Piet Brouwer.

I continued my studies joining the group of Carlo Beenakker in Leiden in 2013 as a PhD student at the Instituut Lorentz, part of the Leiden Institute of Physics, and employed by the Stichting voor Fundamenteel Onderzoek der Materie (FOM). During my time there, I collaborated closely with experimental physicists from the group of Leo Kouwenhoven and Leonardo DiCarlo, both at TU Delft, and with Janos Asbóth at the Wigner Institute for Advanced Studies in Budapest, Hungary. I also supervised a project of a visiting Bachelor student, Yaroslav Gerasimenko, which resulted in a publication. I taught the exercise classes of the Statistical Physics 2 course in Leiden in 2013, 2014 and 2015, for which I was awarded a Teaching Assistant Prize from the Faculty of Science in 2014. I attended many conferences and workshops and presented my work to others in the Netherlands, Hungary, Germany, France, Finland, Ukraine, and Italy.

# List of publications

- B. Tarasinski and G. Schwiete. *Fluctuation conductivity of disordered superconductors in magnetic fields*. Phys. Rev. B **88**, 014518, 2013.

- B. Tarasinski, J. K. Asbóth, and J. P. Dahlhaus. *Scattering theory of topological phases in discrete-time quantum walks*. Phys. Rev. A **89**, 042327, 2014. [Chapter 2]

- J. K. Asbóth, B. Tarasinski, and P. Delplace. *Chiral symmetry and bulk-boundary correspondence in periodically driven one-dimensional systems*. Phys. Rev. B **90**, 125143, 2014. [Chapter 3]

- P. Baireuther, T. Hyart, B. Tarasinski, and C. W. J. Beenakker. *Andreev-Bragg reflection from an Amperian superconductor*. Phys. Rev. Lett. **115**, 097001, 2015.

- I. van Weperen, B. Tarasinski, D. Eeltink, V. S. Pribiag, S. R. Plissard, E. P. A. M. Bakkers, L. P. Kouwenhoven, and M. Wimmer. *Spin-orbit interaction in InSb nanowires*. Phys. Rev. B **91**, 201413, 2015. [Chapter 6]

- B. Tarasinski, D. Chevallier, J. A. Hutasoit, B. Baxevanis, and C. W. J. Beenakker. *Quench dynamics of fermion-parity switches in a Josephson junction*. Phys. Rev. B **92**, 144306, 2015. [Chapter 5]

- Y. Gerasimenko, B. Tarasinski, and C. W. J. Beenakker. *Attractor-repeller pair of topological zero-modes in a nonlinear quantum walk*. Phys. Rev. A **93**, 022329, 2016. [Chapter 4]

# Stellingen

behorende bij het proefschrift
*On periodically driven quantum systems*

1. Unlike their static counterparts, the bulk topological properties of one-dimensional periodically driven quantum systems are characterized by *two* (not one) independent invariants.

   Chapter 2

2. The two invariants of a chiral symmetric driven system are the winding numbers on a torus of half the Floquet operator.

   Chapter 3, thesis cover

3. In an open driven quantum system, topological boundary states can actively trap particles from the bulk.

   Chapter 4

4. The magnetic-field dependent relaxation time $\tau_B$ for weak localization in a nanowire with a hexagonal cross-section depends on the width $W$ with a non-integer exponent, $\tau_B \propto W^{-\gamma}$, $\gamma = 3.174 \pm 0.003$, hinting to hidden fractal properties of electron dynamics in that geometry.

   Chapter 6

5. The full density matrix simulation of the Surface-17 quantum error correction code, requiring thousands of CPU hours as reported by Tomita & Svore [PRA **90**, 062320 (2014)], can be reproduced in a few hours on a single GPU.

   `https://github.com/brianzi/quantumsim`

6. The computational universality of continuous-time quantum walks [Childs, PRL **102**, 180501 (2008)] is of little practical use, because one would need a universal quantum computer to produce the quantum walk in the first place.

7. The construction of "Majorana bound states in non-topological superconductors" described by San Jose et al. [Sci. Rep. **6**, 21427 (2016)] relies not only on charge-conjugation symmetry but also on chiral symmetry.

8. The runtime of a sufficiently accurate decoding algorithm based on minimal-weight matching for the surface code [Fowler et al., PRA **86**, 042313 (2012)] will be dominated not by the matching subroutine, but by the subroutine for weight calculation, especially for low-distance codes.

Brian Tarasinski
20 september 2016